Investigation of amyloid beta peptide aggregation by small angle neutron scattering and complementary methods

Inaugural-Dissertation

Zur Erlangung des Doktorgrades

der Mathematisch-Naturwissenschaftlichen Fakultät

der Heinrich-Heine-Universität Düsseldorf

Vorgelegt von

Bo Zhang-Haagen

aus Harbin, China

Düsseldorf, September 2016

Aus dem Institut für Physikalische Biologie der Heinrich-Heine-Universität Düsseldorf

Gedruckt mit der Genehmigung der Mathematisch-Naturwissenschaftlichen Fakultät der Heinrich-Heine-Universität Düsseldorf

Referent: Prof. Dr. Dieter Willbold

Korreferent: Prof. Dr. Lutz Schmitt

Tag der mündlichen Prüfung:

Eidesstattliche Erklärung

Ich versichere eidesstattlich, dass ich die vorliegende Arbeit selbstständig und ohne Benutzung anderer als der angegebenen Hilfsmittel angefertigt habe. Alle Stellen, die wörtlich oder sinngemäß aus Veröffentlichungen entnommen sind, wurden als solche kenntlich gemacht.

Die Arbeit hat in gleicher oder ähnlicher Form keiner anderen Prüfungsbehörde vorgelegen.

Bedburg-Hau, den 27.09.2016

Danksagung

Eine wissenschaftliche Arbeit ist nie das Werk einer einzelnen Person. Deshalb möchte ich diese Gelegenheit nutzen, um mich bei allen Menschen zu bedanken, die mich bei der Erstellung dieser Arbeit unterstützt haben und so zum Gelingen dieser Arbeit beigetragen haben.

Einigen Personen gilt mein ganz besonderer Dank, insbesondere:

- Meinem Doktorvater Herr Professor Dr. Dieter Willbold vom Institut für physikalische Biologie der Universität Düsseldorf danke ich dafür, dass ich unter seiner Betreuung diese Promotion anfertigen konnte sowie für die Überlassung des interessanten Themas. Auch danke ich ihm für die gute Zusammenarbeit, Unterstützung und Förderung.
- Herrn Professor Dr. Dieter Richter vom Jülich Centre for Neuron Science am Forschungszentrum Jülich für die Möglichkeit der Zusammenarbeit. Insbesondere danke ich Ihm für die produktiven und fruchtbaren Diskussionen, die diese Promotion und dessen Publikationen vorangetrieben haben.
- Meinen Betreuern Frau Dr. Luitgard Nagel-Steger und Herr Dr. Ralf Biehl für die Einführung in die Thematik, den vielen intensiven Diskussionen, den vielen konstruktiven und kritischen Anmerkungen sowie den hilfreichen und zuverlässigen Korrekturen.
- Dem Team der Außenstelle des Forschungszentrums Jülich in Garching für die freundliche Unterstützung während der zeitaufwendigen Messungen. Insbesondere danke ich dem Geräteverantwortlichen Herrn Dr. Aurel Radulescu für die kompetente und zuvorkommende technische Assistenz.
- Meinen Kollegen in Düsseldorf und Jülich für die freundschaftliche, konstruktive und kooperative Zusammenarbeit.
- Meinem Mann Markus, der mich in den richtigen Momenten zu motivieren wusste, für mich da war und an mich geglaubt hat.
- Nicht zuletzt danke ich meinen Eltern, die in jeglicher Hinsicht die Grundsteine für meinen Weg gelegt haben.

Contents

1. Introduction

1.1 Protein aggregation

Proteins are important fundamental subunits of living systems synthesised at the ribosome by formation of peptide bonds between different amino acids according to the genetic code. The amino acid is a chiral molecule with an amine ($-NH_2$), a carboxylic acid functional group ($-COOH$), a hydrogen ($-H$) and a so called side chain ($-R$) binding on the chiral center (see figure 1.1). Side chains with distinct properties, for instance, charged/uncharged, hydrophobic and hydrophilic, regulate the properties of amino acids. From the genetic code therefore the structures, the dynamics and the biological functions of proteins will be defined, which are adjusted also by post-translational modification.

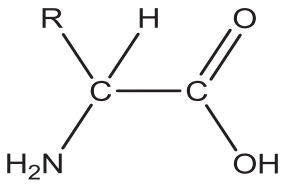

Figure 1.1: General chemical conformation of an amino acid with R as side chain.

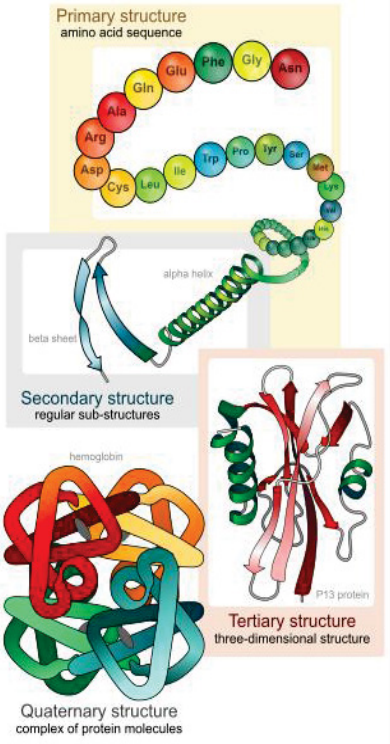

Figure 1.2: Protein structure from upper to lower: Primary, secondary, tertiary and quaternary structure[1].

The structure of proteins is classified as primary, secondary, tertiary and quaternary structure showed in figure 1.2[1]. The primary structure is the protein sequence determined from the genetic code, whereas the secondary structure describes the local structure stabilized by hydrogen bonds between the amino acids. The most common secondary structure elements are the α-helix with 3.6 amino acid residues per turn and β-sheets in two distinct conformations: antiparallel and parallel. To study the secondary structure circular dichroism spectroscopy (CD) and Fourier transform infrared spectroscopy (FTIR) are used, whereby FTIR has the advantage to distinguish parallel and antiparallel β sheet as well as the intra- and intermolecular β-sheet from each other. The tertiary structure is the 3D structure of proteins in the folded state, while the quaternary structure is the complex consisting of more than one polypeptide chain.

Normally, proteins start to fold into their native state already during the synthesis at the ribosome. According to certain requirements of body native proteins can self-assembly to form fibres, oligomers or crystals as shown in figure 1.3[2]. The native state of protein mostly represents a low-energy 3D structure, which determines protein functions (structure-function paradigm[3]). However, due to some reasons proteins can also fold to a disordered configuration (misfolding) or remain unfolded in the tissue (see figure 1.3[2]), which tend to induce diseases. Therefore mis- and unfolded proteins will be commonly degraded in the cytoplasm or refold to their correct configurations with help of chaperones. But in some cases the mis- and unfolded proteins can also fail in their biological function and are prone to aggregate. Some protein aggregations like G-actin are needful for the human body[4], whereas others lead to diseases due to the toxic intermediates produced during the aggregation process[5,6] and accumulation of insoluble fibrils in the tissue.

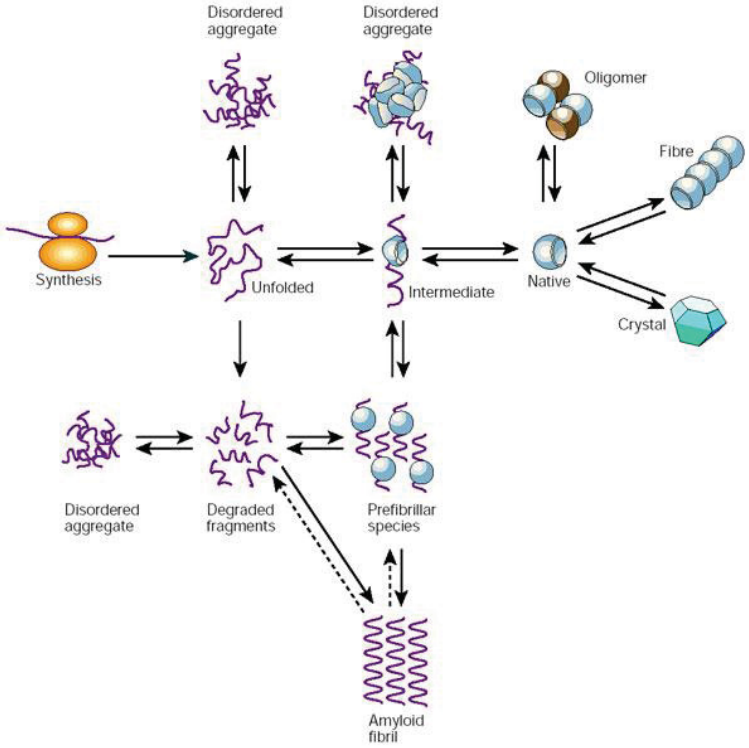

Figure 1.3: Schematic representations of protein folding, misfolding, unfolding and aggregation processes[2].

The key question for the protein aggregation is where, when, why and how the aggregation does take place. In different organs, for instance, liver and brain, both extracellular and intracellular protein deposit are found symptomatic for different associated diseases. The typical intracellular aggregation occurs in Parkinson´s, Huntington´s, Amyotrophic Lateral

Sclerosis disease, while in Alzheimer´s, Creutzfeldt-Jakob´s and renal disease extracellular aggregations are observed. In Alzheimer disease both extracellular amyloid β and intracellular deposits of neurofibrillary tangles consisting of tau protein are found[7]. The reasons for protein aggregation are among others oxidative stress, excessive production or environmentally induced gene mutations, which result in a conformation changing of proteins. Despite the chaperones and the protein quality-control system in the cell aging could be also a reason for a decreased protection against protein aggregation[8].

The protein aggregation is actually the association of peptides or proteins into higher order structures, which are in the aspect of chemical kinetics more stable than the active subunits alone. The aggregation process follows at times simple pathway of reaction of two monomers A to dimer A_2 with reaction constant k_2 as first step. Through addition of further monomers to oligomers small species (A_3), amorphous aggregates, protofibrils and fibrils (A_n/A_{m+n}) could be formed with reaction constant k_{n} or oligomers on oligomers with reaction constant $k_{\mathrm{m+n}}$ depending on experimental conditions (see Eq. 1-4). An autocatalytic polymerization was supposed to explain the protein aggregation of amyloids[11].

$$A \overset{k_2}{\rightarrow} A_2 \tag{1}$$

$$A + A_2 \overset{k_3}{\rightarrow} A_3 \tag{2}$$

$$A + A_{n-1} \overset{k_n}{\rightarrow} A_n \tag{3}$$

$$A_n + A_m \overset{k_{n+m}}{\longrightarrow} A_{n+m} \tag{4}$$

The mechanism of protein aggregation especially in the earlier stage is still not clear, although the equilibrium between monomer and small oligomers, such as dimer, trimer, and pentamer, have been obtained in the lag phase[12,13]. In comparison to polymers the amino acid side chains with various properties lead to a more complicated aggregation mechanism. Aside from monomer addition, elongation, fragmentation and branching have been observed during the protein aggregation processes[21-24]. Moreover due to the weak hydrogen bonding in comparison to covalent binding, even a slight variation of the environment could change the association. The aggregation pathway is influenced among others by temperature, pH, buffer composition and the concentration of the proteins. Oosawa *et al.*[18], Ferrone *et al.*[19] and Flyvnjerg *et al.*[20] proposed the aggregation mechanisms of equilibrium-nucleation for actin, the homogenous-, heterogeneous-nucleation for Sickle-cell haemoglobin and downhill

polymerization for tubulin, respectively. Depending on the nucleation pathway the growth of fibril follows the exponential-law, power-law or square of time. Lately, a simple two-step model was suggested by Finke-Watzky *et al.* to calculate the reaction constant of the aggregation of G-actin with the assumption of similar k_i after nuclei formation[21]. The whole aggregation processes could be reduced to two reactions: the formation of the nuclei and the fibrillization.

1.2 Amyloid beta protein (Aβ)

So far more than 20 neurodegenerative diseases like Alzheimer, Huntington, Prion and Parkinson are believed to be related to protein aggregation[22–27]. Aβ (Alzheimer diabetes), IAPP (Typ II diabetes), α-synuclein (Parkinson´s disease), prion (Creutzfeldt-Jakob disease) and Huntingtin (Huntington disease) are classified as amyloid protein, which deposits with histological staining properties similar to starch. The amyloid is characterized as protein fibrils with a cross beta-sheet quaternary structure, which was first described by Rudolf Virchow[28] and was further characterized firstly by Cohen and Calkins through electron microscopy (EM)[29], and by Kirschner through X-rays[30], where the cross β structure of fibril was observed.

The origin of Aβ

Amyloid beta (Aβ) is a small protein consisting of 39-43 amino acids, which is supposed to be associated with Alzheimer's disease (AD), which is one of the common neurodegenerative disorders with symptoms of memory loss and deficits in cognitive behaviour[31]. So far worldwide more than 35 million patients suffer from AD, and this number will increase up to 115 million in 2050[32]. The most important risk factor for AD is aging. People over 65 have a 90 % chance to develop AD. Additionally, early-onset forms of AD exist, which are related to familiar Alzheimer, where genes involved in Aβ metabolism, like presenilin 1, presenilin 2 or the amyloid β precursor protein carry mutations [33–36]. At the beginning of 20th century AD was considered as a normal effect of aging that is associated with shrinkage of prefrontal cortex and hippocampus until extra- and intra-cellular deposits were detected and linked to AD. The intracellular neurofibrillary tangles consist of fibrils of hyperphosphorylated tau, whereas in the extracellular plaques Aβ protein was found as the main component (see figure 1.4)[31].

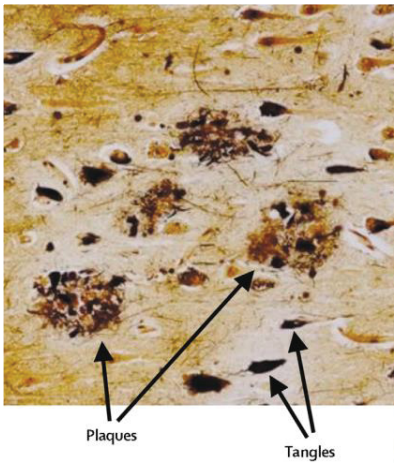

Figure 1.4: Hallmarks of Alzheimer disease. The intracellular tangles consist of τ protein, whereas Aβ protein is the main component of neurotic plaques [31].

In the amyloid cascade hypothesis the Aβ plays a central role in the disease pathology due to the high content of Aβ peptide in the neuritic plaques[7]. It is suggested that an excessive production combined with a decrease of Aβ degradation, especially $A\beta_{1\text{-}42,}$ leads to protein aggregation. In the earlier time of AD investigation the Aβ fibril is supposed to be responsible for the AD due to the capability to destroy cell membranes, whereas current evidences showed that some kinds of soluble amyloid oligomers could also create membrane pores and are the agents for the death of nerve cells. It is reported that the soluble Aβ oligomers can bind the NMDA-, insulin-, NGF- and frizzled-receptor, which leads to oxidative stress, decrease of the amount of synapse/insulin-receptor and hinder Wnt signalling, respectively[37–40,40–43]. Moreover it is supposed that Alzheimer disease and Parkinson´s disease (α-synuclein) are associated with each other[44]. Hence, the understanding of the reason as well as the mechanism of Aβ self-assembly is not only significant for the knowledge of AD but also for the amyloid proteins pathology and the prevention or treatment of the associating disease.

Aβ structure

Aβ is a fragment of a transmembrane glycoprotein, amyloid β-precursor-protein (AβPP) consisting of 265~770 amino acids. Figure 1.5 shows the longest isoform of AβPP with Kunitz-type protease inhibitor and OX-2 antigen domain binding at the N-terminus outside of the membrane[31]. There are two proteolytic pathways of AβPP: the amyloidogenic pathway with the γ- and β-secretase and the non-amyloidogenic pathway with α- and γ-secretase. Aβ

protein is generated by the abnormal proteolysis of AβPP through the amyloidogenic pathway. The gene mutation of AβPP on chromosome 21 is supposed to link to the familiar AD.

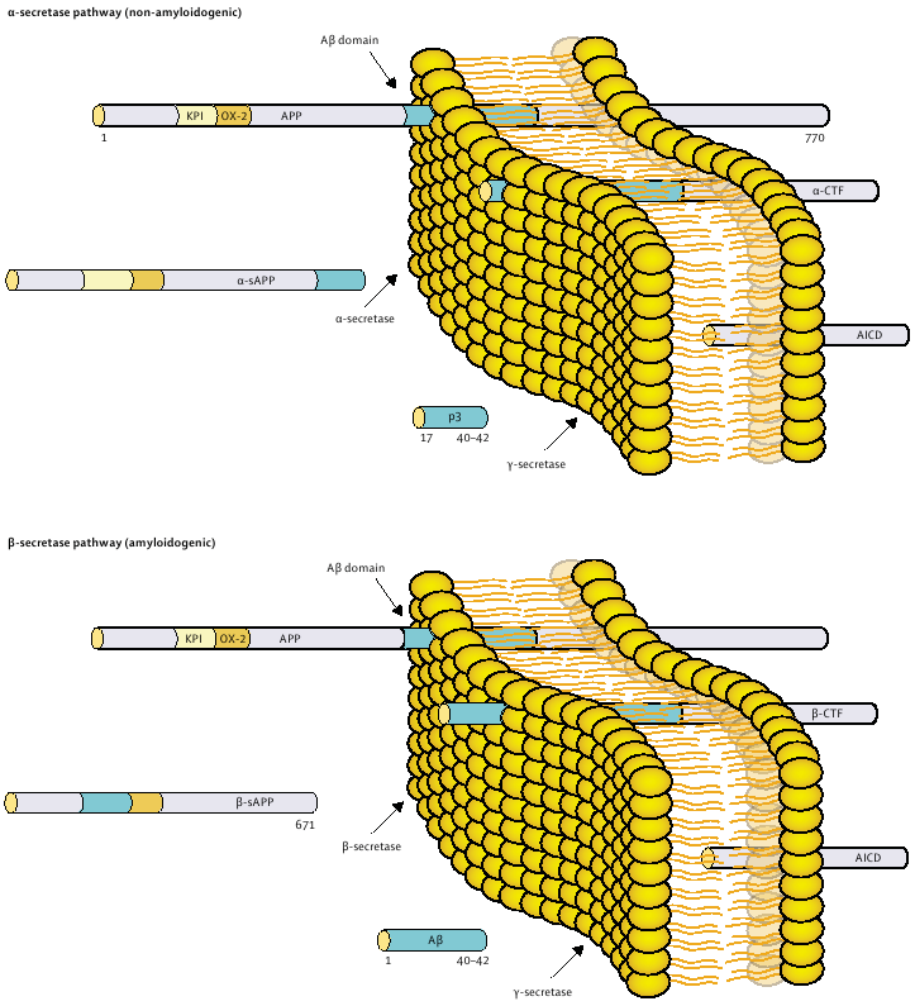

Figure 1.5: Schematic representation of proteolysis of amyloid precursor protein[31]. The left side with AβPP reveals the outside of membrane. The non-amyloidogenic α- and γ-secretase produce the nontoxic p3 and sAPPα, whereas the amyloid beta protein is produced by amyloidogenic β- and α-secretase. The γ-secretase cleaves the APP within the membrane and generates different Aβ isoforms.

The extracellular β-secretase produces the nontoxic β-sAPP and the N-terminal part of Aβ, while γ-secretase cleaves between Val40 and Ile41 or Ala42 and Tyr43 within the membrane region generating the AICD and the C-terminal part of Aβ. There are only three amino acids (residues 12 to 14) inside the transmembrane region. Different isoforms with lengths of 36-43 amino acid residues are produced. The most common isoforms of Aβ are $A\beta_{1\text{-}40}$ and $A\beta_{1\text{-}42}$, where $A\beta_{1\text{-}40}$ is more common than $A\beta_{1\text{-}42}$, but $A\beta_{1\text{-}42}$ exhibits stronger fibrillogenic

and toxic capabilities. The non-amyloidogenic cleavages, by α- and γ-secretase, produce the intracellular fragment AICD and the nontoxic α-sAPP and p3 outside of the membrane (see figure 1.5)[31]. Because the α-secretase cleaves within the Aβ region, the production of Aβ is prevented in non-amyloidogenic pathway.

Aβ is a hydrophobic protein with residues Leu17-Ala21 function as hydrophobic centre. The residues from Lys28-Ala42 and Gly9-Ala21 are suggested to be capable to form α or β secondary structure, wherein the residues Lys28-Ala42 tend to form β-sheet[45,46]. There are two β-turn regions in Aβ protein with residues from His6-Ser8 and from Asp23-Asn27. In organic solvent Aβ monomers prefer to be folded, whereas in aqueous environment the structure is mostly random coil.

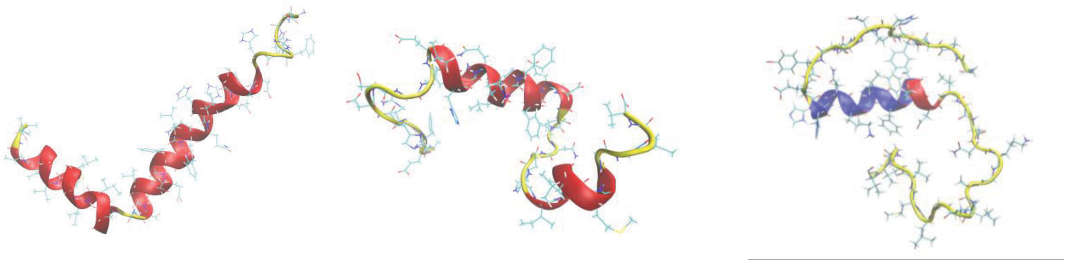

Figure 1.6: 3D NMR structure of $A\beta_{1-42}$ monomer in d-$HFIP_{0.8}D_2O_{0.2}$ (PDB code 1IYT, left), $A\beta_{1-40}$ monomer in $TFE_{0.4}H_2O_{0.6}$ (PDB code 1AML, middle) and $A\beta_{1-40}$ monomer in aqueous environment (20 mM K_3PO_4 + 50 mM NaCl, pH=7.3) (PDB code 2LFM, right)[47-49]. All three PDB files were treated by VMD software and presented in New-Cartoon style with red for α-helix; yellow for turn/random coil and blue for 3^{10}-helix.

The 3D structure of Aβ monomer in various solvents has been obtained by solution NMR[47–49] (see figure 1.6). In d-$HFIP_{0.8}D_2O_{0.2}$ $A\beta_{1-42}$ has two α-helical regions from residues Ser8-Gly25 at the N-terminus and from Lys28-Gly38 at the C-terminus with a type I β-turn between them, which is similar to $A\beta_{1-40}$ in $TFE_{0.4}H_2O_{0.6}$. The two α-helices of $A\beta_{1-40}$ are from Gln15-Asp23 and from Ile31-Met35 connected by a type I β-turn. Due to the relative high content of random coil between the two α-helices $A\beta_{1-40}$ monomer in organic solvent is more flexible than $A\beta_{1-42}$. In contrast, in aqueous environment (20 mM K_3PO_4 + 50 mM NaCl, pH=7.3) $A\beta_{1-40}$ monomer has only one 3^{10}-helix from residues His13-Asp23 in the middle but two random coil regions (see figure.1.6 right), which renders it more prone to aggregation than in $TFE_{0.4}H_2O_{0.6}$.

The conformational transition of Aβ monomer from α-helical to β-sheet structure is considered as the first step of aggregation and has been investigated by different methods. A

reversible conformational change between α- and β-structure has been observed by varying the fraction of water in dHFIP[50]. An increase of water percentage in d-HFIP leads to the transformation from α- to β-structure, which is reversible, if dHFIP is added again[50]. Moreover, time resolved CD experiments showed that the higher the temperature and ionic strength the faster the conformational transition to β-structure[51].

Figure 1.7 shows the 3D NMR structure of $^{35Mox}A\beta_{1-42}$ fibril with oxidized Met at residues 35[52]. The fibril has one random coil region from residues Asp1-Leu17 and two intermolecular β-sheets from residues Val18-Ser26 and from residues Ile31-Ala42[52]. In amyloid fibrils the hydrogen bonding direction runs parallel to the fiber axis. The diameter of the fibrils is between 7 and 12 nm. The $A\beta_{1-40}$ fibrils in the brains of Alzheimer patients have been investigated by solid state NMR and TEM[53]. The structure of fibrils varies in different patients.

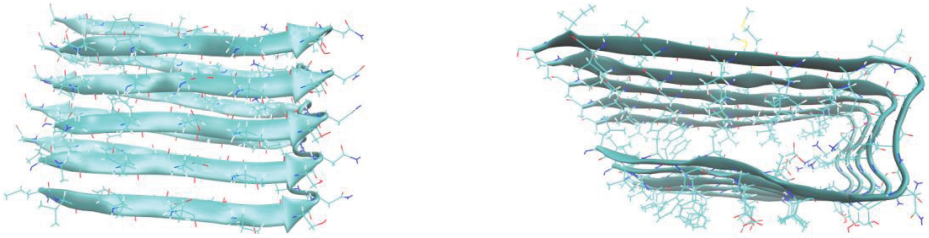

Figure 1.7: 3D NMR structure of $^{35Mox}A\beta_{1-42}$ fibril in side view (left) and top view (right) (PDB code 2BEG)[52]. The β-strands are perpendicular to the fibril axis. The residues from Val18-Ser26 and residues Ile31-Ala42 are the intermolecular β-sheets. The random coil region is from residues Asp1-Leu17.

Aβ fibrillation

In the earlier time of research, a nucleation like mechanism derived from crystallization with formation of nuclei through monomer association in the lag phase and fibrillization in the growth phase was used to explain the aggregation of amyloid proteins. In comparison to nucleation the fibrillization is much faster and depends weakly on the monomer concentrations. By using Thioflavin T (ThT) fluorescence measurements the lag time and the rate of growth can be determined by evaluation of a sigmoidal growth[54], where the fluorescence signal is proportional to the amount of amyloid structure.

The nuclei are defined as particles with critical radius r_{crit}. Aggregates with $r < r_{crit}$ are not stable and will dissociate shortly after formation, while those with $r > r_{crit}$ continue to grow. Nucleated polymerization is a process of monomer addition to a nucleus. The critical

radius r_{crit} of nuclei can be determined by the change of total free energy consisting of two parts: surface and volume contributions as shown in figure 1.8. The expansion of an aggregate leads on the one hand to a decrease of ΔG_{volume} but on the other hand a growth of $\Delta G_{surface}$. The critical radius is derived at the maximum from the change of the total free energy and depends both on the concentration and temperature.

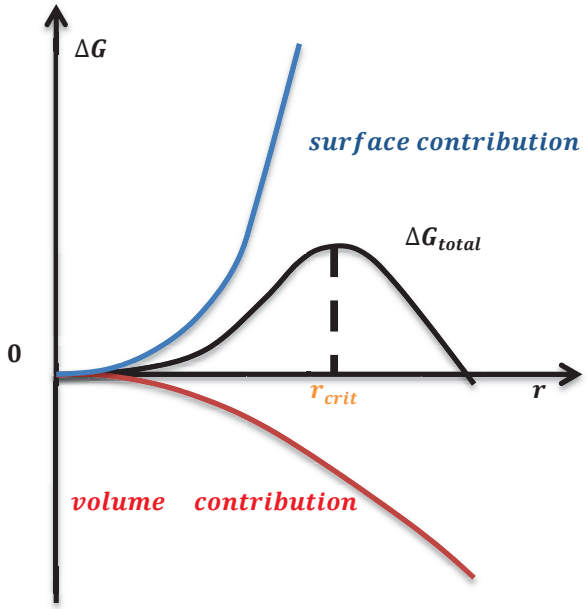

Figure1.8: Change of total free energy ΔG_{total}. The total free energy consists of the surface formation $\Delta G_{surface}$ and the volume transition ΔG_{volume}. A growth of particle leads to a raise in $\Delta G_{surface}$ but a decrease of ΔG_{volume}, which creates a maximum in the total free energy, which marks the critical radius of nuclei.

Current exploration suggests, except for the classical nucleation process the nucleus can also be formed by conformational rearrangement of oligomers, monomer coagulation, and branching, fragmentation of fibrils showed in figure 1.9[55]. Alternatively, nucleus formation can also be catalyzed by the surface of a fibril, which is defended as secondary growth processes and described as heterogeneous nucleation (see figure 1.9[55]). Furthermore it is suggested that the conformational change of monomer and oligomers in the lag phase can be depicted through nucleation or pre-nucleation processes, which depend particularly on the monomer concentration (see figure 1.9[55]). In contrast, the formation of fibrils is less related to the monomer concentrations.

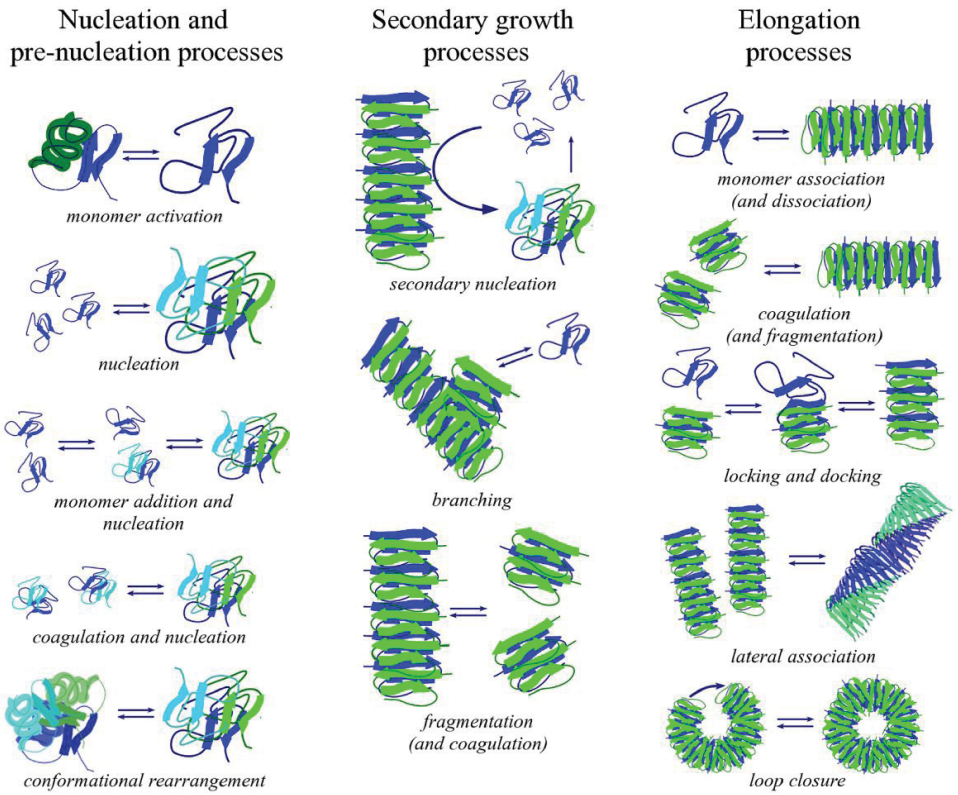

Figure 1.9: Schematic representation of mechanism of amyloid formation consisting of nucleation/pre-nucleation, secondary growth and elongation processes[55]. The formation of nuclei occurs throughout the whole aggregation process.

The amyloid formation therefore is supposed to be modelled by nucleation/pre-nucleation, secondary growth and elongation processes[55]. Both in the nucleation/pre-nucleation and secondary growth process the formation of nuclei occurs, while in the secondary growth process the fibril is involved. The fibril catalyzed nucleation is a competition process to fibril growth through monomer addition. Depending on the experiment conditions one of the processes is preferred. In most cases both processes occur parallel. In the elongation processes fibril elements will grow through the addition of monomer or nuclei to the end of fibril elements, which will self-assemble further to fibril. The lateral association of fibril elements results in straight fibrils, whereas the loop closure leads to annular aggregates. X-ray diffraction and TEM experiments showed that the fibrils consist of twisting protofibrils[56–58]. Moreover it is supposed that each process in the aggregation pathway is reversible. The dissociation of monomers from protofibrils has been observed by AUC experiment [59].

1.3 The mechanism of Aβ aggregation

The pathway from monomer to fibril is strongly correlated to the different factors such as, temperature, pH value, the concentration of metal ions, salts and the proteins[60]. Although the basic pH (NaOH or NH_4OH solvent, pH>10) is used to achieve monomeric Aβ solution, aggregation at basic condition (pH=8) close to physiological pH value (pH=7.4) has been observed by AFM[61]. After 8 h incubation at 30°C at pH=8 protofibrils and two kinds of low molecular weight oligomers were formed showed by time resolved AFM. The small oligomers are globular or disc-shaped aggregates with heights between 0.5-0.9 nm and widths between 5-10 nm, while the larger ones have heights between 1-2 nm and widths between 15-25 nm. At lower pH tube like aggregate tend to be formed[62], whereas neutral environment induces amyloid fibril formation.

Moreover, it is also shown that the coordinative binding of metal ions like Fe^{3+}, Zn^{2+} and Cu^{2+} by the three histidine residues of Aβ can induce rapid aggregation[63,64] influenced by pH value and metal concentrations[59,65–71]. The interaction between Zn/Cu metal ions and insulin degrading enzyme as well as neprilysin can decrease the degradation of Aβ monomers/oligomers and thereby accelerates the plaques formation[72].

Depending on experimental conditions nuclei and oligomers with various sizes and shapes, for example amyloidogenic- and unstructured-oligomers, can be formed by self-assembly of misfolded or denatured monomers at the same time in the lag phase (see figure 1.10)[73]. In some hypotheses it is suggested that soluble small oligomers such as dimer, pentamer and hexamer are stable and preferentially formed in the early stage, which can dissociate into native monomers again during the aggregation processes [74]. Such small oligomers function later in the phase of fibril growth as source of monomers. In a three-stage kinetic model for the insulin aggregation hexamer is proposed to be the most stable small oligomer in solution[75].

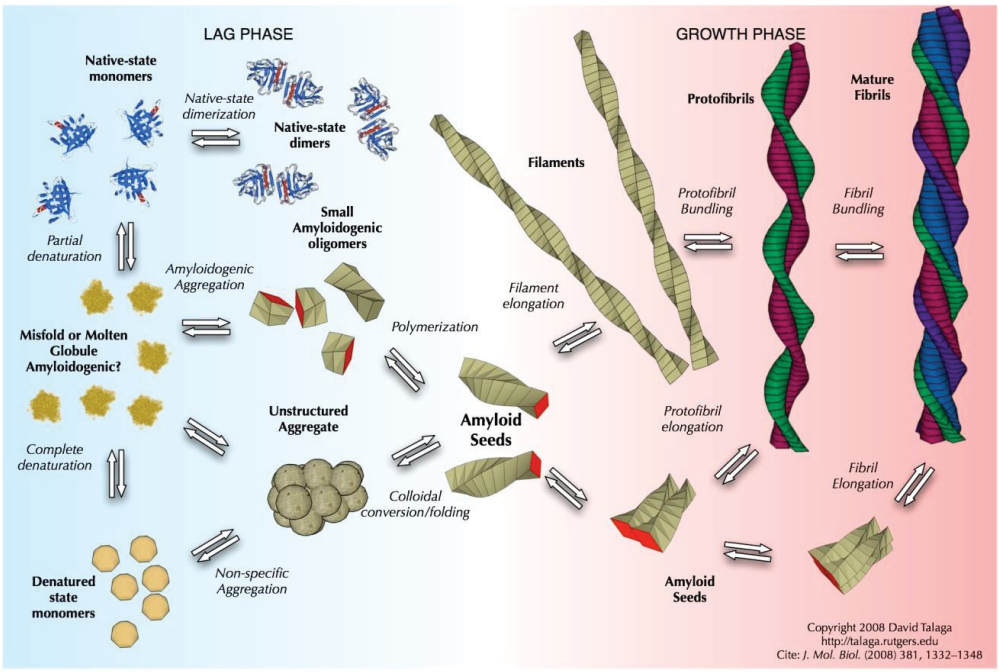

Figure 1.10: Schematic representation of the mechanism of amyloid protein aggregation. In the lag phase monomers aggregate to amyloid nuclei, oligomer and amyloid seeds, while protofibril and fibril form through elongation in the growth phase at later stage[73].

It is supposed that there exists a so-called critical concentration $C_{critical}$[76]. The aggregation can only take place when the monomer concentration is higher than $C_{critical}$[76]. In a healthy human brain the Aβ concentration is normally too low to induce self-assembly. Naturally, the excessive production of Aβ is therefore considered as one of the main causes of Alzheimer disease. The critical concentration $C_{critical}$ is strongly correlated to the experimental conditions.

Four models are among others discussed for Aβ aggregation: first, the classic nucleation like model with fibril formation via addition of monomer on preformed nuclei, seeds or micelles, second, the oligomer conversion through conformational change from unstructured oligomers to β-sheet rich structures, third, association through secondary nucleation, and fourth, self-assembly through formation of paranuclei followed by protofibril/fibril formation (see figure 1.11)[77].

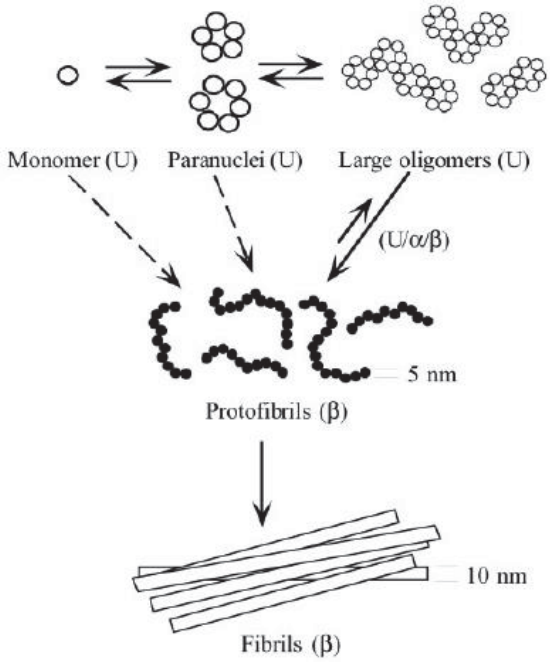

Figure 1.11: Self-assembly of Aβ from monomer to fibril via paranuclei and oligomer conversion[77]. Pentamer/hexamer is supposed as paranuclei for $A\beta_{1-42}$, which is considered to be the buildings block of aggregation.

In the paranuclei associated mechanism small oligomers from dimer to hexamer will be formed in the lag phase as building blocks of 12-, 18- and 24-mer, which can self-assemble into larger oligomers and protofibrils showed in figure 1.11[77]. The amyloid fibrils consist from 2-5 protofibrils, which are twisted with height of ~4.3 nm and period of ~20 nm[78]. The diameter of protofibrils is about 5 nm and around 10 nm for fibrils. The building block is defined as paranuclei. It is supposed that the pentamer/hexamer could be the paranuclei in the association of Aβ.

Figure 1.12 shows the hexamers of $A\beta_{1-40}$ and $A\beta_{1-42}$ in 10 mM HEPES buffer (pH=7.4) obtained by AFM [79,80]. Interestingly, the six subunits of hexamer are hardly distinct from each other. In spite of small size the pore in the middle of oligomers is clear to see. The hexamers of $A\beta_{1-40}$ and $A\beta_{1-42}$ have a disk-like shape and channel-like structure in common. The $A\beta_{1-40}$ hexamer has an outer diameter of 16 nm, a pore of about 2 nm and thickness between 1 nm and 2 nm[79]. The outer diameter of $A\beta_{1-42}$ hexamer is between 8 nm and 10 nm[80].

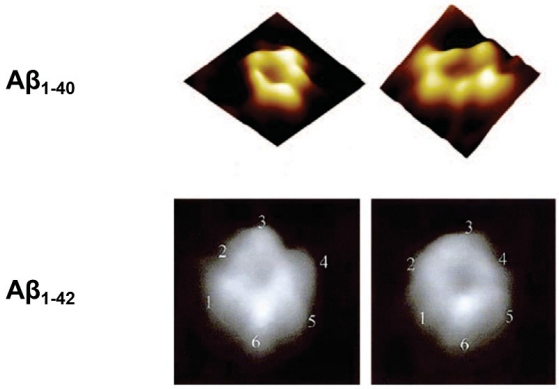

Figure 1.12: High resolution AFM images of Aβ hexamer [79,80]. The hexamers of Aβ have a disk-like shape with a pore in the middle. It appears that the six subunits of hexamers are distinct from each other.

At physiological conditions (pH= 7.4) small oligomers (or paranuclei) in the lag phase can be stabilized at low temperature (4°C)[81]. NMR, FTIR, TEM and AFM can be therefore performed to study the structure of oligomers. Two main populations were found: disc like pentamer with widths between 10 nm and 15 nm and thickness of about 2 nm, oligomers with thickness between 3 nm and 4 nm and same widths as pentamer, which could be undecamers or dodecamers associated from pentamer[81]. High resolution NMR showed the monomers in the pentamer are extreme compact and different from the monomers in the fibril. Three turns between residues His13-Gln15, Gly25-Gly29 and Gly37-Gly38 and a binding between residues Phe19-Leu34 were found in the monomer unit of pentamer. In contrast there is only one turn between two hydrophobic regions in the monomer within fibrils. A conformation changing is therefore supposed[81].

In 2001 Bitan *et al.* isolated and defined the ´Low Molecular Weights´ (LMWs) oligomers of Aβ by size exclusion chromatograph (SEC) and filtration through 10,000 molecular weight cut-off (MWCO) filter[82]. The isolated LMWs oligomers of $A\beta_{1\text{-}40}$ are a mixture from monomer to tetramer, which are in equilibrium after preparation, whereas the isolated LMWs oligomers of $A\beta_{1\text{-}42}$ are from monomer to octamer, which tend to aggregate[77]. Later it is shown the self-assembly of $A\beta_{1\text{-}42}$ and $A\beta_{1\text{-}40}$ is therefore distinct from each other[77]. Although the protofibrils were formed at later stage the formation of paranuclei of $A\beta_{1\text{-}40}$ were much later than $A\beta_{1\text{-}42}$. In comparison to LMWs oligomers the ´High Molecular Weights´ (HMWs) oligomers are β-sheet rich aggregates with 40-200 kDa in molecular weight[83].

The mechanism of $A\beta_{1\text{-}40}$ fibrillzation in 0.1 mM HCl at various concentrations has been studied by DLS and reported by Lomakin *et al.*[84]. A critical concentration $c_{critical}$ was

suggested. Below it ($c < c_{critical}$) the fibrillation follows heterogeneous nucleation with monomer addition to seeds (see figure 1.13 B[84]), whereas above it ($c > c_{critical}$) the amyloid fibril with radius about 4 nm will be formed by addition of monomer to nuclei, which are generated from preformed Aβ micelles with a hydrodynamic radius R_H of 7 nm in the lag phase showed in figure 1.13 A[84].

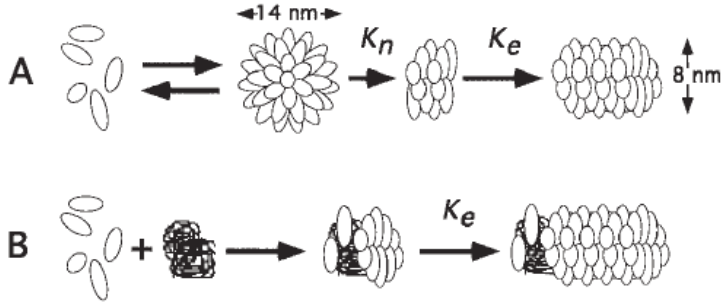

Figure 1.13: Self-assembly of $A\beta_{1\text{-}40}$ in HCl[84]. A: aggregation at higher concentration through addition of monomer to nuclei being generated from Aβ micelle. B: aggregation at lower concentration via addition of monomer to Aβ seed.

Furthermore SANS experiments of amyloid beta micelles at different concentrations between 5.0 mg/ml and 0.31 mg/ml were carried out to study the aggregation of $A\beta_{1\text{-}40}$ in 0.1 mM HCl[85]. The SANS pattern in log-log scale was modelled as spherocylinder (a cylinder with hemispheres as endcaps of length L and radius R, see figure 1.14)[85]. SANS experiments revealed that the micelle has a radius of about 2.4 nm and length of about 11 nm, which is independent from the protein concentration. Moreover, as expected, the lower the concentration the lower the forward scattering intensity and the higher the error at high scattering vector Q($Å^{-1}$) (see figure 1.14)[85]. At 0.05 mg/ml below critical concentration $C_{critical}$ ($C_{critical}$≈0.1mM) it is not possible to detect the micelle in solution.

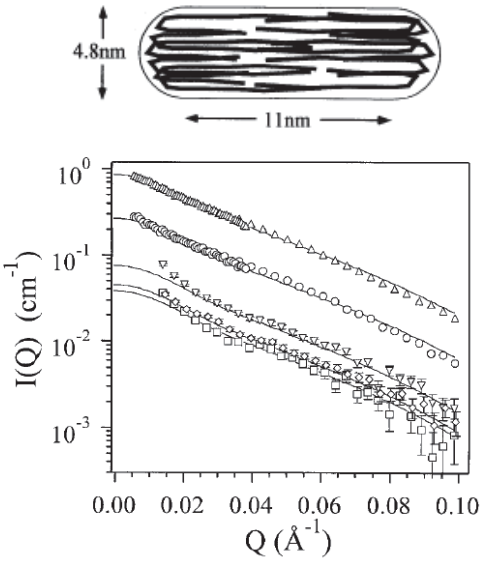

Figure 1.14: SANS pattern and corresponding analytical model of Aβ micelle in 0.1 M DCl at different protein concentrations (5.0 mg/ml (Δ); 2.2 mg/ml (O); 0.6 mg/ml (∇); 0.4 mg/ml (◊); 0.31 mg/ml (□))[85]. The SANS curves were modeled by spherocylinder with cylinder length *L* and endcap radius *R*.

The aggregation mechanism of $A\beta_{1\text{-}40}$ in phosphate-buffered saline (pH=7.4) was studied by time-resolved dynamic light scattering (DLS) and static light scattering (SLS). It is demonstrated that the self-assembly is irreversible and follows diffusion-limited aggregation[66]. In 2001 Murphy *et al.* draft a mathematical model for the fibril growth of $A\beta_{1\text{-}40}$ in phosphate-buffered saline, which was investigated by light scattering and size exclusion chromatography[86]. In 2000 a simple mathematical model based on a micelle-nuclei-fibril directed self-assembly process was developed by Saitô *et al.* to analyze human calcitonin[87], which was later applied to study the aggregation of Aβ by Sabate *et al.*[11].

1.4 The topic of the work

Because of the rapid fibrillation and the overlapping different pathways the applicable methods for Aβ investigations are limited. The lower protein concentrations and low molecular weight of monomers and small oligomers at the beginning of the association pose challenges for most analytical methods. The common methods for the study of Aβ are NMR and X-ray diffraction for the high resolution structure; CD and FTIR for the secondary structure estimation; transmission electron microscopy (TEM) and AFM for morphological study of aggregates; analytical ultracentrifugation (AUC) and DLS for the hydrodynamic properties of aggregates at various sizes in solution; and ThT-fluorescence measurements for

the kinetic investigation. Small angle scattering techniques (SANS, SAXS) are useful to characterize particles in solution such as polymers and nanoparticles in a wide size range from several nanometres to micrometres, which provides a superior possibility to investigate the self-assembly of protein, where both monomers and aggregates in different sizes are exist. Depending on the particle size and shape monomer and dimer can be distinguished from each other.

In comparison to neutron scattering, high intensity SAXS has the advantage to require only small sample volumes, relatively low concentrations. Further, it allows studying fast kinetics, which would be useful for Aβ aggregation. Nevertheless, SAXS is seldom used due to the protein damage and acceleration of the aggregation process[88]. The main objective of this work focusses on the investigation of Aβ oligomerization by using SANS and DLS. Through complementation by AUC and AFM a more quantitative picture of Aβ aggregation will be developed. The challenge for this work is among others sample preparation and experiment design. Because the scattering intensity plays a decisive role for the structure estimation, a normal protein concentration for SANS experiment is above 10 mg/ml, which is unsuitable for aggregation study. Considering the concentration requirements of the applied methods (SANS, DLS, AUC, CD) the experiments were performed at a concentration range between 1 mg/ml and 0.001 mg/ml in this work. Moreover, in order to rise the scattering intensity long-time experiments (8 h per sample) were carried out for SANS. Additionally, low temperature (7°C) close to freeze point of heavy water (3.8°C) was applied to slow down the aggregation process and stabilize the performed small oligomers in the lag phase.

To get the insight into the aggregation pathway in the lag phase a monomeric sample is important, Hence, as the first attempt we probed the Aβ monomers at different solutions, such as d-HFIP[89], basic environment (0.1 M NaOH), 0.1 M HCl and physiological conditions (0.05 M Napi+0.15 M NaCl, pH=7.4) in order to find suitable experimental conditions for aggregation study by scattering methods.

To study the self-assembly pathway we choose $A\beta_{1-42}$. Even though $A\beta_{1-40}$ is the most common isoform of amyloid beta protein, $A\beta_{1-42}$ is suggested to play the central role in the pathology of AD because of its higher toxicity. At various concentrations and temperatures (7°C-37°C) time resolved SANS, DLS, AFM and AUC were performed under physiological conditions (0.05 M Napi+0.15 M NaCl, pH=7.4), whereas the SANS experiments were carried out only at 7°C.

2. Experimental results

2.1 Monomeric amyloid beta peptide in hexafluoroisopropanol detected by small angle neutron scattering

Bo Zhang-Haagen[1,3], Ralf Biehl[1], Luitgard Nagel-Steger[2,3] , Aurel Radulescu[4], Dieter Richter[1], Dieter Willbold[2,3],

Status: published in PLOS ONE

Impact Factor: 3.23

Proportion of contribution: 80%

Contributions: Conceived and designed the experiments; performed the experiments; Analyzed the data; Wrote the paper.

PLOS | ONE

RESEARCH ARTICLE

Monomeric Amyloid Beta Peptide in Hexafluoroisopropanol Detected by Small Angle Neutron Scattering

Bo Zhang-Haagen[1,2], Ralf Biehl[1]*, Luitgard Nagel-Steger[2,3], Aurel Radulescu[4], Dieter Richter[1], Dieter Willbold[2,3]

1 Jülich Centre for Neutron Science & Institute of Complex Systems, Neutron Scattering (JCNS-1&ICS-1), Research Centre Jülich, Jülich, Germany, **2** Institut für Physikalische Biologie, Heinrich-Heine-Universität Düsseldorf, Düsseldorf, Germany, **3** Institute of Complex Systems, Structural Biochemistry (ICS-6), Research Centre Jülich, Jülich, Germany, **4** Jülich Centre for Neutron Science, Outstation at MLZ (JCNS-MLZ), Research Centre Jülich, Garching, Germany

* ra.biehl@fz-juelich.de

Citation: Zhang-Haagen B, Biehl R, Nagel-Steger L, Radulescu A, Richter D, Willbold D (2016) Monomeric Amyloid Beta Peptide in Hexafluoroisopropanol Detected by Small Angle Neutron Scattering. PLoS ONE 11(2): e0150267. doi:10.1371/journal.pone.0150267

Editor: Jie Zheng, University of Akron, UNITED STATES

Received: December 22, 2015

Accepted: February 11, 2016

Published: February 26, 2016

Data Availability Statement: All relevant data are within the paper and its Supporting Information files.

Funding: These authors have no support or funding to report.

Competing Interests: The authors have declared that no competing interests exist.

Abstract

Small proteins like amyloid beta (Aβ) monomers are related to neurodegenerative disorders by aggregation to insoluble fibrils. Small angle neutron scattering (SANS) is a nondestructive method to observe the aggregation process in solution. We show that SANS is able to resolve monomers of small molecular weight like Aβ for aggregation studies. We examine Aβ monomers after prolonged storing in d-hexafluoroisopropanol (dHFIP) by using SANS and dynamic light scattering (DLS). We determined the radius of gyration from SANS as 1.0±0.1 nm for $A\beta_{1-40}$ and 1.6±0.1 nm for $A\beta_{1-42}$ in agreement with 3D NMR structures in similar solvents suggesting a solvent surface layer with 5% increased density. After initial dissolution in dHFIP Aβ aggregates sediment with a major component of pure monomers showing a hydrodynamic radius of 1.8±0.3 nm for $A\beta_{1-40}$ and 3.2±0.4 nm for $A\beta_{1-42}$ including a surface layer of dHFIP solvent molecules.

Introduction

A common pathologic hallmark of neurodegenerative disorders like Alzheimer's, Parkinson's or Huntington's disease is the existence of amyloid deposits in the brain[1–6]. Amyloid is generated by abnormal protein aggregation leading to formation of insoluble protein fibrils with a highly ordered cross-beta sheet structure. At the beginning of the 20th century beta amyloid protein (Aβ) was supposed to be associated with Alzheimer disease (AD) in consequence of the detection of Aβ fibril in intercellular plaques found in brain of AD patients[7]. Aβ fibrils and soluble oligomers are suggested to be responsible for the disease symptoms, whereas the monomers in the brain of AD patients are considered as nontoxic[8–10]. Aβ is a hydrophobic protein with 39–43 amino acid residues, which is produced by proteolytic cleavage of amyloid precursor protein (APP) associated with the cell membrane[11]. The γ-secretase, within the membrane region, generates the fibrillogenic C-terminus of Aβ[12] and may cause an amount of isoforms dependent on the exact position for cleavage, where $A\beta_{40}$ and $A\beta_{42}$ are the most

common, while the extracellular β-secretase cleaves N-terminally. The residues Leu17-Ala21 constitute the hydrophobic core of Aβ. The residues Lys28-Ala42 and Gly9-Ala21 are capable to form α-helical or β-sheet structure, where the *β*-sheet is the priority for Lys28-Ala42[13,14]. As the key of AD investigation Aβ monomers have been studied by different methods as nuclear magnetic resonance (NMR), analytical ultracentrifugation (AUC), circular dichroism (CD) and Fourier transform infrared spectroscopy (FTIR)[15–18]. In aqueous environment the monomeric Aβ is mainly unstructured[19], whereas apolar solvents induce a folded, α-helical structure[20,21]. The conformational change to β-sheet is supposed as the first step of the aggregation process and has been observed by CD and NMR spectroscopy by increasing the content of water in apolar solvents (hexafluoroisopropanol (HFIP), trifluoroethanol (TFE)) [17,22,23]. The classic hypothesis of fibril formation suggests monomer addition to soluble oligomers or to the seeds for fibril formation, whereas current explorations propose firstly the assembly of oligomers and secondly the structural conversion to β-sheet structure as alternative[16]. A nucleation like mechanism was used to explain the fibrillation in former studies [24].

The fast conformational change with rapid onset of the aggregation process makes a study of the early stage of aggregation from monomers to small oligomers and fibril formation in aqueous solvents challenging. High-resolution structural methods fail to deliver the needed information to understand disease mechanism, therefore low-resolution methods are important to gain insight in structure and kinetics of the aggregation processes. Non-destructive methods like dynamic light scattering (DLS) either give limited amount of information (only hydrodynamic radius) or, like small angle X-ray scattering (SAXS) techniques, may have a strong influence on the aggregation due to radiation damage associated with high intensity X-ray sources. Methods like atomic force microscopy, analytical ultracentrifugation or transmission electron microscopy on the other hand give a snapshot of the aggregation process.

For all of the mentioned methods the preparation of the initial sample of Aβ is crucial as it defines the starting point for examination of aggregation pathways. Different methods involving alkaline or acidic solutions or organic solvents are regularly used[25–28]. Solvents with rich fluoride content as HFIP or TFE are known to produce stable amyloid protein monomer solution and may lead to monomer dissociation from protofibrils/fibrils or break up of preaggregates[28–30]. After re-purification and before the addition of aqueous buffers the proteins will be dried and consequently the protein concentration is much higher than in experiment before the complete evaporation of HFIP.

Neutron scattering, in contrast to X-ray scattering, shows no radiation damage or radiation induced aggregation even on delicate samples like unfolded proteins[31]. Small angle neutron scattering (SANS) accesses the same low-resolution structural information as SAXS with a different scattering contrast as X-rays interact mainly with the electrons of the atoms and neutrons interact with the nucleus[32,33]. The scattered intensity depends on the isotopes allowing contrast variation by isotope exchange[34] as e.g. using D_2O instead of H_2O to reduce the scattering of the solvent. SAXS and SANS are frequently used to determine the low-resolution structure of proteins and protein complexes in solution[32,35]. By inelastic neutron scattering methods the internal dynamics between domains on several nanosecond timescale or the sidechain motions on picosecond timescales can be observed[36,37].

So far, SANS was rarely used to study aggregates and aggregation kinetics of small peptides like Aβ or insulin, despite the advantage that it might reveal new structural information that is not accessible by other methods and in contrast to SAXS does not induce radiation damage in the sample[38–42]. Typically small angle scattering is used to determine the size or shape of larger aggregates during aggregation. Discrimination between populations of monomers, small oligomers and fibrils is challenging because of the low concentrations used in aggregation

studies below 1 mg/ml and limited solubility of the peptides. Additionally discrimination is only possible if clear differences between populations can be expected as in case of Aβ where monomers, oligomers and large fibrils are present[43,44].

To examine the possibilities and limitations of small angle scattering techniques to observe the monomer to oligomer transition exploiting the nondestructive character of neutrons as a probe for delicate proteins, the monomer scattering is examined here as a limiting case for further aggregation studies. In biological relevant environment (H2O or D2O buffers) the Aβ monomer scattering is low and hardly to detect at lower concentrations as it is close to the SANS instrument noise and the fast aggregation introduces aggregates/oligomers masking a clear signal of the present monomers. Therefore we examined a monomeric solution in dHFIP to show what can be expected from the scattering signal and which effects need to be included in interpretation. This will help in the evaluation of aggregation studies by SANS to discriminate between monomers and oligomers. We examine here monomeric solutions of $A\beta_{1-42}$ and $A\beta_{1-40}$ as the most common peptides for Aβ aggregation studies at relative high concentration after incubation in dHFIP for several days. We observe a stable monomer population and a disappearing aggregate population by DLS and examine the monomeric solution by SANS. We demonstrate that SANS is capable to resolve monomeric Aβ with different radius of gyration for $A\beta_{1-42}$ and $A\beta_{1-40}$ and strong indications for a solvent surface layer bound to the peptides.

Materials and Method

Materials

The Aβ peptide was purchased as TFA salt with >95% purity (Bachem, Weil am Rhein, Germany). The deuterated 1,1,1,3,3,3-hexafluoro-2-propanol-D2 (dHFIP) was purchased from euriso-top (Saint-Aubin, France) with >99% purity. Aβ was dissolved in dHFIP in the purchased vials to yield a concentration of about 12 mg/ml dry mass including remaining salt or interfacial water from the protein powder. The peptide concentration was determined by UV absorption measurement (NanoDrop, Thermo Scientific, USA), applying an extinction coefficient at 280 nm of 1490 $cm^{-1}M^{-1}$, based on the single tyrosine residue of Aβ[45]. Final protein concentrations were about 5.6 mg/ml for $A\beta_{1-42}$ and about 2.4 mg/ml for $A\beta_{1-40}$. No further purification was done to prevent any additional decrease of concentration or material loss. Incubation and all measurements for $A\beta_{1-40}$ and $A\beta_{1-42}$ were performed at 20°C. SANS experiments were carried out after three weeks incubation in dHFIP.

Small Angle Neutron Scattering (SANS)

Experiments were performed at the high intensity SANS diffractometer KWS2 operated by Jülich Center for Neutron Science at Heinz Maier Leibnitz Zentrum (MLZ) in Germany at a wavelength $\lambda = 4.7$ Å with a wavelength spread of $\lambda/\Delta\lambda = 0.2$ [46]. The samples were measured in 1 mm quartz cells (Hellma Analytics, Germany) at sample-detector-distances 1.1 m and 5.6 m covering the range of scattering vector $Q = 4\pi/\lambda sin(\theta/2)$, with scattering angle θ, between 0.01 $Å^{-1}$ and 0.5 $Å^{-1}$. Samples and buffer measurements for background correction were measured for 1 h to 3 h dependent on detector distance. Appropriate standard methods for data evaluation and background correction were used.

The coherent scattering intensity of particles in solution with background contributions *bgr* is

$$I(Q) = \frac{N}{V} S(Q)F(Q) + bgr \quad (1)$$

with the number of particles N in the volume V. Background *bgr* contributions are due to

scattering from solvent and incoherent particle scattering. The interparticle interactions are subsumed in the structure factor $S(Q)$, which is for low concentrations equal one and is neglected in the following. The scattering of the protein configuration is described by the form factor $F(Q)$.

$$F(Q) = \sum_{i,j} \langle b_i b_j exp\,(iQ(r_i - r_j)) \rangle \tag{2}$$

with the atomic position vectors r_i and the atomic scattering lengths b_i relative to the displaced solvent scattering in the ensemble average $<\cdot>$[47]. The form factor is independent of the sample concentration and exhibits the particle shape, respectively the configuration. Additional scattering from a surface layer of solvent around the protein can be taken into account by assuming a layer of solvent with increased density compared to the bulk[47].

Models

The Beaucage function is a simple and common model being applied to analyze SANS data of objects with undefined geometry. It describes the Guinier region at low Q with radius of gyration R_g as a measure of size and a power-law at high Q with dimensionality d as measure of shape or configuration[48–50] as

$$\begin{aligned} F(Q) &= Gexp\left(-\frac{Q^2R_g^2}{3}\right) + \left(\frac{C}{Q^d}\right)\left[erf\left(\frac{QR_g}{\sqrt{6}}\right)\right]^{3d} \\ C &= \left(\frac{Gd}{R_g^d}\right)\left[\frac{6d^2}{(2+d)(2+2d)}\right]^{d/2}\Gamma\left(\frac{d}{2}\right) \end{aligned} \tag{3}$$

with the Guinier scaling factor G, the Porod scaling factor C, error function erf and Gamma function Γ. With $d = 2$ it is a good approximate for the Gaussian coil[50].

Atomic modeling is based on the atom positions of PDB structures and Eq 2 taking into account the scattering length difference relative to the solvent. To consider the excluded solvent scattering the solvent excluded volume V_{SES} needs to be determined. Therefore the protein solvent accessible surface (SAS) is calculated with a probe radius $R_p = 0.14$ nm resulting in volume V_{SAS} and surface area A_{SAS} as implemented in the used MMTK software[51,52]. As a fast approximate for V_{SES} we subtract the surface layer volume with a correction for overlapping regions in grooves determined from the additional surface area with half the probe size as $V_{SES} = V_{SAS}\text{-}R_p\times(A_{SAS}(R_p)+0.5(A_{SAS}(R_p)\text{-}A_{SAS}(R_p/2))$. The resulting specific volumes are 0.705 cm^3/g and 0.720 cm^3/g for $A\beta_{1-40}$ and $A\beta_{1-42}$ as average over the configurations in pdb structures 1IYT and 1AML, respectively. Both values are slightly smaller compared to reported values from analytical ultracentrifugation of 0.734 cm^3/g and 0.738 cm^3/g for $A\beta_{1-40}$ and $A\beta_{1-42}$[18,53]. With these increased values for the specific volume the resulting scattering would increase.

Dynamic Light Scattering (DLS)

Experiments were performed with a Zetasizer Nano ZS (Malvern Instruments, Worcestershire, UK). The instrument uses a He-Ne laser with $\lambda = 632.8$ nm and vertical polarization in backscattering geometry at 173°. The sample cell is a UV-Cuvette micro (BRAND, Wertheim, Germany) with 70 µl sample volume. To cover also larger aggregates (as the later third species) the measurements duration was set to 1h to get reliable data at long times. The auto correlation function was analyzed by non-negative least square (NNLS) algorithm[54] followed by protein analysis (L-curve)[55] as implemented in the instrument software. The result is an intensity

weighted distribution of hydrodynamic radius R_H in the sense of a relaxation time distribution where each relaxation time τ is interpreted via the Stoke-Einstein relation $R_H = k_B T/6\pi\eta D$ with the diffusion coefficient $D = (Q^2\tau)^{-1}$ and Q as the scattering wave vector, Boltzmann constant k_B, temperature T and solution viscosity η. The mean R_H and the width of the resulting distribution characterize a population. It should be noted that the typical noise of the measured auto correlation results in a distribution width of about 30% for an ideal monodisperse population. The error of a mean R_H is evaluated as standard deviation of repeated measurements. The volume fraction of a population can be evaluated from the volume-weighted distribution as calculated by the instrument software.

Results and Discussion

To examine the content of freshly in dHFIP dissolved Aβ powder we explored the evolution of the intensity correlation of $A\beta_{1-40}$ and $A\beta_{1-42}$ in dHFIP at 20°C by repeated DLS experiment. Shortly after dissolution three distinct particle populations can be observed (see Figs 1 and S1). The population with largest R_H belongs to peptide aggregates or fibrils (or contaminating dust particles) with sizes larger than several microns. The remaining two populations show mean relaxation times of about 20 μs and 5000 μs corresponding to hydrodynamic radii R_H around 2 nm and 500 nm, which are clearly separated in the auto correlation function as shown in Fig 1. The population with $R_H \approx 2$ nm and width typical for monomeric protein solutions refers to monomers. Analysis of the volume weighted distributions shows that the monomer population is the main component to the peptide content with more than 99% for all measurements. Accordingly the concentration as measured by UV-Vis absorption does not change significantly with time. The two larger populations refer to aggregates that strongly contribute to the scattering intensity because the scattered intensity is proportional to the sixth power of the particle size. During the observation time the size of the second population varied between 100 nm and 3000 nm, where the content fluctuated, but mainly shows a decrease of the scattering contribution. A change in size may be caused by monomer dissociation/aggregation from aggregates, fragmentation/aggregation of aggregates or faster sedimentation of larger aggregates. For the cases of dissociation, aggregation and fragmentation we expect an obvious change of size including sizes smaller than 100 nm (relaxation times $<$1000 μs), which is not observed in detectable amount. Therefore, we supposed that the dominating process for both larger aggregate species is sedimentation during the incubation in dHFIP. Changes of the aggregate contribution to the auto correlation may result from wobbling of the sample prior to the measurement. After about 9 days incubation in dHFIP there is no more larger change in the correlation function observable. The sample reached its equilibrium and contains hardly any larger aggregates. The small particles have a hydrodynamic radius of about 1.8±0.3 nm for $Aß_{1-40}$ and 3.2±0.4 nm for $Aß_{1-42}$.

Fig 2 shows the SANS scattering curves of Aβ in dHFIP. In spite of the relatively high concentrations—compared to aggregation studies with concentrations below 1 mg/ml—the intensity is quite low due to the small size of Aβ and about a factor of 3 below the background of pure dHFIP that is subtracted taking the protein volume fraction into account. A residual background at high Q is obvious, which is due to incoherent scattering from the protein (about 0.0025 cm^{-1} for the 5.6 mg/ml) and residual scattering from protonated water and salts in the purchased protein powder. The difference in forward scattering of about a factor of 3 corresponds mainly to the difference in concentration. Low intensity and residual background favour together a Beaucage model including a background over the classical Guinier analysis for Rg evaluation as the later does not include a background contribution[56]. The measured intensity was modeled by a Beaucage function with fixed dimensionality ($d = 2$) within a least

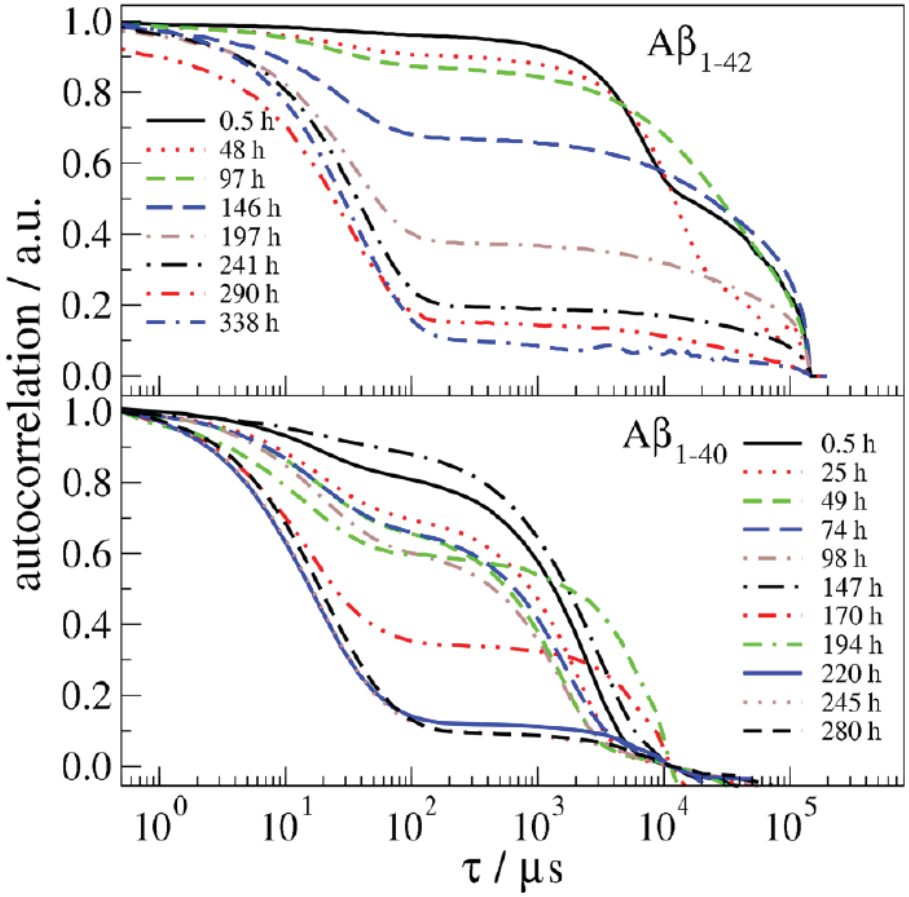

Fig 1. Time resolved DLS experiment of $A\beta_{1-42}$ and $A\beta_{1-40}$ in dHFIP. The samples were measured between 0.5 h and 14 days after initial incubation at 20°C. For $A\beta_{1-40}$ the value of $\tau = 10000$ μs is subtracted to focus on the two smaller species. For both samples correlations are normalized to 1 for $\tau \rightarrow 0$ to get a better overview over the data. Original measurements are found in S1 and S2 Figs.

doi:10.1371/journal.pone.0150267.g001

square fit including the residual background. The radius of gyration R_g evaluates to 1.6±0.1 nm and 1.0±0.1 nm for $A\beta_{1-42}$ and $A\beta_{1-40}$ respectively (see Fig 2A).

The 3D structure of $A\ß_{1-42}$ monomer in $dHFIP_{0.8}D_2O_{0.2}$ is available from the PDB data bank (PDB code 1IYT) as measured by solution NMR (see Fig 3A) with a set of 10 conformations, which show mainly reorientations due to a small hinge between the two α-helices[20]. For $A\beta_{1-40}$ a structure file (PDB code 1AML) measured in 40%TFE/water with 20 different conformations is available (see Fig 3B)[21]. The simulated scattering curves of the conformations are illustrated in S3 Fig and the averages are shown in Fig 2B as broken line for both structures. In both cases we find too strong scattering. Including the effect of a solvent surface layer with higher density compared to the bulk solvent comparable to the hydration layer observed for proteins in water[47] the calculated scattered intensity matches the measured intensity with an increase in density of 5% for a 0.3 nm thick solvent surface layer. The surface

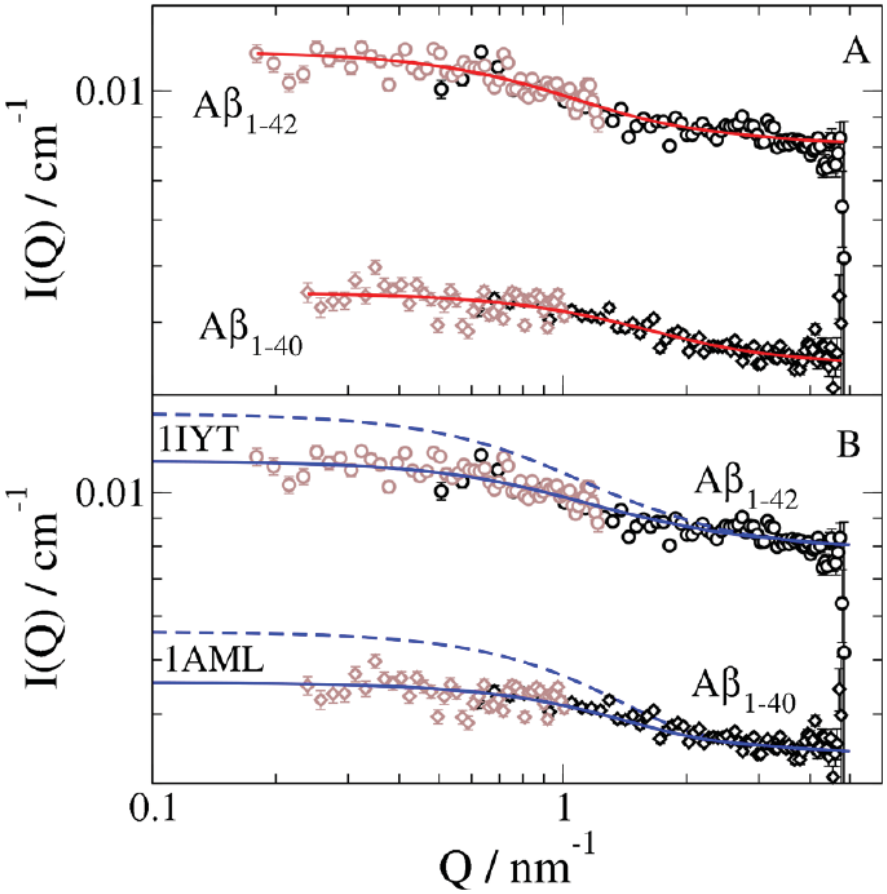

Fig 2. Scattering intensity of Aβ monomers in dHFIP ($Aß_{1-42}$, concentration 5.6 mg/ml, $Aß_{1-40}$ concentration 2.4 mg/ml) after three weeks incubation measured at detector distance of 5.6 m (grey) and 1.1 m (black). (A) The red solid line shows the fitted Beaucage function with fixed dimensionality ***d* = 2**. (B) SANS data compared to simulations based on atomic coordinates from 3D NMR structure data ($Aß_{1-42}$ PDB code 1IYT, $Aβ_{1-40}$ compared to PDB code 1AML). Broken blue lines represent the average over the PDB structures; while solid blue lines include a surface layer with increased solvent density.

doi:10.1371/journal.pone.0150267.g002

layer in water seems to be mainly determined by geometric effects of the surface and partly by the electrostatic field at the protein surface and water structure perturbation as shown by MD simulations by Merzel and Smith[57]. At least a similar geometric effect of the protein surface might be present here. MD simulations can only answer how far electrostatic effects or the stronger hydrogen bonds of HFIP compared to water contribute. The mean R_g of $Aβ_{1-42}$ monomer from these conformations is 1.58 nm and 1.46 nm including the surface layer (see S3 Fig). For $Aβ_{1-40}$ the mean R_g is 1.29 nm and 1.16 nm including the surface layer. Thus a surface layer with increased density decreases R_g as a result of the combination of solvent scattering length density and protein scattering length density. The strong effect of the surface layer is related to the large volume of the surface layer, which is in average a factor of 2.6 (1AML) and 2.3 (1IYT) larger than the protein volume. For a detailed determination of a changed density in

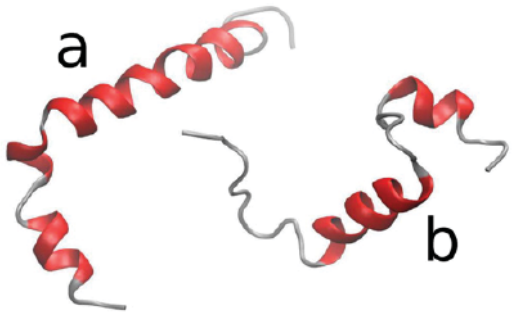

Fig 3. Exemplary structure of Aβ monomers: (a) $A\beta_{1-42}$ $dHFIP_{0.8}D_2O_{0.2}$ (PDB code 1IYT)[20] with two α helices from residues Ser8-Gly25 and Lys28-Gly38, which is connected by a type I β-turn. (b) $A\beta_{1-40}$ in $TFE_{0.4}H_2O_{0.6}$ (PDB code 1AML)[21] with two α helices from Gln15-Asp23 and from Ile31-Met35 connected with a type I β-turn.

doi:10.1371/journal.pone.0150267.g003

the surface layer a combination of SAXS and SANS with different contrast contributions is required. SAXS measurements were not possible in dHFIP as the solvent evaporated due to the high-energy input on a high intensity beam line. Nevertheless the observed radius of gyration seems to be influenced by a solvent surface layer and shows compatibility of the observed radius of gyration with previously reported structures of Aβ in similar solvents. It should be noted that the actual configuration and flexibility has a strong influence on the scattering as SANS measures the configurational ensemble. Comparing the simulated scattering of the different configurations according to the PDB structures (see S3 Fig) we observe that the $A\beta_{1-42}$ scattering patterns stay quite similar as the small hinge between the two α-helices allows only small changes of the configuration. $A\beta_{1-40}$ has larger configurational freedom (more disordered regions and stronger variation in the PDB structures) and consequently larger differences in the scattering patterns and R_g. Generally a larger configurational freedom may allow more extended configuration. Nevertheless, the NMR structures and the SANS data show a similar tendency with a more compact $A\beta_{1-40}$ compared to $A\beta_{1-42}$. The larger configurational freedom results here in a more compact structure, which may be a result of a reduced contact to the solvent.

The question arises how to compare the radius of gyration and the hydrodynamic radius as both are influenced by a solvent surface layer, but in different ways. A simple approach for globular proteins relates the radius R_S of a sphere to the radius of gyration by $R_g^2 = (3/5)R_s^2$ resulting in R_s of 2.06 nm for $A\beta_{1-42}$ and 1.3 nm for $A\beta_{1-40}$. If we assume that the monomer is surrounded by a solvent layer contributing to the apparent hydrodynamic radius ($2R_{s,HFIP} = 0.68\ nm$) the hydrodynamic radius of $A\beta_{1-42}$ and $A\beta_{1-40}$ monomer is about 2.7 nm and 2.0 nm respectively, which correspond approximately to the measured R_H from DLS experiment. In a different approach based on measurements of R_g and R_H for proteins between 50–400 residues in denaturing solvents the relation $R_g/R_H = 1.06$ is found[58]. Even taking into account that Aβ is smaller than the reference proteins and the difference in solvent molecule size, too small hydrodynamic radii result demonstrating that a Aβ seems to be not in a disordered state.

The hydrodynamic radii of $A\beta_{1-42}$ and $A\beta_{1-40}$ in water is according to Nag et al. 0.9 nm[43]. For both monomers the actual conformation in water is not known and the influence of a hydration layer is undetermined. Assuming a hydration layer of 0.3 nm as found for other proteins the configuration seems to be rather compact. Nevertheless it is clear that not only the predominantly α-helical structure in dHFIP can increase the hydrodynamic radius as observed.

The strong hydrogen bonding properties of dHFIP may be of importance here. Stronger hydrogen bonding compared to the peptide in water may cause a larger peptide-solvent complex that contributes to the hydrodynamic radius. For the smaller $A\beta_{1-40}$ the more compact structure reduces the surface to the solvent and a lower number of solvent molecules may contribute to the complex resulting in the smaller hydrodynamic radius compared to $A\beta_{1-42}$. The strong hydrogen bonding of dHFIP allows solvation of monomeric peptides without aggregation for Aβ and seems to increase the apparent hydrodynamic radius.

Conclusions

In this study we investigated the applicability of SANS to the study of the Alzheimer's disease associated amyloid beta peptide (Aβ). Several properties of this 4 to 5 kDa small peptide make structural studies with high-resolution methods of the monomer as well as of the early assembly states extremely difficult. Therefore, other methods giving less detailed structural information become more important. Small angle neutron scattering and dynamic light scattering at relatively high concentration (for Aβ aggregation experiments) was used to probe the application of SANS as a scattering method without radiation damage for Aβ solutions as a prerequisite for further kinetic measurements of Aβ aggregation and fibril formation. We found that the solvation of Aβ in dHFIP is a fast process, where after a short incubation of less than 1 h the remaining aggregates mainly sediment. Therefore preparation time can be shortened by centrifugation to sediment the small amount of aggregates. We showed that SANS is able to perform measurements with monomeric Aβ solutions to determine the radius of gyration. Although we cannot differentiate between conformations as in high-resolution techniques, we find a more compact structure of $A\beta_{1-40}$ compared to $A\beta_{1-42}$ showing that low resolution information can give valuable insight about the general structure. The difference in structure between $A\beta_{1-40}$ and $A\beta_{1-42}$ regarding the distribution of α-helices and disordered regions seems to be preserved in pure dHFIP. Additionally the results show the probable existence of a surface layer with increased density of dHFIP solvent similar to the hydration layer of proteins in water, which was not observed by other methods. The solvent surface layer increases the hydrodynamic radius considerably. Still the application of SANS onto low concentration samples of a protein as small as Aβ would benefit from higher intensity and it is at the limit of the nowadays possibilities.

Supporting Information

S1 Dataset. DLS and SANS data.
(ZIP)

S1 Fig. Time resolved DLS experiment with a concentration of 2.4 mg/ml $A\beta_{1-40}$ in dHFIP. The sample was measured between 0.5 h and 12 days after initial incubation at 20°C. The strong change in the absolute value of the correlation function at $\tau \rightarrow 0$ (intercept) is due to the increase in signal to noise ratio. With more large aggregates, respectively higher intensity, the signal has less noise and the intercept is closer to one. Additionally the signal to noise ratio depends on the laser attenuation chosen automatically by the instrument adjusting the mean intensity to values between 200000 and 500000 counts/s dependent on the total scattered intensity of a sample.
(EPS)

S2 Fig. DLS of 5.6 mg/ml $A\beta_{1-42}$ in HFIP. The sample was measured between 0.5 h and 14 days after initial incubation at 20°C in HFIP. See S1 Fig for more comments.
(EPS)

S3 Fig. Simulated scattering intensities for configurations according to PDB structures of $A\beta_{1-42}$ and $A\beta_{1-40}$. Black and green lines take only the contrast to the dHFIP solvent into account, while for red and blue lines additionally a solvent surface layer with 0.3 nm thickness and 5% higher density compared to bulk dHFIP is used. The given radius of gyration R_g is the average of the different structures in the PDB file as evaluated from the scattering in the Guinier region. The differences in the forward scattering for the same protein arise due to the changed protein volume if the configuration is changed.
(EPS)

Author Contributions

Conceived and designed the experiments: BZ RB LN. Performed the experiments: BZ AR. Analyzed the data: BZ RB LN AR. Wrote the paper: BZ RB LN AR DR DW.

References

1. Blennow K, de Leon MJ, Zetterberg H. Alzheimer's disease. Lancet. 2006; 368: 387–403. doi: 10.1016/S0140-6736(06)69113-7 PMID: 16876668
2. Dauer W, Przedborski S. Parkinson's Disease. Neuron. 2003; 39: 889–909. doi: 10.1016/S0896-6273(03)00568-3 PMID: 12971891
3. Roos RAC. Huntington's disease: a clinical review. Orphanet J Rare Dis. BioMed Central Ltd; 2010; 5: 40. doi: 10.1186/1750-1172-5-40 PMID: 21171977
4. Ross CA, Poirier MA. Protein aggregation and neurodegenerative disease. Nat Med. 2004; 10 Suppl: S10–7. doi: 10.1038/nm1066 PMID: 15272267
5. Murphy RM. Peptide aggregation in neurodegenerative disease. Annu Rev Biomed Eng. 2002; 4: 155–74. doi: 10.1146/annurev.bioeng.4.092801.094202 PMID: 12117755
6. Hamley IW. The amyloid beta peptide: a chemist's perspective. Role in Alzheimer's and fibrillization. Chem Rev. American Chemical Society; 2012; 112: 5147–92. doi: 10.1021/cr3000994 PMID: 22813427
7. Sommer B. Alzheimer's disease and the amyloid cascade hypothesis: Ten years on. Curr Opin Pharmacol. 2002; 2: 87–92. doi: 10.1016/S1471-4892(01)00126-6 PMID: 11786314
8. Wang HW, Pasternak JF, Kuo H, Ristic H, Lambert MP, Chromy B, et al. Soluble oligomers of β amyloid (1–42) inhibit long-term potentiation but not long-term depression in rat dentate gyrus. Brain Res. 2002; 924: 133–140. doi: 10.1016/S0006-8993(01)03058-X PMID: 11750898
9. Walsh DM, Klyubin I, Fadeeva J V, Rowan MJ, Selkoe DJ. Amyloid-beta oligomers: their production, toxicity and therapeutic inhibition. Biochem Soc Trans. 2002; 30: 552–557. doi: 10.1042/BST0300552 PMID: 12196135
10. Larson ME, Lesné SE. Soluble Aβ oligomer production and toxicity. J Neurochem. 2012; 120 (Suppl: 125–139. doi: 10.1111/j.1471-4159.2011.07478.x.Soluble
11. Selkoe DJ. Normal and abnormal biology of the beta-amyloid precursor protein. Annu Rev Neurosci. 1994; 17: 489–517. doi: 10.1146/annurev.ne.17.030194.002421 PMID: 8210185
12. Jarrett JT, Berger EP, Lansbury PT. The C-terminus of the β protein is critical in amyloidogenesis. Ann N Y Acad Sci. 1993; 695: 144–148. doi: 10.1111/j.1749-6632.1993.tb23043.x PMID: 8239273
13. Soto C, Brahes MC, Alvarez J, Inestrosa NC. Structural Determinants of the Alzheimer ' s. J Neurochem. 1994; 63: 1191–1198. PMID: 7931272
14. Kirschner DA, Inouye H, Duffy LK, Sinclair A, Lind M, Selkoe DJ. Synthetic peptide homologous to beta protein from Alzheimer disease forms amyloid-like fibrils in vitro. Proc Natl Acad Sci U S A. 1987; 84: 6953–6957. doi: 10.1073/pnas.84.19.6953 PMID: 3477820
15. Sticht H, Bayer P, Willbold D, Dames S, Hilbich C, Beyreuther K, et al. Structure of amyloid A4-(1–40)-peptide of Alzheimer's disease. Eur J Biochem. 1995; 233: 293–298. doi: 10.1111/j.1432-1033.1995.293_1.x PMID: 7588758
16. Ahmed M, Davis J, Aucoin D, Sato T, Ahuja S, Aimoto S, et al. Structural conversion of neurotoxic amyloid-beta(1–42) oligomers to fibrils. Nat Struct Mol Biol. Nature Publishing Group; 2010; 17: 561–567. doi: 10.1038/nsmb.1799 PMID: 20383142

17. Janek K, Rothemund S, Gast K, Beyermann M, Zipper J, Fabian H, et al. Study of the conformational transition of Ab(1–42) using D-amino acid replacement analogues. Biochemistry. 2001; 40: 5457–5463. PMID: 11331010

18. Wolff M, Unuchek D, Zhang B, Gordeliy V, Willbold D, Nagel-Steger L. Amyloid β Oligomeric Species Present in the Lag Phase of Amyloid Formation. PLOS ONE. Public Library of Science; 2015; 10: e0127865. doi: 10.1371/journal.pone.0127865 PMID: 26024352

19. Vivekanandan S, Brender JR, Lee SY, Ramamoorthy A. A partially folded structure of amyloid-beta(1–40) in an aqueous environment. Biochem Biophys Res Commun. Elsevier Inc.; 2011; 411: 312–6. doi: 10.1016/j.bbrc.2011.06.133 PMID: 21726530

20. Crescenzi O, Tomaselli S, Guerrini R, Salvadori S, D'Ursi AM, Temussi PA, et al. Solution structure of the Alzheimer amyloid β-peptide (1–42) in an apolar microenvironment. Eur J Biochem. 2002; 269: 5642–5648. doi: 10.1046/j.1432-1033.2002.03271.x PMID: 12423364

21. Sticht H, Bayer P, Willbold D, Dames S, Hilbich C, Beyreuther K, et al. Structure of Amyloid A4-(1–40)-Peptide of Alzheimer's Disease. Eur J Biochem. 1995; 233: 293–298. doi: 10.1111/j.1432-1033.1995.293_1.x PMID: 7588758

22. Fezoui Y, Teplow DB. Kinetic studies of amyloid beta-protein fibril assembly. Differential effects of alpha-helix stabilization. J Biol Chem. 2002; 277: 36948–36954. doi: 10.1074/jbc.M204168200 PMID: 12149256

23. Tomaselli S, Esposito V, Vangone P, van Nuland NAJ, Bonvin AMJJ, Guerrini R, et al. The alpha-to-beta conformational transition of Alzheimer's Abeta-(1–42) peptide in aqueous media is reversible: a step by step conformational analysis suggests the location of beta conformation seeding. Chembiochem. 2006; 7: 257–67. doi: 10.1002/cbic.200500223 PMID: 16444756

24. van der Linden E, Venema P. Self-assembly and aggregation of proteins. Curr Opin Colloid Interface Sci. 2007; 12: 158–165. doi: 10.1016/j.cocis.2007.07.010

25. Fezoui Y, Hartley DM, Harper JD, Khurana R, Walsh DM, Condron MM, et al. An improved method of preparing the amyloid beta-protein for fibrillogenesis and neurotoxicity experiments. Amyloid Int J Exp Clin Investig. Taylor & Francis; 2000; 7: 166–178.

26. Ward RV, Jennings KH, Jepras R, Neville W, Owen DE, Hawkins J, et al. Fractionation and characterization of oligomeric, protofibrillar and fibrillar forms of β-amyloid peptide. Biochem J. Portland Press Limited; 2000; 348: 137–144. doi: 10.1042/bj3480137 PMID: 10794724

27. Sigurdsson EM. Amyloid Proteins: Methods And Protocols. Springer Science & Business Media; 2005.

28. Zagorski MG, Yang J, Shao H, Ma K, Zeng H, Hong A. Amyloid, Prions, and Other Protein Aggregates. Methods in Enzymology. Elsevier; 1999. doi: 10.1016/S0076-6879(99)09015-1

29. Broersen K, Jonckheere W, Rozenski J, Vandersteen A, Pauwels K, Pastore A, et al. A standardized and biocompatible preparation of aggregate-free amyloid beta peptide for biophysical and biological studies of Alzheimer's disease. Protein Eng Des Sel. 2011; 24: 743–50. doi: 10.1093/protein/gzr020 PMID: 21565831

30. Nichols MR, Moss MA, Reed DK, Cratic-McDaniel S, Hoh JH, Rosenberry TL. Amyloid-beta protofibrils differ from amyloid-beta aggregates induced in dilute hexafluoroisopropanol in stability and morphology. J Biol Chem. 2005; 280: 2471–80. doi: 10.1074/jbc.M410553200 PMID: 15528204

31. Stadler AM, Stingaciu L, Radulescu A, Holderer O, Monkenbusch M, Biehl R, et al. Internal nanosecond dynamics in the intrinsically disordered myelin basic protein. J Am Chem Soc. 2014; 136: 6987–94. doi: 10.1021/ja502343b PMID: 24758710

32. Koch MH, Vachette P, Svergun DI. Small-angle scattering: a view on the properties, structures and structural changes of biological macromolecules in solution. Q Rev Biophys. 2003; 36: 147–227. PMID: 14686102

33. Jacrot B. The study of biological structures by neutron scattering from solution. Reports Prog Phys. 1976; 39: 911–953.

34. Ibel K, Stuhrmann HB. Comparison of neutron and X-ray scattering of dilute myoglobin solutions. J Mol Biol. 1975; 93: 255–265. doi: 10.1016/0022-2836(75)90131-X PMID: 1171250

35. Lipfert J, Doniach S. Small-angle X-ray scattering from RNA, proteins, and protein complexes. Annu Rev Biophys Biomol Struct. 2007; 36: 307–27. doi: 10.1146/annurev.biophys.36.040306.132655 PMID: 17284163

36. Biehl R, Richter D. Slow internal protein dynamics in solution. J Phys Condens Matter. IOP Publishing; 2014; 26: 503103. doi: 10.1088/0953-8984/26/50/503103 PMID: 25419898

37. Gabel F, Bicout D, Lehnert U, Tehei M, Weik M, Zaccai G. Protein dynamics studied by neutron scattering. Q Rev Biophys. 2002; 35: 327–367. doi: 10.1017/S0033583502003840 PMID: 12621860

38. Pedersen J, Hansen S, Bauer R. The aggregation behavior of zinc-free insulin studied by small-angle neutron scattering. Eur Biophys J. 1994; 22. doi: 10.1007/BF00180159

39. Jeng U-S, Lin T-L, Lin JM, Ho DL. Contrast variation SANS for the solution structure of the β-amyloid peptide 1–40 influenced by SDS surfactants. Phys B Condens Matter. 2006; 385–386: 865–867. doi: 10.1016/j.physb.2006.05.128

40. Yong W, Lomakin A, Kirkitadze MD, Teplow DB, Chen S-H, Benedek GB. Structure determination of micelle-like intermediates in amyloid β^2-protein fibril assembly by using small angle neutron scattering. Proc Natl Acad Sci. 2002; 99: 150–154. doi: 10.1073/pnas.012584899 PMID: 11756677

41. Stanley C, Perevozchikova T, Berthelier V. Structural Formation of Huntingtin Exon 1 Aggregates Probed by Small-Angle Neutron Scattering. Biophys J. Cell Press; 2011. pp. 2504–2512.

42. Bolisetty S, Adamcik J, Mezzenga R. Snapshots of fibrillation and aggregation kinetics in multistranded amyloid β-lactoglobulin fibrils. Soft Matter. Royal Society of Chemistry; 2011; 7: 493–499. doi: 10.1039/C0SM00502A

43. Nag S, Sarkar B, Bandyopadhyay A, Sahoo B, Sreenivasan VKA, Kombrabail M, et al. Nature of the amyloid-beta monomer and the monomer-oligomer equilibrium. J Biol Chem. 2011; 286: 13827–33. doi: 10.1074/jbc.M110.199885 PMID: 21349839

44. Sakono M, Zako T. Amyloid oligomers: formation and toxicity of Abeta oligomers. FEBS J. 2010; 277: 1348–58. doi: 10.1111/j.1742-4658.2010.07568.x PMID: 20148964

45. Pace CN, Vajdos F, Fee L, Grimsley G, Gray T. How to measure and predict the molar absorption coefficient of a protein. Protein Sci. Cold Spring Harbor Laboratory Press; 1995; 4: 2411–2423. PMID: 8563639

46. Radulescu A, Pipich V, Frielinghaus H, Appavou M- S. KWS-2, the high intensity/wide Q-range small-angle neutron diffractometer for soft-matter and biology at FRM II. J Phys Conf Ser. 2012; 351: 012026. doi: 10.1088/1742-6596/351/1/012026

47. Svergun DI, Richard S, Koch MHJ, Sayers Z, Kuprin S, Zaccai G. Protein Hydration in Solution: Experimental Observation by X-Ray and Neutron Scattering. Proc Natl Acad Sci USA. 1998; 95: 2267–2272. doi: 10.1073/pnas.95.5.2267 PMID: 9482874

48. Beaucage G. Approximations Leading to a Unified Exponential/Power-Law Approach to Small-Angle Scattering. J Appl Crystallogr. International Union of Crystallography; 1995; 28: 717–728. doi: 10.1107/S0021889895005292

49. Beaucage G. Small-Angle Scattering from Polymeric Mass Fractals of Arbitrary Mass-Fractal Dimension. J Appl Crystallogr. 1996; 29: 134–146. doi: 10.1107/S0021889895011605

50. Hammouda B. Analysis of the Beaucage model. J Appl Crystallogr. 2010; 43: 1474–1478. doi: 10.1107/S0021889810033856

51. Hinsen K. The molecular modeling toolkit: A new approach to molecular simulations. J Comput Chem. 2000; 21: 79–85. doi: 10.1002/(SICI)1096-987X(20000130)21:2<79::AID-JCC1>3.0.CO;2-B

52. Eisenhaber F, Lijnzaad P, Argos P, Sander C, Scharf M. The double cubic lattice method: Efficient approaches to numerical integration of surface area and volume and to dot surface contouring of molecular assemblies. J Comput Chem. 1995; 16: 273–284. doi: 10.1002/jcc.540160303

53. Lashuel HA, Hartley DM, Balakhaneh D, Aggarwal A, Teichberg S, Callaway DJE. New class of inhibitors of amyloid-beta fibril formation. Implications for the mechanism of pathogenesis in Alzheimer's disease. J Biol Chem. 2002; 277: 42881–90. doi: 10.1074/jbc.M206593200 PMID: 12167652

54. Morrison ID, Grabowski EF, Herb CA. Improved techniques for particle size determination by quasi-elastic light scattering. Langmuir. 1985; 1: 496–501. doi: 10.1021/la00064a016

55. Calvetti D, Reichel L, Shuibi A. L-curve and curvature bounds for Tikhonov regularization. Numer Algorithms. 2004; 301–314.

56. Rubinson K a., Stanley C, Krueger S. Small-angle neutron scattering and the errors in protein structures that arise from uncorrected background and intermolecular interactions. J Appl Crystallogr. International Union of Crystallography; 2008; 41: 456–465. doi: 10.1107/S0021889808004950

57. Merzel F, Smith JC. Is the first hydration shell of lysozyme of higher density than bulk water? Proc Natl Acad Sci U S A. 2002; 99: 5378–83. doi: 10.1073/pnas.082335099 PMID: 11959992

58. Wilkins DK, Grimshaw SB, Receveur V, Dobson CM, Jones JA, Smith LJ. Hydrodynamic radii of native and denatured proteins measured by pulse field gradient NMR techniques. Biochemistry. 1999; 38: 16424–31. PMID: 10600103

2.2 Amyloid β Oligomeric Species Present in the Lag Phase of Amyloid Formation

Martin Wolff[1,2], Dmitry Unuchek[3], Bo Zhang[2,4], Valentin Gordeliy[2,3,5,6,7], Dieter Willbold[1,2], Luitgard Nagel-Steger[1,2*]

Status: published in PLOS ONE

Impact Factor: 3.23

Proportion of contribution: 15%

Contributions: Conceived and designed the experiments

PLOS | ONE

RESEARCH ARTICLE

Amyloid β Oligomeric Species Present in the Lag Phase of Amyloid Formation

Martin Wolff[1,2], Dmitry Unuchek[3], Bo Zhang[2,4], Valentin Gordeliy[2,3,5,6,7], Dieter Willbold[1,2], Luitgard Nagel-Steger[1,2]*

1 Institut für Physikalische Biologie, Heinrich-Heine-University Düsseldorf, Düsseldorf, Germany, **2** Institute of Complex Systems, Structural Biochemistry (ICS-6), Research Centre Jülich, Jülich, Germany, **3** Dep. of Molecular and Chemical Physics, Moscow Institute of Physics and Technology, Dolgoprudniy, Russian Federation, **4** Institute of Complex Systems, Neutron Scattering (ICS-1), Research Centre Jülich, Jülich, Germany, **5** Institut de Biologie Structurale J.-P. Ebel, Université Grenoble Alpes, Grenoble, France, **6** Institut de Biologie Structurale J.-P. Ebel, Centre National de la Recherche Scientifique, Grenoble, France, **7** Institut de Biologie Structurale J.-P. Ebel, Direction des Sciences du Vivant, Commissariat à l'Énergie Atomique, Grenoble, France

* l.nagel-steger@fz-juelich

Citation: Wolff M, Unuchek D, Zhang B, Gordeliy V, Willbold D, Nagel-Steger L (2015) Amyloid β Oligomeric Species Present in the Lag Phase of Amyloid Formation. PLoS ONE 10(5): e0127865. doi:10.1371/journal.pone.0127865

Academic Editor: Aldrin V. Gomes, University of California, Davis, UNITED STATES

Received: January 26, 2015

Accepted: April 20, 2015

Published: May 29, 2015

Data Availability Statement: All relevant data are within the paper.

Funding: Computing time and computational support for UltraScan III software was provided by the Texas Advanced Computing Centre from UT Austin, and is supported by an NSF Teragrid Allocation grant, TGMCB070038. Helmholtz Association funded this work through the Helmholtz-Portfolio Topics "Technology and Medicine" and "Drug Research". The funders had no role in study design, data collection and analysis, decision to publish, or preparation of the manuscript.

Abstract

Alzheimer's disease (AD)-associated amyloid β peptide (Aβ) is one of the main actors in AD pathogenesis. Aβ is characterized by its high tendency to self-associate, leading to the generation of oligomers and amyloid fibrils. The elucidation of pathways and intermediates is crucial for the understanding of protein assembly mechanisms in general and in conjunction with neurodegenerative diseases, e.g., for the identification of new therapeutic targets. Our study focused on Aβ42 and its oligomeric assemblies in the lag phase of amyloid formation, as studied by sedimentation velocity (SV) centrifugation. The assembly state of Aβ during the lag phase, the time required by an Aβ solution to reach the exponential growth phase of aggregation, was characterized by a dominant monomer fraction below 1 S and a population of oligomeric species between 4 and 16 S. From the oligomer population, two major species close to a 12-mer and an 18-mer with a globular shape were identified. The recurrence of these two species at different initial concentrations and experimental conditions as the smallest assemblies present in solution supports the existence of distinct, energetically favored assemblies in solution. The sizes of the two species suggest an Aβ42 aggregation pathway that is based on a basic hexameric building block. The study demonstrates the potential of SV analysis for the evaluation of protein aggregation pathways.

Introduction

Alzheimer's disease (AD) is an age-related disease with growing incidence in populations with high life expectancies. As a consequence AD poses a major health risk to people and a substantial worldwide economic burden [1]. Therefore, efforts to improve our understanding of the disease mechanism have been taken to develop knowledge-based therapeutic concepts.

Competing Interests: The authors have declared that no competing interests exist.

It is well established that a proteolytic fragment of the amyloid precursor protein (APP) plays a key role in disease pathogenesis, as reviewed in [2,3]. This 39 to 43 residue fragment of the membrane spanning APP, referred to as the amyloid β peptide (Aβ), is highly prone to self-association [4]. Although the monomeric form of Aβ is apparently nontoxic, the self-associated species exhibit neurotoxic behavior [5]. Fibrillar deposits of Aβ in intercellular plaques are a histological marker for post-mortem AD diagnosis and are considered to be the cause of neurodegeneration. More recently, however, it was found that soluble Aβ oligomers are more neurotoxic than the amyloid fibrils and thus may represent the causative agents for neurodegeneration [6–13]. Nevertheless, a conclusive, generally accepted definition of the toxic oligomer is still missing [14]. As pointed out in [15] there are manifold challenges for oligomer study, one of which is the rather low concentrations of the natural oligomeric species in tissues and body fluids of AD patients, which hinder a direct preparation and characterization. Additionally, it is difficult to control Aβ aggregation processes *in vitro*. Therefore structural information that should aid the development of therapeutic interventions is still missing.

Because there is obviously still need for clarification we engaged in this study in a thorough characterization of Aβ aggregation by sedimentation velocity centrifugation (SV), one of the major applications of analytical ultracentrifugation. SV analysis exhibits several advantageous properties, making it especially attractive for the investigation of self-assembling proteins. SV is a first-principles based method. No calibration standards are required as for instance necessary in size exclusion chromatography to assign molecular weights to elution volumes. And even more important the characterization is carried out in solution without a solid phase being involved. In SV analysis all parameters regarding size distribution and shape of aggregates are derived simultaneously from one specific Aβ solution. Although fractionation occurs due to the sedimentation process, leading to improved detectability of the different species, aggregates sediment always in the presence of equilibrium concentrations of smaller species and monomers, preventing dissociation. Sedimentation velocity centrifugation (SV) is suitable for the study of macromolecules ranging from a few thousand Da to several MDa. Measurement of peptide concentrations by absorbance throughout the experiment guarantees control over possible losses of Aβ. In recent years, SV methodology has drastically improved in terms of information content and resolution [16,17]. This is particularly pertinent in the field of aggregating proteins where analytical ultracentrifugation has become an increasingly important technique due to its unique properties [18–25]. In the case of self-assembling proteins, the samples consist of mixtures of differently sized and shaped particles. In SV experiments the solute concentration as a function of the radial position within the rotor is recorded at regular time intervals. These concentration profiles can be fitted by a sum of solutions of the Lamm equation [26]. The $c(s)$ distribution [27] and genetic algorithm based analyses [28] are two implemented software approaches to perform this data fitting task. In previously reported SV experiments, we have demonstrated the power of the data evaluation method for the determination of size- and shape-distributions of the Aβ peptide [29,30].

In our study we decided to investigate the early phase of Aβ42 self-assembly. We chose Aβ42 because the elevation of its levels and of the ratio of Aβ42 to the shorter major form Aβ40, had been identified as important early events in the pathogenesis of AD[31]. Specific questions to be addressed are: what is the size of the smallest detectable oligomer in solution, and do well-defined, oligomeric species exist as the hypothesis of a toxic oligomer might suggest. For this purpose we restricted our analysis to the lag phase of aggregation as defined by thioflavin T kinetic measurements.

Materials and Methods

Amyloid β preparation

Synthetic human Aβ42 peptide was purchased as a trifluoroacetate salt (Bachem, Weil am Rhein, Germany). For disintegration of preexisting aggregates, the peptide was predissolved in 100% hexafluoroisopropanol (HFIP) at 1 mg/mL and incubated overnight at room temperature. The solution was then divided into aliquots, lyophilized and stored at -8000B0030C until required. Aβ42 was dissolved at pH 10 for analysis of a monomeric sample. To initiate aggregation the Aβ42 peptide was dissolved at concentrations from 10 to 240 μM in 10 mM NaP_i buffer (6.2 mM sodium dihydrogen phosphate, 3.8 mM disodium hydrogen phosphate, pH 7.4).

Thioflavin T (ThT)-Assay

For the quantitative assessment of amyloid formation, freshly prepared Aβ42 samples in NaP_i buffer with 5 μM ThT were incubated in a black 96-well fluorescence plate with an optical bottom (Nunc, Thermo Scientific, Germany). ThT fluorescence was recorded every 30 min in a plate reader (M1000, Tecan, Maennedorf, Switzerland) at λ_{ex} = 446 nm and λ_{em} = 490 nm with a bandwidth of 5 nm. The temperature was controlled at either 20 or 37°C.

CD spectroscopy

Circular dichroism spectroscopic measurements were carried out on a Jasco J-815 spectrometer. A 1 mm optical path length cuvette was used. The temperature was controlled at 20°C. For the measurement over time, sample incubation was not performed in the cuvette but in a standard sample tube, from which aliquots were taken. Spectra were recorded from λ = 260 nm to 185 nm at 1 nm resolution, 50 nm/min scan speed, and an integration time of 0.5 s. For signal improvement ten accumulations were averaged. The obtained spectra were transformed from ellipticity θ, measured in millidegrees (mdeg), to mean residue ellipticity (MRE) after subtraction of the buffer spectra.

Analytical Ultracentrifugation

Sedimentation velocity centrifugation experiments were carried out in a Beckman Optima XL-A (Beckman-Coulter, Brea, CA, USA), equipped with absorption optics and a four-hole rotor. Samples (volume 400 μL) were filled into standard aluminum or epon double sector cells with quartz glass windows. Measurements were performed in the intensity mode [32] at detection wavelengths between 224 and 242 nm in order to adjust for different peptide concentrations. For Aβ42 peptide concentrations above 40 μM the temperature was set to 10°C, otherwise 20°C was chosen. Radial scans were recorded with 20 μm radial resolution at ~1.5 min intervals. The software packages UltraScan II v 9.9/III v 2.0 [28,33] and SEDFIT v 14.1[34] were used for data evaluation. After transformation of the recorded sedimentation velocity data, taken in the intensity mode, to either absorbance or pseudo-absorbance data in the respective data evaluation software, time- as well as radially-invariant noise were calculated and subtracted. In UltraScan a model-independent analysis approach for fitting SV data, which permits simultaneous determination of shape and molecular weight distributions for mono- and polydisperse solutions of macromolecules, was further refined by a parsimoniously regularized fit of independent solutions of the Lamm equation applying a genetic algorithm (GA) to ensure convergence into the global minimum [35]. The final results were subjected to a Monte Carlo (MC) analysis with 50 iterations each. In SEDFIT, continuous sedimentation coefficient distributions $c(s)$ were determined with 0.05 S resolution and an F-ratio = 0.95. Suitable s-value ranges between 0 and 30 S and for GA f/f_0 between 1 and 4 were chosen. Buffer density

Table 1. Solvent parameters for 10 mM NaPi, pH 7.4 and $\bar{\nu}$ of Aβ42 for the temperatures used in the SV experiments. Calculations were performed with SEDNTERP or UltraScan II/III.

temperature (°C)	$\bar{\nu}$ (cm^3/g)	density (g/cm^3)	viscosity (cp)
10	0.734	1.0011	1.3109
20	0.738	0.9996	1.0048

doi:10.1371/journal.pone.0127865.t001

and viscosity (Table 1) had been calculated with SEDNTERP v 20111201 beta [36,37]. The partial specific volume of Aβ42 was calculated according to the method of Cohn and Edsall [38,39] as implemented in SEDNTERP or UltraScan II/III (Table 1). Graphical output for SEDFIT results was created with the software GUSSI vs 1.0.3, written by Chad A. Brautigam, University of Texas Southwestern Medical Center. All reported *s*-values were corrected for 20°C and water and therefore $s_{20,w}$-values.

Results and Discussion

In this study we analyzed freshly prepared solutions of Aβ42 by analytical ultracentrifugation, ThT-assay, and CD spectroscopy to gain insights into the early processes of Aβ42 self-assembly within the lag phase of amyloid formation.

Monomer characterization at pH 10

In a first step, we wanted to characterize the hydrodynamic properties of monomeric Aβ42. At basic pH Aβ42 is stable as a monomer [40]. In contrast to organic solvents like HFIP or TFE [41] known for their monomer stabilizing properties the chosen basic conditions do not induce an α-helical structure. At pH 10 (Fig 1) the Aβ42 peptide shows a secondary structure profile comparable to the one determined at pH 7.4 for the earliest time point as shown in Fig 1. The CD spectrum of the peptide at basic pH did not change within 2 d of incubation, indicating the required stabilization of the peptide. To increase the certainty of species detection, we compared two different software packages for analytical ultracentrifugation data evaluation, i.e., SEDFIT [34] and UltraScan [33].

The SV analysis of 20 μM Aβ42 at pH 10 revealed that the Aβ42 solution consisted of 95% monomers. In Fig 2 the calculated $c(s)$ distribution shows a first peak at 0.6 ± 0.2 S, representing 94% of the sample, and a second broader peak at 4.8 ± 0.5 S, accounting for 6%. The signal increase at *s*-values between 0 and 0.6 S indicated either the presence of smaller species than Aβ42, i.e., fragments that we could neither identify in gel electrophoresis nor mass spectrometry or, more likely, a baseline deconvolution problem caused by the small size of the macromolecules, preventing clearance of the meniscus region during centrifugation. The 0.6 S species fits well to monomeric Aβ42, the 4.8 S species indicates an oligomer of 50 to 70 kDa. The weight averaged f/f_0 was fitted as 1.56. According Eq. 1 the 0.6 S species with $f/f_0 = 1.56$ had a molecular weight of 4.4 kDa, which is close to the molecular weight of the monomeric Aβ42 (4.5 kDa). In contrast to the $c(s)$ determined *s*-value distribution (Fig 2) the GA-MC analysis in UltraScan (Fig 3) fitted three species with an *s*-value smaller than 1, which differed significantly with respect to their frictional ratios. The main species with 0.67 S had a smaller f/f_0 value of 1.35 than the main component from the $c(s)$ analysis. Again the resulting molecular weight is close to 4.6 kDa, which confirmed the monomeric nature of the species. Taken together around 6% of the aggregates with an average *s*-value of 5 S were detected independent from the data evaluation procedure. These aggregates might comprise either residually undissolved material or newly formed assemblies.

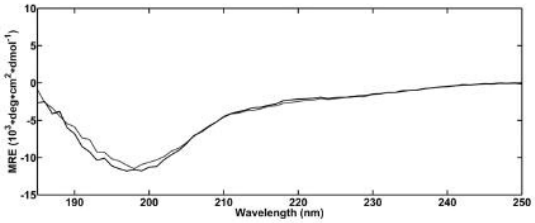

Fig 1. CD-spectroscopy of Aβ42 at pH 10. CD spectra measured at the start of the incubation (black) and after 48 h (grey) at 20°C. Spectra are in agreement with a random coil dominated secondary structure with a characteristic minimum around 200 nm.

doi:10.1371/journal.pone.0127865.g001

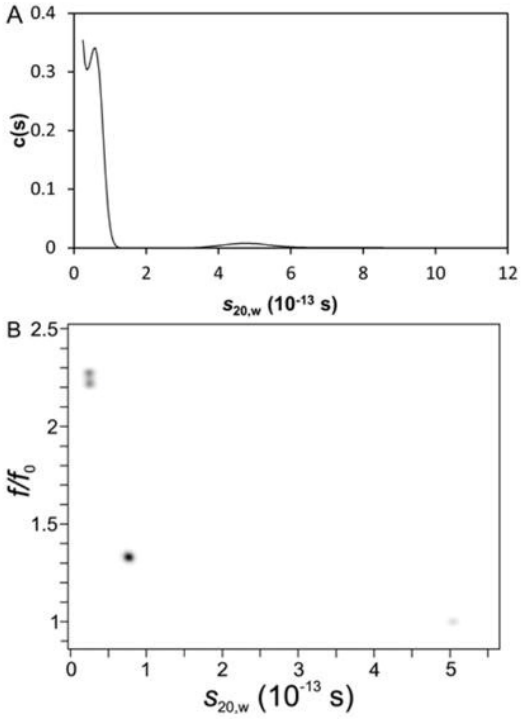

Fig 2. SV-analysis of Aβ42 at pH 10. 40 μM Aβ42 had been centrifuged at 40,000 rpm and 20°C. By *c*(*s*) analysis the most prominent species was detected at s = 0.6 S (A); GA-MC analysis revealed the dominant species at *s* = 0.67S with f/f_0 = 1.35 (B). Results are presented in a pseudo-3D plot with a color coded third dimension indicating the species fraction. In both evaluations a small amount of near spherical aggregates appeared at 5 S. The minor species detected below 1 S are artifacts due to a base line deconvolution problem.

doi:10.1371/journal.pone.0127865.g002

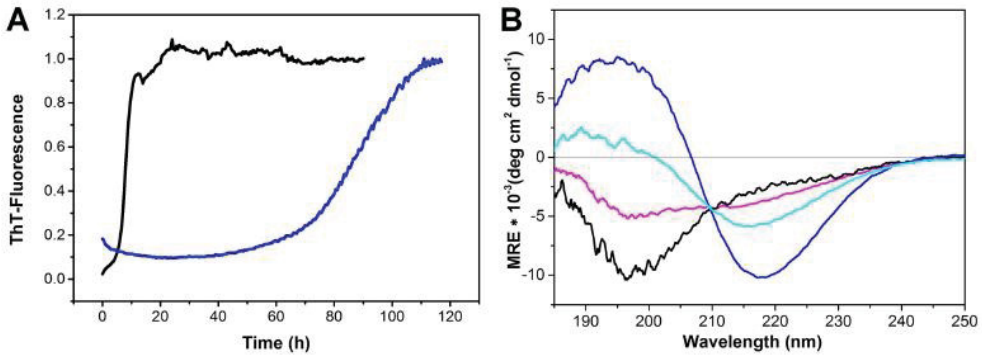

Fig 3. Kinetics of amyloid formation. ThT-fluorescence kinetics of 40 μM Aβ42 in 10 mM NaP_i at 37°C (black) and 20°C (blue). The maximum RFUs had been normalized to 1. Determined lag times were ~8 h at 37°C and ~80 h at 20°C (A). CD spectra of 37 μM Aβ42 incubated at 20°C for 0 (black), 29 (magenta), 49 (cyan) and 74 h (blue). The spectrum of Aβ42 in NaP_i, pH 7.4 changes within the indicated times from a predominantly random coil spectrum to a β-sheet rich spectrum. Superimposed spectra possess an isosbestic point at 209 nm, indicating a two-state transition (B).

doi:10.1371/journal.pone.0127865.g003

The experimentally determined *s*-value of the monomer is in agreement with an *s*-value of 0.55 S reported in the literature [42]. In the PDB a high resolution structure of full-length Aβ42 exists, that was determined by NMR in an HFIP-water mixture (1Z0Q) [43]. The *s*-value calculated for a bead model [44,45] built from this NMR structure of Aβ42, is 0.72 S and the frictional ratio is 1.3. The structure is characterized by 42% helices and several turns giving it a more compact conformation. In comparison we can conclude that the Aβ42 monomer at pH 10 characterized in our experiments had a more elongated shape, i.e., it was less structured than the structure deposited in the PDB. This result is in agreement with the peptide adopting a random-coil dominated structure, when the helix inducing agent HFIP is not present in the sample buffer.

Length of the lag phase

An SV experiment for Aβ42 monomers at 20°C and 60,000 rpm corresponding to 257,000 g takes 6 to 10 h, because of the slow sedimentation of the monomer. If assemblies present in the lag phase are to be characterized, the lag phase has to last longer than the experimental analysis. Entry into the rapid growth phase would also cause profound changes to the sample composition, thereby complicating data analysis. To determine the length of the lag phase, we followed the process of amyloid formation starting from freshly dissolved Aβ42 by a ThT fluorescence assay (Fig 3A). Measurement over time typically results in a sigmoidal curve, that is subdivided into the lag phase during the initial stage, a steep increase in fluorescence during the growth phase, that represents the formation of amyloid fibrils, and finally the plateau region, where fluorescence is constant and then decreases slightly after a period due to precipitation. The duration of the lag phase was about 80 h for 40 μM Aβ42 (Fig 3A) at 20°C. To complement the fluorescence data, the structural conversion from random coil to β-sheet structure, which accompanies self-assembly of monomeric Aβ42 units to fibrils with an amyloid specific cross-β conformation, was monitored by CD spectroscopy. In Fig 3B, CD spectroscopic measurements over time at 20°C for a 37 μM Aβ42 solution indicated a conformational change, characterized by the presence of an isosbestic point, within 49 to 74 h. The isosbestic point at 209 nm suggests a two-state transition between random coil and β-sheet conformation. The duration of the lag phase determined by the CD measurements and the ThT assay were within the same order of magnitude. Shortening of the lag phase with increasing initial Aβ42 concentrations

was compensated by reducing the temperature from 20 to 10°C during SV analysis of samples at concentrations higher than 40 μM. It was therefore possible to perform the SV experiments within the lag phase of the system and before the initiation of the rapid growth phase.

Concentration dependent self-association

Samples were prepared by freshly dissolving HFIP pretreated synthetic Aβ42 at different initial concentrations. At the start of the sedimentation process all samples had a history of ~1 h handling and thermal equilibration time. Calculation of the initial peptide concentration from a first scan at 3000 rpm and the first scan at 55,000 and 60,000 rpm, respectively, revealed a deficit between 20 and 25% for all samples. Material might have been lost to inter-/surfaces, undissolved, and/or sedimented during the acceleration phase. In a first approach, the SV data were evaluated in a model independent manner by the van Holde-Weischet (vHW) method [46]. Fig 4 shows the combined vHW-distribution plots for 40, 80, 160, 200 and 280 μM initial Aβ42 concentrations. Analyzed solutions showed bimodal distributions characterized by a slowly sedimenting, rather homogenous fraction, visible at the near vertical line in the vHW-distribution at small *s*-values, and a clearly separated, faster sedimenting fraction with *s*-values ranging between 4 and 15 S. The Aβ42 species detected at *s*-values below 1 S were assigned to monomeric species based on the monomer characterization at pH 10 (Fig 2). The proportion of oligomeric species was found to increase from ~30% to ~50% without populating oligomeric species larger than 20 S by a sevenfold increase of the initial Aβ42 concentration of 40 μM. Under the applied experimental conditions, that is speed, temperature, and solvent, molecular species up to 200 S would be detectable in SV analysis. As a consequence the weight averaged *s*-

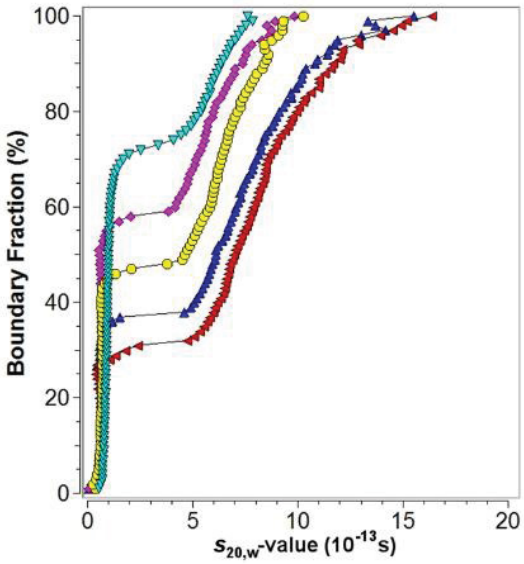

Fig 4. G(s) distributions for different initial concentrations of Aβ42. Model independent analysis of SV data by the van Holde-Weischet method for freshly prepared Aβ42 solutions with 40 μM (cyan triangle), 80 μM (magenta diamond), 160 μM (yellow circle), 200 μM (blue triangle upwards), and 280 μM (red triangle leftwards) initial monomer concentrations.

doi:10.1371/journal.pone.0127865.g004

value of the oligomer fraction increased with increasing Aβ42 concentration. The near horizontal curve progression between *s*-values 1 and 4 S indicates the absence of detectable Aβ42 assemblies in this area and marks therefore the range where kinetically unstable intermediates might be located. Sedimenting species with *s*-values between 1 and 4 S would correspond to oligomers ranging from dimer to octamer assuming a spherical shape, thus giving lower size limits of the intermediates. A further observation was a slight shift of the monomer peak to smaller *s*-values for those measurements performed at 10°C when compared with the data recorded for a 40 μM Aβ42 sample at 20°C. The observed change in *s*-value could be the result of a temperature induced conformational change leading to an altered frictional coefficient of the monomer in solution. Alternatively or additionally the shift might be due to the presence of an unresolved fast equilibrium, e.g. between the monomer and a dimer.

Our major objective was to identify discrete Aβ42 oligomeric species. Such species should feature energetically favored assemblies consisting of a well-defined number of monomeric units. To identify single species, the data were evaluated by calculating $c(s)$ distributions, as well as by applying a parsimoniously regulated genetic algorithm, as implemented in UltraScan. For both approaches the underlying models assume the existence of a number of independent species in solution. For a rapid equilibrium with the smaller compound being present in excess as is the case in our system $c(s)$ is a valid approximation for data evaluation [47]. Provided that seed formation in the lag phase is a slow and rare process, the solution state could be approximated as steady-state equilibrium. This assumption was corroborated by small root mean square deviation (rmsd) values obtained by measuring the agreement between measured and calculated data, which amounted to ~0.5% of the total signal. In Fig 5 the noise subtracted raw data together with the fitted curves of SV runs with three different initial Aβ42 concentrations (A, B and C) and the combination of the resulting $c(s)$ distributions (D) are shown.

As part of the oligomer fraction two prominent species were repeatedly detected by $c(s)$ analysis (Fig 5D) with *s*-values averaged for 9 independent samples of 4.70 S ± 0.27 S and 6.25 S ± 0.28 S (Table 2). These two species were observed under different experimental conditions, i.e., initial Aβ42 concentration, rotor speed and temperature. A third species appeared as a shoulder of the larger species with an *s*-value of 6.2 to 7.6 S. The smaller species at 2.6 S, and any species larger than 10 S were detected at too low concentrations to be reliably assigned. In $c(s)$ a global f/f_0 weight averaged for all *s*-value species was determined. As already noticeable in the vHW-distribution (Fig 4) the percentage of oligomeric species in the range between 1 and 15 S increased with increasing initial Aβ42 concentrations, while concomitantly weight averaged f/f_0 decreased from 1.6 to 1.2 (data not shown). This indicates an increase of globular particles present in solution. To resolve individual shape parameters data evaluation was performed by applying GA in UltraScan. The monomeric species showed a slightly extended conformation with an f/f_0 of 1.6, in agreement with the results from SV analysis at pH 10 (Fig 2). For the oligomers ranging from 4 to 10 S, f/f_0 values < 1.3 were calculated, which is consistent with the results from $c(s)$ showing less extended conformations with increasing fractions of oligomeric species. Although the determined *s*-values for the two species could be reproduced by the GA algorithm (Fig 6), the Monte Carlo statistics for the GA results revealed considerable uncertainties for f/f_0 determinations, probably due to the comparatively low number of scans reporting about the sedimentation and diffusion properties of the larger species. Although no conclusive f/f_0 values for single species could be retrieved, both methods support a globular shape of the oligomers. The obtained shape information had been confirmed by AFM measurements (data not shown). Additionally it is in agreement with reported AFM and TEM studies from literature [48,49].

Calculations of the molecular weights of the oligomers based on the determined *s*-values utilizing shape factors (f/f_0) between 1.0 and 1.1, typical for globular proteins, using the following

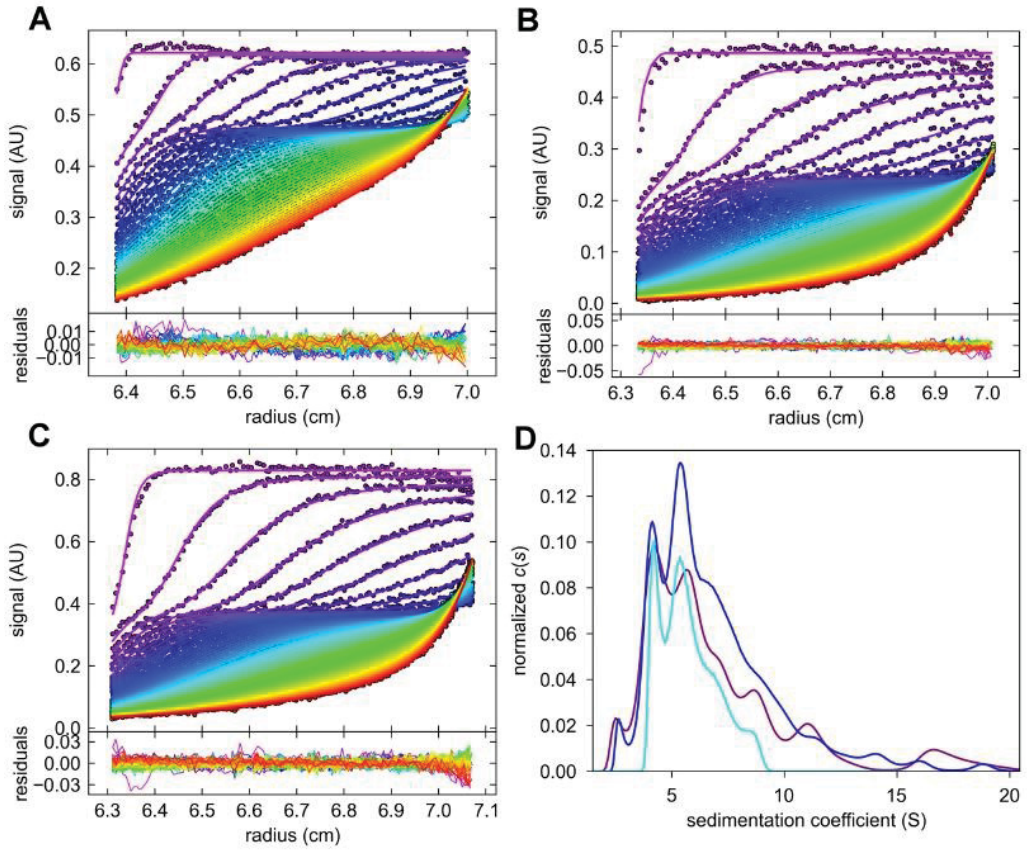

Fig 5. SV analysis of Aβ42 at different initial concentrations. The noise corrected data (dots) superimposed with fitted curves (lines) from *c*(*s*) analysis, and the residuals plot attached below, are shown for 40 μM (A), 80 μM (B), and 160 μM (C) initial concentrations of Aβ42. For clarity, only every second scan and every third data point is shown. The combined *c*(*s*) distributions for 40 μM (cyan) measured at 20°C, 80 μM (magenta) measured at 10°C, and 160 μM (blue) measured at 10°C are shown in (D). The monomer peak below 1 S has been excluded from the plot.

doi:10.1371/journal.pone.0127865.g005

Table 2. Observed *s*-value species of Aβ42. The oligomeric state was determined for a globular particle with $f/f_0 = 1.1$. The error was calculated as standard deviation of the mean of *s*-values obtained by applying the c(s) routine to the given number of different data sets. Different data sets correspond to independent sample preparations.

	***s*-value [10^{-13} s] ± SD**	**Number of data sets**
Monomer	0.62 ± 0.02	12
12-mer	4.70 ± 0.27	9
18-mer	6.25 ± 0.28	9

doi:10.1371/journal.pone.0127865.t002

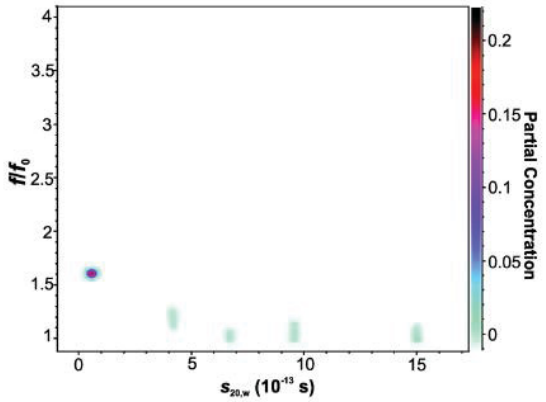

Fig 6. Pseudo-3D plot of Aβ42 size and shape distribution. Results from a SV analysis of 280 μM Aβ42 at 60,000 rpm and 10°C. Data were evaluated by 2-dimensional spectrum analysis followed by GA-MC analysis.

doi:10.1371/journal.pone.0127865.g006

equation

$$s^0_{20,w} = \frac{(1-\bar{\nu}\rho)}{(f/f_0 \cdot 6\eta)} \cdot \sqrt[3]{\frac{4}{3\bar{\nu}}\left(\frac{M \cdot n}{\pi \cdot N_A}\right)^2}$$

with solvent density (ρ) and viscosity (η) revealed for the 4.7 S species a size corresponding to 11 to 13 Aβ42 monomeric units (n M, M molecular weight of Aβ42) and for the 6.25 S species accordingly 17 to 20 monomeric Aβ42 units. The third species in the range of 6.2 to 7.6 S covers oligomeric species built from 22 to 29 monomeric units.

The determined sizes further supports prior evidence of a hexameric building block in Aβ42 aggregation [50–52] A hypothetical Aβ42 hexamer with an s-value between 1.9 (f/f_0 = 1.6) and 3.1 S (f/f_0 = 1.0) would be located within the predetermined gap between 1 and 4 S. The hexamer is not detected in solution because it is a kinetically unstable intermediate. The fraction of oligomeric species in solution is concentration dependent and reached 75% at 280 μM Aβ42 initial concentration; taking the 25% loss of Aβ42 during acceleration into account the fraction is 56%.

Although the described oligomers were detected free in solution for the first time, their sizes agree well with previously reported species. A dodecamer was detected by PICUP [6,52] and confirmed by ion mobility spectrometry-mass spectrometry [53]. Dodecameric assemblies were also described as Aβ-derived diffusible ligands and a specific assembly detected in cerebrospinal fluid, Aβ*56. Additionally, the oligomeric species termed globulomer [54] is a dodecamer, although the preparation of this species required SDS for maintaining stabilization. Experimental and theoretical evidence from MD simulations exists for the 18mer [55–57]. In contrast to our work, the 18mer reported in these references is dependent on hydrophobic interactions either with lipids in a bilayer or fatty acids. Kumar *et al.* [56] showed $c(s)$ distributions for their large fatty acid-derived Aβ oligomers with peaks at 5 and 7 S, which are similar to our $c(s)$ distributions obtained for Aβ42.

In our study of Aβ42, oligomerization clearly preceded the conversion to a β-sheet conformation. This is in contrast to an analytical ultracentrifugation based study of the prion protein (PrP), where the detected small oligomers showed significantly larger shape factors f/f_0 than the PrP monomer, and oligomerization happened in the same time frame as the structural conversion to a β-sheet dominated structure as demonstrated by CD measurements [24]. The 12-mer and the

18-mer were detected reproducibly under different speed conditions, temperature and initial Aβ42 concentrations. With increasing initial Aβ42 concentrations the fraction of these oligomers increased rather than larger aggregates forming. This is the first time that these species were detected free in solution. We suggest that these species are part of an oligomer formation pathway similar to the one proposed by Barghorn *et al.* [54] based on hexameric building blocks; although we believe that the two pathways for either fibril or oligomer formation are not completely separated from each other. To resolve this question, the addition of oligomers to monomeric Aβ solutions must be tested to determine whether a decrease in the lag phase is observed. Additionally, it should be clarified whether the observed oligomers are cytotoxic towards neuronal cells. Therefore, oligomers have to be purified away from monomers and larger assemblies.

Conclusions

The pathogenic aggregation mechanism of the amyloid beta peptide is still a matter of debate. Especially the nature of a postulated oligomer responsible for the neurodegeneration in Alzheimer's disease is elusive. In this study we utilized a technique that allows for observation of all species present within a sample at a given time point without complications arising from involvement of solid phases or necessity for any calibration. Size, shape, and quantity of all observed *s*-value species could be determined simultaneously, avoiding unaccounted changes in sample composition in the course of multi-step analysis procedures. In contrast to our expectations it was possible to increase the initial Aβ42 concentration above 1 mg/ml without generating larger aggregates and fibrils within the experimental time frame. This was caused or at least supported by the reduced temperature of 10°C and the property of the SV method to deplete solutions of larger aggregates, which might act as seeds for amyloid formation. Such particles with high *s*-values are removed by their rapid sedimentation during the early phases of centrifugation, i.e., by their rapid sedimentation already during the acceleration phase. We were able to demonstrate the existence of distinct oligomeric species in solutions of Aβ42 during the lag phase of amyloid formation. These oligomers appeared to be globular in shape, while the monomer showed a slightly extended conformation. During the experiment, starting from a homogeneously filled cell, the characterized oligomers sedimented always in the presence of smaller species, thus maintaining equilibrium between distinct oligomeric species and smaller oligomers and monomers. The postulated equilibrium is in agreement with the observation that increasing the initial Aβ42 concentration led rather to an increase of the oligomer fraction than to the appearance of aggregates above 20 S.

The two recurring species were interpreted as an 11 to 13mer for the smaller and a 17 to 20mer for the larger oligomer assuming a frictional ratio between 1.0 and 1.1. The numbers are tempting to suggest a model based on a hexameric building block as recently proposed in [58]. The high reproducibility of the *s*-values as well as their independence from the initial Aβ42 concentration clearly indicates the existence of energetically favored assemblies among possible oligomeric states. It can be assumed that the defined size of the oligomers correlates with an equally well defined secondary and tertiary structure. Such characterized species would be ideal candidates for specific, pathogenic interactions with cellular receptors or other interaction partners. Whether the observed oligomers are on or off-pathway to the amyloid fibrils cannot be concluded, although it seems probable that once a certain number of monomeric units are assembled this might be the place where—triggered by a conformational rearrangement—the rapid growth of fibrillar structures initiates.

Acknowledgments

Computing time and computational support for UltraScan III software was provided by the Texas Advanced Computing Centre from UT Austin, and is supported by a NSF Teragrid

Allocation grant TGMCB070038. The authors thank the Helmholtz Association for funding this work through the Helmholtz-Portfolio Topics "Technology and Medicine" and "Drug Research". The authors wish to thank Andrew J. Dingley for his critical proofreading of the manuscript.

Author Contributions

Conceived and designed the experiments: MW DU BZ LNS. Performed the experiments: MW DU. Analyzed the data: MW DU LNS. Contributed reagents/materials/analysis tools: DW. Wrote the paper: MW LNS. Reviewed and edited manuscript: LNS VG DW.

References

1. Brookmeyer R, Johnson E, Ziegler-Graham K, Arrighi HM (2007) Forecasting the global burden of Alzheimer's disease. Alzheimer's & dementia: the journal of the Alzheimer's Association 3: 186–191.
2. Masters CL, Selkoe DJ (2012) Biochemistry of amyloid beta-protein and amyloid deposits in Alzheimer disease. Cold Spring Harbor perspectives in medicine 2: a006262. doi: 10.1101/cshperspect.a006262 PMID: 22675658
3. Yankner BA, Lu T (2009) Amyloid beta-protein toxicity and the pathogenesis of Alzheimer disease. The Journal of biological chemistry 284: 4755–4759. doi: 10.1074/jbc.R800018200 PMID: 18957434
4. Finder VH, Glockshuber R (2007) Amyloid-beta aggregation. Neuro-degenerative diseases 4: 13–27. PMID: 17429215
5. Klyubin I, Cullen WK, Hu NW, Rowan MJ (2012) Alzheimer's disease Abeta assemblies mediating rapid disruption of synaptic plasticity and memory. Molecular brain 5: 25. doi: 10.1186/1756-6606-5-25 PMID: 22805374
6. Roychaudhuri R, Yang M, Deshpande A, Cole GM, Frautschy S, Lomakin A, et al. (2013) C-terminal turn stability determines assembly differences between Abeta40 and Abeta42. Journal of Molecular Biology 425: 292–308. doi: 10.1016/j.jmb.2012.11.006 PMID: 23154165
7. Lambert MP, Barlow AK, Chromy BA, Edwards C, Freed R, Liosatos M, et al. (1998) Diffusible, nonfibrillar ligands derived from Abeta1–42 are potent central nervous system neurotoxins. Proc Natl Acad Sci USA 95: 6448–6453. PMID: 9600986
8. Wang HW, Pasternak JF, Kuo H, Ristic H, Lambert MP, Chromy B, et al. (2002) Soluble oligomers of beta amyloid (1–42) inhibit long-term potentiation but not long-term depression in rat dentate gyrus. Brain Res 924: 133–140. PMID: 11750898
9. Walsh DM, Klyubin I, Fadeeva JV, Rowan MJ, Selkoe DJ (2002) Amyloid-beta oligomers: their production, toxicity and therapeutic inhibition. Biochem Soc Trans 30: 552–557. PMID: 12196135
10. Klein WL, Krafft GA, Finch CE (2001) Targeting small A beta oligomers: the solution to an Alzheimer's disease conundrum?. Trends Neurosci 24: 219–224. PMID: 11250006
11. Querfurth HW, LaFerla FM (2010) Mechanisms of disease: Alzheimer's disease. N Engl J Med 362: 329–344. doi: 10.1056/NEJMra0909142 PMID: 20107219
12. Glabe CG (2008) Structural classification of Toxic Oligomers. J Biol Chem 283: 29639–29643. doi: 10.1074/jbc.R800016200 PMID: 18723507
13. Larson ME, Lesne SE (2012) Soluble Abeta oligomer production and toxicity. Journal of neurochemistry 120 Suppl 1: 125–139. doi: 10.1111/j.1471-4159.2011.07478.x PMID: 22121920
14. Benilova I, Karran E, De Strooper B (2012) The toxic Abeta oligomer and Alzheimer's disease: an emperor in need of clothes. Nature neuroscience 15: 349–357. doi: 10.1038/nn.3028 PMID: 22286176
15. Hayden EY, Teplow DB (2013) Amyloid beta-protein oligomers and Alzheimer's disease. Alzheimer's research & therapy 5: 60.
16. Harding SE, Rowe AJ (2010) Insight into protein-protein interactions from analytical ultracentrifugation. Biochemical Society transactions 38: 901–907. doi: 10.1042/BST0380901 PMID: 20658974
17. Howlett GJ, Minton AP, Rivas G (2006) Analytical ultracentrifugation for the study of protein association and assembly. Current opinion in chemical biology 10: 430–436. PMID: 16935549
18. Correia JJ (2010) Analysis of tubulin oligomers by analytical ultracentrifugation. Methods in cell biology 95: 275–288. doi: 10.1016/S0091-679X(10)95015-2 PMID: 20466140
19. Gabrielson JP, Arthur KK (2011) Measuring low levels of protein aggregation by sedimentation velocity. Methods 54: 83–91. doi: 10.1016/j.ymeth.2010.12.030 PMID: 21187149
20. Mok YF, Howlett GJ (2006) Sedimentation velocity analysis of amyloid oligomers and fibrils. Methods in enzymology 413: 199–217. PMID: 17046398

21. Liu J, Andya JD, Shire SJ (2006) A critical review of analytical ultracentrifugation and field flow fractionation methods for measuring protein aggregation. The AAPS journal 8: E580–589. PMID: 17025276

22. Fawzi NL, Ying J, Ghirlando R, Torchia DA, Clore GM (2011) Atomic-resolution dynamics on the surface of amyloid-beta protofibrils probed by solution NMR. Nature 480: 268–272. doi: 10.1038/nature10577 PMID: 22037310

23. Mok YF, Ryan TM, Yang S, Hatters DM, Howlett GJ, Griffin MD (2011) Sedimentation velocity analysis of amyloid oligomers and fibrils using fluorescence detection. Methods 54: 67–75. doi: 10.1016/j.ymeth.2010.10.004 PMID: 21055469

24. Trevitt CR, Hosszu LL, Batchelor M, Panico S, Terry C, Nicoll AJ, et al. (2014) N-terminal domain of prion protein directs its oligomeric association. The Journal of biological chemistry 289: 25497–25508. doi: 10.1074/jbc.M114.566588 PMID: 25074940

25. Hosszu LL, Trevitt CR, Jones S, Batchelor M, Scott DJ, Jackson GS, et al. (2009) Conformational properties of beta-PrP. The Journal of biological chemistry 284: 21981–21990. doi: 10.1074/jbc.M809173200 PMID: 19369250

26. Lamm O (1929) Die Differentialgleichung der Ultrazentrifugierung. Ark Mat Astr Fys 21B: 1–4.

27. Schuck P (2000) Size-distribution analysis of macromolecules by sedimentation velocity ultracentrifugation and lamm equation modeling. Biophysical journal 78: 1606–1619. PMID: 10692345

28. Demeler B (2005) UltraScan A Comprehensive Data Analysis Software Package for Analytical Ultracentrifugation Experiments. In: Scott DJ, Harding SE, Rowe AJ, editors. Modern Analytical Ultracentrifugation: Techniques and Methods. Cambridge: Royal Society of Chemistry (UK). pp. 210–229.

29. Demeler B, Brookes E, Nagel-Steger L (2009) Analysis of heterogeneity in molecular weight and shape by analytical ultracentrifugation using parallel distributed computing. Methods in enzymology 454: 87–113. doi: 10.1016/S0076-6879(08)03804-4 PMID: 19216924

30. Nagel-Steger L, Demeler B, Meyer-Zaika W, Hochdorffer K, Schrader T, Willbold D (2010) Modulation of aggregate size- and shape-distributions of the amyloid-beta peptide by a designed beta-sheet breaker. European biophysics journal: EBJ 39: 415–422. doi: 10.1007/s00249-009-0416-2 PMID: 19238376

31. Findeis MA (2007) The role of amyloid beta peptide 42 in Alzheimer's disease. Pharmacology & therapeutics 116: 266–286.

32. Kar SR, Kingsbury JS, Lewis MS, Laue TM, Schuck P (2000) Analysis of Transport Experiments Using Pseudo-Absorbance Data. Analytical Biochemistry 285: 135–142. PMID: 10998273

33. Demeler B (2014) UltraScan Software. A Comprehensive Data Analysis Software Package for Analytical Ultracentrifugation Experiments. Web. 22 November 2014. Available: http://ultrascan.uthscsa.edu/index.php.

34. Schuck P (2014) SEDFIT. Web. 22 November 2014. Available: http://www.analyticalultracentrifugation.com/default.htm.

35. Brookes E, Cao W, Demeler B (2010) A two-dimensional spectrum analysis for sedimentation velocity experiments of mixtures with heterogeneity in molecular weight and shape. European biophysics journal: EBJ 39: 405–414. doi: 10.1007/s00249-009-0413-5 PMID: 19247646

36. Laue TM, Shah BD, Ridgeway TM, Pelletier SL (1992) Computer-aided interpretation of analytical sedimentation data for proteins. In: Harding S, Rowe A, Horton JC, editors. Analytical Ultracentrifugation in Biochemistry and Polymer Science. Cambridge: Royal Society of Chemistry pp. 90–125. doi: 10.1007/s00249-009-0425-1 PMID: 19266192

37. Laue TM (2014) SEDNTERP. Web. 22 November 2014. Available: http://bitcwiki.sr.unh.edu/index.php/Main_Page.

38. Cohn EJ, Edsall JT (1943) Proteins, Amino Acids and Peptides. New York: Reinhold.

39. Durchschlag H (1986) Thermodynamic Data for Biochemistry and Biotechnology; H H-J, editor. Berlin Heidelberg New York: Springer. 84 p.

40. Fezoui Y, Hartley DM, Harper JD, Khurana R, Walsh DM, Condron MM, et al. (2000) An improved method of preparing the amyloid beta-protein for fibrillogenesis and neurotoxicity experiments. Amyloid: the international journal of experimental and clinical investigation: the official journal of the International Society of Amyloidosis 7: 166–178. PMID: 11019857

41. Fezoui Y, Teplow DB (2002) Kinetic studies of amyloid beta-protein fibril assembly. Differential effects of alpha-helix stabilization. The Journal of biological chemistry 277: 36948–36954. PMID: 12149256

42. Hepler RW, Grimm KM, Nahas DD, Breese R, Dodson EC, Acton P, et al. (2006) Solution state characterization of amyloid beta-derived diffusible ligands. Biochemistry 45: 15157–15167. PMID: 17176037

43. Tomaselli S, Esposito V, Vangone P, van Nuland NAJ, Bonvin AMJJ, Guerrini R, et al. (2006) The α-to-β Conformational Transition of Alzheimer's Aβ-(1–42) Peptide in Aqueous Media is Reversible: A Step

by Step Conformational Analysis Suggests the Location of β Conformation Seeding. Chembiochem: a European journal of chemical biology 7: 257–267.

44. Rai N, Nollmann M, Spotorno B, Tassara G, Byron O, Rocco M (2005) SOMO (SOlution MOdeler) differences between X-Ray- and NMR-derived bead models suggest a role for side chain flexibility in protein hydrodynamics. Structure 13: 723–734. PMID: 15893663

45. Brookes E, Demeler B, Rosano C, Rocco M (2010) The implementation of SOMO (SOlution MOdeller) in the UltraScan analytical ultracentrifugation data analysis suite: enhanced capabilities allow the reliable hydrodynamic modeling of virtually any kind of biomacromolecule. European biophysics journal: EBJ 39: 423–435. doi: 10.1007/s00249-009-0418-0 PMID: 19234696

46. van Holde KE, Weischet WO (1978) Boundary analysis of sedimentation velocity experiments with monodisperse and paucidisperse solutes. Biopolymers 17: 1387–1403.

47. Dam J, Velikovsky CA, Mariuzza RA, Urbanke C, Schuck P (2005) Sedimentation velocity analysis of heterogeneous protein-protein interactions: Lamm equation modeling and sedimentation coefficient distributions c(s). Biophysical journal 89: 619–634. PMID: 15863475

48. Legleiter J (2011) Assessing Abeta aggregation state by atomic force microscopy. Methods in molecular biology 670: 57–70. doi: 10.1007/978-1-60761-744-0_5 PMID: 20967583

49. Gu L, Liu C, Guo Z (2013) Structural insights into Abeta42 oligomers using site-directed spin labeling. The Journal of biological chemistry 288: 18673–18683. doi: 10.1074/jbc.M113.457739 PMID: 23687299

50. Roychaudhuri R, Yang M, Hoshi MM, Teplow DB (2009) Amyloid beta-protein assembly and Alzheimer disease. J Biol Chem 284: 4749–4753. doi: 10.1074/jbc.R800036200 PMID: 18845536

51. Lesne S, Koh MT, Kotilinek L, Kayed R, Glabe CG, Yang A, et al. (2006) A specific amyloid-beta protein assembly in the brain impairs memory. Nature 440: 352–357. PMID: 16541076

52. Bitan G, Kirkitadze MD, Lomakin A, Vollers SS, Benedek GB, Teplow DB (2003) Amyloid beta-protein (Abeta) assembly: Abeta 40 and Abeta 42 oligomerize through distinct pathways. Proceedings of the National Academy of Sciences of the United States of America 100: 330–335. PMID: 12506200

53. Bernstein SL, Dupuis NF, Lazo ND, Wyttenbach T, Condron MM, Bitan G, et al. (2009) Amyloid-beta protein oligomerization and the importance tetramers and dodecamers in the aetiology of Alzheimer's disease. Nat Chem 1: 326–331. doi: 10.1038/nchem.247 PMID: 20703363

54. Barghorn S, Nimmrich V, Striebinger A, Krantz C, Keller P, Janson B, et al. (2005) Globular amyloid beta-peptide oligomer—a homogenous and stable neuropathological protein in Alzheimer's disease. Journal of neurochemistry 95: 834–847. PMID: 16135089

55. Jang H, Teran Arce F, Ramachandran S, Kagan BL, Lal R, Nussinov R (2013) Familial Alzheimer's Disease Osaka Mutant (DeltaE22) beta-Barrels Suggest an Explanation for the Different Abeta Preferred Conformational States Observed by Experiment. The journal of physical chemistry B.

56. Kumar A, Paslay LC, Lyons D, Morgan SE, Correia JJ, Rangachari V (2012) Specific soluble oligomers of amyloid-beta peptide undergo replication and form non-fibrillar aggregates in interfacial environments. The Journal of biological chemistry 287: 21253–21264. doi: 10.1074/jbc.M112.355156 PMID: 22544746

57. Kumar A, Bullard RL, Patel P, Paslay LC, Singh D, Bienkiewicz EA, et al. (2011) Non-esterified fatty acids generate distinct low-molecular weight amyloid-beta (Abeta42) oligomers along pathway different from fibril formation. PloS one 6: e18759. doi: 10.1371/journal.pone.0018759 PMID: 21526230

58. Lendel C, Bjerring M, Dubnovitsky A, Kelly RT, Filippov A, Antzutkin ON, et al. (2014) A hexameric peptide barrel as building block of amyloid-beta protofibrils. Angewandte Chemie 53: 12756–12760. doi: 10.1002/anie.201406357 PMID: 25256598

2.3 Studying soft-matter and biological systems on a wide length scale from nanometer to micrometer sizes at the small-angle neutron diffractometer KWS-2

Aurel Radulescu, Noemi Kinga Szekely, Marie-Sousai Appavou, Vitaliy Pipich, Thomas Kohnke, Vladimir Ossovyi, Simon Staringer, Gerald, J. Schneider, Matthias Amann, Bo Zhang-Haagen, Georg Brandl, Matthias Drochner, Ralf Engels, Romulad Hanslik, Günther Kemmerling

Status: accept in Journal of Visualized Experiments

Impact Factor:1.1

Proportion of contribution 5%

Contributions: Conceived, designed and performed the experiments of amyloid beta protein; Analyzed the data the experiments of amyloid beta protein.

Studying soft-matter and biological systems on a wide length scale from nanometer to micrometer sizes at the small-angle neutron diffractometer KWS-2

CORRESPONDING AUTHOR: Aurel Radulescu (a.radulescu@fz-juelich.de)

KEYWORDS: Small-angle neutron scattering (SANS), high-resolution SANS; high-intensity SANS, focusing SANS, soft-matter systems, biophysical systems

LONG ABSTRACT:

KWS-2 represents a SANS diffractometer which, by combining classical pinhole, focusing (with lenses) and time-of-flight (with chopper) methods, is optimized for the exploration of a wide momentum transfer Q range, between $1x10^{-4}$ and 0.5 $Å^{-1}$, at high neutron intensities and with adjustable resolution. By its concept and performance parameters and being equipped with specific sample environments and ancillary devices, the instrument is dedicated to investigation of soft-matter and biophysical systems over a wide length scale, from nm up to μm. Structures and morphologies at equilibrium or under transformation due to kinetical processes spanning a wide time scale, between minutes and tens of milliseconds, can be studied in static or time-resolved approaches. By enabling the possibility to adjust at will, during the experiment, either the intensity or the resolution within wide limits, KWS-2 shows an increased flexibility in use and a high versatility in addressing a broad range of structural and morphological studies in the field, from the investigation of small and weak scattering systems, like single polymers and proteins in dilute solutions, up to resolving complex, hierarchical systems that exhibit multiple structural levels, like gels, networks or macro-aggregates. With the recent upgrade of the detection system, MHz count rates became detectable, which opens new opportunities for the study of very small biological morphologies in solution, which deliver weak scattering signals above the buffer scattering level at high Q. The use of the multiple working modes that are offered by the KWS-2 instrument and the performance that can be achieved will be reported here in details.

INTRODUCTION:

Soft and biological materials show a rich variety of morphologies which are characterized by features such as self-organization and self-assembly of elementary units to larger, complex aggregates, cooperative interplay of a large number of degrees of freedom, weak interaction between the structural units and thus high sensitivity to external fields, and spatio-temporal correlations that can span a huge range from nanometers to millimeters and from nanoseconds to days. Because of the large range of relevant length and time scales the experimental characterization of the properties of these materials are very challenging. Scattering techniques with neutrons play an important role in the investigation of the structure, dynamics and thermodynamic properties of such complex systems. As unique probe, neutrons offer the advantage of different interaction between the ^{1}H and ^{2}H (deuterium, D) hydrogen isotopes. The large difference in the coherent scattering length density between hydrogen and deuterium represents the basis of the contrast variation and contrast matching methods using neutron scattering on hydrocarbon samples, which most of the soft-matter and biological systems are. Thus, by the possibility to vary the coherent scattering length density of a compound over a broad range by hydrogen/deuterium (H/D) substitution, a selected constituent in a complex system can be made "visible" or "invisible" as depending upon its contrast – the squared difference between its scattering length density and that of the other components – without altering the system chemically. By contrast matching and contrast variation separate analyses of selected components or regions within a complex soft-matter or biophysical morphology can be thus performed. Furthermore, neutrons are highly penetrating and can be used as non-destructive probes and for studying samples in special environments, when the contribution from the additional materials placed in beam can be reliably measured and corrected for.

Elastic scattering experiments deliver information about the structure and morphology of a sample in real space through the inverse Fourier transformation of the scattered intensity measured in reciprocal space as a function of the momentum transfer Q, where $Q=4\pi/\lambda \sin\theta/2$, with λ - the neutron wavelength and θ - the scattering angle. Thus, large Q values relate to short length scales, with the inter-atomic correlations investigated by classical neutron diffraction (ND), while at small Q large length scales can be explored by small-angle neutron scattering (SANS). Typically, single or assembling synthetic or natural

macromolecules in solution, melt, film or bulk samples are characterized over a wide length scale from nanometer and micrometer sizes via the application of the classical pin-hole SANS and the ultra-SANS (based on focusing or single-crystal diffractometry) techniques. However, the combination of different methods/facilities for achieving a complete structural characterization is sometimes difficult because of issues such as available amount of sample, stability of samples over longer time, reproducibility of effects in special thermodynamic conditions, as well as the joint analysis of experimental data obtained in different experimental geometries. Moreover, the studies that are dealing with structures and fast structural changes which are characterized by high space or time resolution are very challenging, requiring very special experimental setups. Therefore, the development of a highly versatile SANS instruments where limits can be pushed beyond the typical configuration in an easy and practicable manner is beneficial for meeting all special demands from the user community.

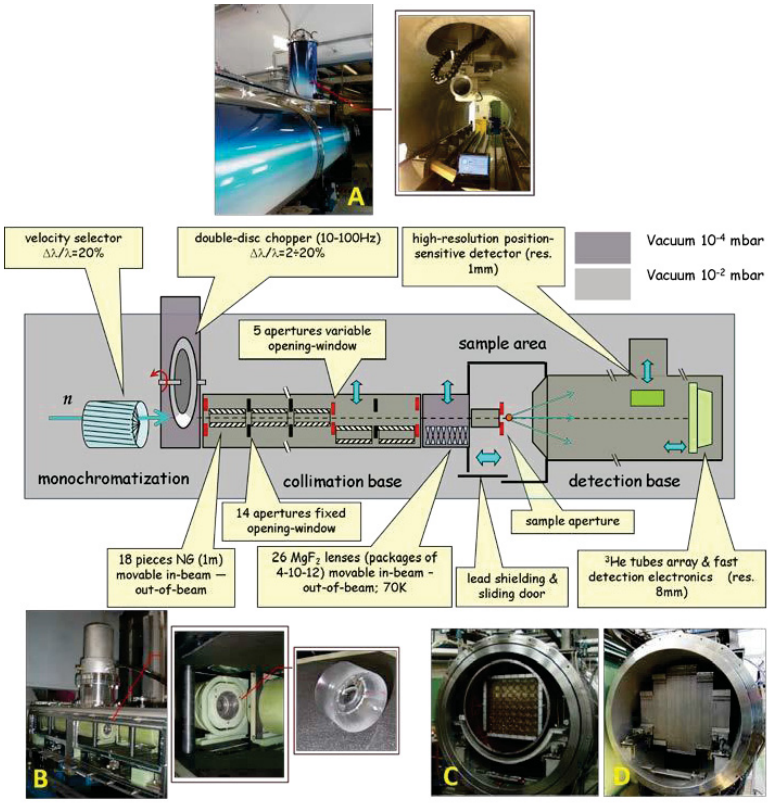

Figure 1: Layout of KWS-2 SANS instrument, including all upgrades done between 2010 and 2015: A – the secondary high-resolution detector and its tower on the top of the vacuum tank; B – the MgF_2 focusing lenses grouped in three packages and their cooling system (cold head); C – the old main detector (scintillation) with its 8x8 array of photomultipliers and D – the new main detector (^{3}He tubes) with larger detection area.

The SANS diffractometer KWS-2 (Figure 1), operated by the Jülich Centre of Neutron Science (JCNS) at Heinz Maier-Leibnitz Center (MLZ) in Garching, is originally a classical pinhole SANS instrument which, benefiting from a high neutron flux (Figure 2) delivered by the FRM II neutron source[1] and the dedicated guide system[2-4] and through repeated upgrades, was optimized for the exploration of a wide Q-range, between $1x10^{-4}$ and 0.5 $Å^{-1}$, at high neutron intensities and with adjustable resolution. Being equipped with specific sample environments and ancillary devices (Table 1), the instrument is adapted to the study of soft-matter and biophysical systems over a wide length scale, from nm up to □m, through static or time-resolved investigations of structures and morphologies at equilibrium or under transformation due to kinetical processes spanning a wide time scale, between minutes and tens of milliseconds. In conventional working mode (Figure 3), through the variation of the sample-to-detector distance and/or the wavelength, a Q-range between $7x10^{-4}$ $Å^{-1}$ and 0.5 $Å^{-1}$ can be covered, which means that structural levels and correlation effects on a length scale from 10Å up to 9000Å can be inspected in the real space (where the dimension is considered as $2\pi/Q$). The selection of the wavelength, between 4.5Å and 20Å, using a mechanical monochromator (velocity selector) that provides a wavelength spread $\Delta\lambda/\lambda$=20%, the variation of the collimation conditions (collimation length L_C and apertures opening, A_C – the entrance aperture, following the last neutron guide segment in beam, and A_S – the sample aperture, just in front of the sample) and of detection distance L_D are done automatically, via computer control.

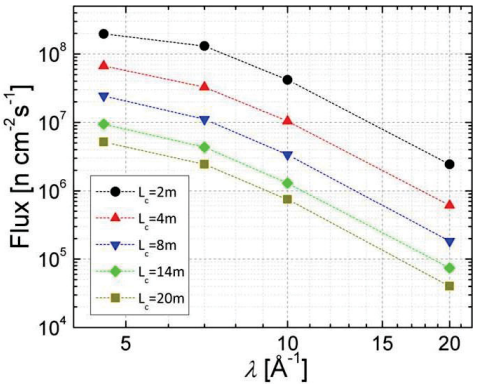

Figure 2: The neutron flux at the sample position (status 2013).

Considerable upgrades, aiming for boosting the performance with respect to the intensity on the sample, the instrumental resolution, the minimum momentum transfer Q_m and the fast detection at high count rates in the MHz range, were recently carried out, which resulted in equipping the instrument with:

(1) a double-disc chopper[5] with variable slit opening (Figure 4) and time-of-flight (TOF) data acquisition mode; the opening time τ_w of the neutron guide can be adjusted by varying the chopper frequency $f_{chopper}$ between 10Hz and 100 Hz and the angular opening of the two

chopper window, $\Delta\varphi$, between 0° and 90° by changing the positioning of the two discs with respect to each other; the improvement in wavelength resolution $\Delta\lambda/\lambda$ is achieved by shortening τ_w (by decreasing and/or increasing $f_{chopper}$) and by splitting the pulses recorded on the detector in an appropriate number of time channels that match τ_w in width and are characterized by the aimed.

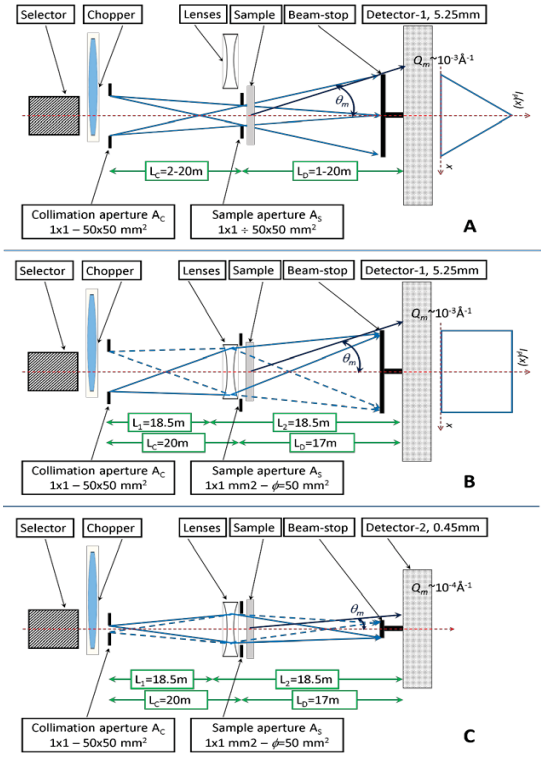

Figure 3: Schematic view of three working modes offered at KWS-2: A – conventional pin-hole ; for L_C=L_D and optimal pinhole condition A_C=2A_S, the beam profile I_P at the detector is approximately triangular with a base width equal to 2A_C; B – the high-intensity focusing mode; using lenses, larger samples can be measured with the same resolution as in the conventional pinhole mode (the beam profile I_P at the detector is rectangular in this case); C – the high-resolution (extended Q-range) focusing mode; using lenses and a small entrance aperture A_C (typically 4mm x 4mm) that is placed in one focal point of the lenses system a small beam is transmitted on the detector, which is placed in the other focal point of lenses, hence a smaller Q_m than in conventional mode can be reached.

□□□□□

(2) focusing elements – magnesium fluorite MgF_2 parabolic lenses[6] with a diameter of 50mm (Figure 1); 26 MgF_2 lenses are grouped in three packages (4+6+16 lenses), which can be moved independently in beam, for achieving the focusing conditions with different wavelengths within the range λ=7-20Å; in order to increase the transmission by reducing the scattering on phonons in the lens material, the lenses are kept at 70K using a special cooling system.

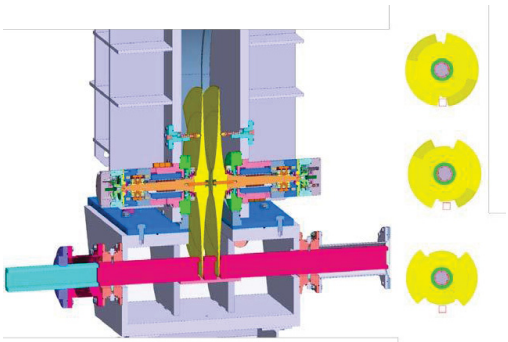

Figure 4: Schematic view of double disc chopper with variable slit opening (right); the slit opening $\Delta\varphi$ can be adjusted between 0° and 90° so that, depending also on the chopper frequency $f_{chopper}$, the opening time τ_w of the guide (red rectangle on the right series of pictures) can be varied.

(3) a secondary high-resolution position-sensitive detector (scintillation, 1mm position resolution and 0.45mm pixel-size), which is vertically movable in or out the beam (Figure 1); the small detector is typically parked in the tower on the top of the vacuum tank and brought in beam in a controlled way, when high-resolution investigations (low Q) using lenses are intended[4, 7] and the main detector is parked in the end position of the tank, at 20m; the small detector is placed at a fixed distance after the sample, L_D=17m, in one focal point of the lenses system (when a small entrance aperture at L_C=20m would be in this case in the other focal point of the lenses system).

(4) a new main detection system, which consists of an array of 144 ^{3}He tubes (with a global efficiency per tube of 85% for λ=5Å) that defines an active detection area equivalent to 0.9 m^2 (Figure 1) and an innovative rapid readout electronics, which is mounted in a closed case on the backside of the ^{3}He tubes frame for reasons of improving the read-out characteristics and reducing the noise. The new system that replaced the old scintillation detector (^{6}Li scintillator and an array of 8x8 photomultipliers, Figure 1) is characterized by an effective dead-time constant of 25ns and an overall count rate as high as 5MHz at 10% dead-time for flat profiles. These features are due to the fact that the system contains independent channels operated in parallel, which is an advantage over systems that experience dead-time after an event. The much higher count rate shortens the measurement times and therefore, increases the number of experiments in the same time period.

With all these innovations, the instrument became a highly versatile tool that can address a broad range of structural studies by offering multiple working modes (Table 2) that can be selected and used in a direct and user-friendly manner. In the **high-intensity mode** (Figure 3), up to twelve times intensity gain compared to the conventional pinhole mode for the same resolution can be achieved with lenses based on increasing of the sample size. In the **tunable resolution mode**, with chopper and TOF data acquisition, improved characterization of the scattering features within different Q ranges is enabled by the possibility to vary the wavelength resolution $\Delta\lambda/\lambda$ between 2% and 20%[5]. In the **extended *Q*-range mode** (Figure 3), by means of lenses and the secondary high-resolution detector, a Q_m down to 1 x 10^{-4} $Å^{-1}$ can be achieved, which in combination with the pinhole mode, permits the exploration of sizes over a continuous length scale from nm to micron range. The use of chopper for narrowing $\Delta\lambda/\lambda$ provides accurate beam characteristics by avoiding the gravity and chromatic effects while using the lenses. In the **real-time mode**, by exploiting the high intensity and

external triggering of data acquisition by sample environments, structural changes can be resolved with time resolutions down to 50ms. By improving the wavelength resolution down to $\Delta\lambda/\lambda$=5% with the chopper, time resolutions as good as 2ms can be realized.

Here, we will present in details how typical experiments are conducted at KWS-2 in all working modes and how the reduction of data collected in these modes can be performed, for obtaining the structural information of interest about the investigated sample.

PROTOCOL:

1. Positioning the sample holder / sample environment on the sample stage

1.1) Define the needed space at the sample position for the sample holder which will be used, by adjusting the length of the collimation nose (Figure 5). Select from the stored configurations at the nose control system the appropriate one for the sample holder/sample environment that is planned to be used.

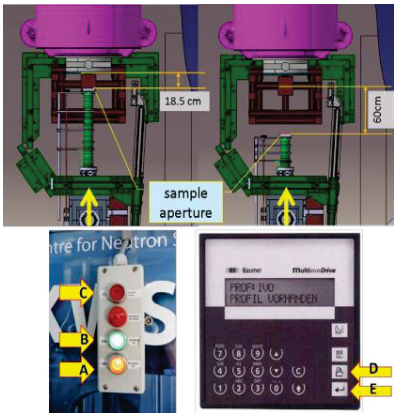

Figure 5: Schematic top view of the sample area of KWS-2 (A) in two configurations of the collimation nose), showing the available space for the installation of various sample environments in beam (the neutrons are coming from the bottom) and images of the handling panel of the lead door (B) and the handling panel of the collimation nose (C). From the door panel one can open (1) or close (2) the door or can quit the failure (3) that is indicated in case the door movement is interrupted due to activation of safety elements. From the nose panel one can select an appropriate configuration (4) and execute the nose movement positioning by keeping the button 5 continuously activated until the selected positioning is reached and the movement stops.

1.2) Select the appropriate cell type and geometry (Figure 6) for the experiment and fill the sample in the cells in the sample preparation laboratory of FRM II.

1.3) Select the appropriate cell holder for the purpose of experiment, i.e. for investigation at ambient temperature or at controlled temperature (Figures6 and 7).

1.4) Load the cartridges of the sample holder (Figures 6 and 7) or the holder support (in the case of large cells like in Figure 6) with sample cells and cover them with the Cd-coated Al-cover plates (Figure 7) or borated plastic masks (Figure 6) in the sample preparation laboratory of FRM II (the Cd or borated plastic faces must be oriented on the neutron side).

1.5) Fix the cartridges on the Al-frame (Figure 7) in the sample preparation laboratory of FRM II; Note: the steps 1.2 - 1.4 should be done similarly in the case of any other cell holder that is planned to be used. For special sample environments (rheometer, pressure cell, humidity cell, etc.) the special sample cells must be filled also in the sample preparation laboratory of FRM II.

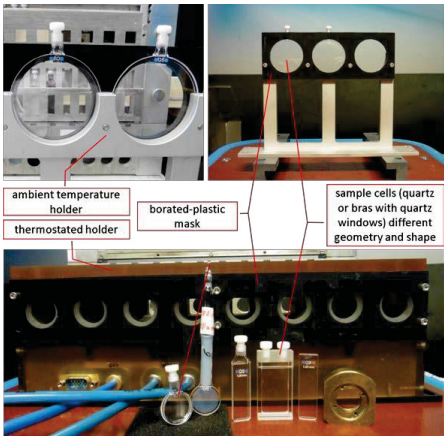

Figure 7: View of one of the multilevel/multi-position cell-holders used at KWS-2 for measurements at ambient conditions; the three levels can be equipped with cartridges designed for different cell geometries that are closed with covers equipped with Cd shielding on the face towards neutrons; the positioning of the holder on the sample stage is predetermined (in X, Y coordinates).

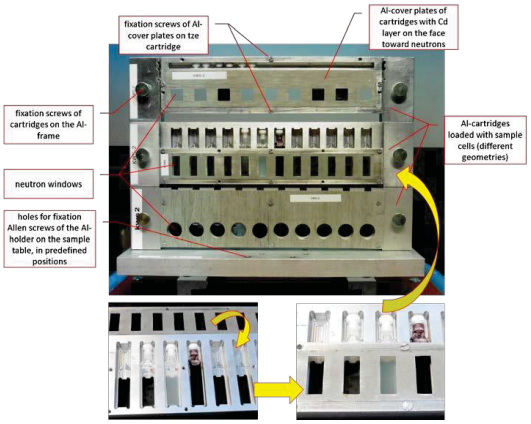

Figure 6: Overview of the quartz or bras cells that are used as sample container at KWS-2 in conventional (bottom) or high-intensity focusing (top) modes with different beam sizes. Cells with 1mm and 2mm beam path are available; the three positions cell holder (top) for measurements with lenses or the 8-positions thermostated cell holder (bottom) that are equipped with borated plastic masks enable series of measurements with automatic, computer controlled, sample change in beam.

1.6) Install the appropriate sample holder/sample environment on the sample stage in the predetermined position on the sample stage, using Allen screws (example in Figure 8). Note: the current Protocol presents the case of working with holders for quartz cells typically used in experiments at KWS-2; the use of special sample environments, like for example the pressure cell (Figure 8), rheometer or humidity cell, requires special assistance from the instrument team.

1.7) Close the motorized sliding lead door (Figure 5) by using the knobs on its outer side, keeping the knobs activated until the door reaches the end position, which will be indicated by a luminous signal; Note: without the door completely closed and the end-switch activated, the beam shutter cannot be opened, neither manually, nor from the measurement control software; the software will require in this case an additional check of the issue, before starting of the measurement.

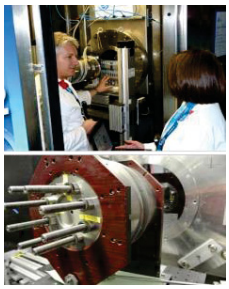

Figure 8: Installation of the multilevel/multi-position sample holder (top) for measurements at ambient temperature (Photo credits: Wenzel Schürmann, TU München) and of a typical sample environment (pressure cell – bottom) on the sample stage of KWS-2; the sample aperture is positioned just in front of the holder; during measurement programs the holder is moved laterally and vertically in order to bring each cell in beam, in an automatic, computer controlled, way; the measurements with pressure cell are carried out at a fixed position of the cell in beam.

2. Planning of Experiments

2.1) Choose the adequate experimental configuration/mode for performing the investigation in a Q-range that is appropriate to the length scale of structures and correlation effects revealed by the sample. Check the dynamical range of the instrument[4] (Table 2).

2.2) Choose the adequate experimental configuration/mode for enabling proper intensity on the sample in order to optimize either the measurement time and to match the sample stability time, for static investigations, or the appropriate time step, for time-resolved investigation of structural changes. Check the intensity map for different experimental configurations (Table 2, Figure 2).

2.3) Choose the adequate experimental configuration/mode for providing a proper resolution in order to enable the resolving of fine scattering features occurring due to ordering effects in the sample. Check the possibility to tune the wavelength resolution $\Delta\lambda/\lambda$[5] (Table 2).

3. Preparation of the measurement software and conducting/visualizing the experiment

3.1) Start the measurement software KWS2TC in a terminal window at the measurement control computer of the KWS-2 instrument (Figure 9) and use the left set of functions to carry out the configuration, definition, startup and control and the visualization of the measurement.

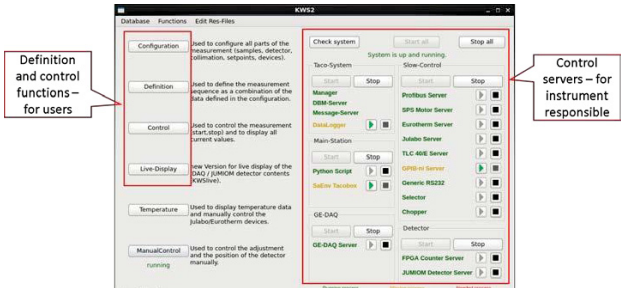

Figure 9: The main user interface of the measurement control/visualization software at KWS-2; the left side functions can be used by the experimentalists, while the right side functions and indicators are used by the instrument responsible.

3.2) Select Configuration in the main menu (Figure 9) to activate the kws2-Configuration menu (Figure 10) for defining the user data and configuring the

elementary motor positions and the set-points for the devices/fields on the sample.

Note: for regular users only the options **UserData**, **Sample** and **Set Points** options are of a direct interest, the other options refer to components of the instrument that are predefined and changes can be operated only under the supervision of the instrument scientist.

3.2.1) Select **UserData** (Figure 10, upper functions menu) and fill the fields **User name**, **E-mail**, **First part of filename** and **Measurement comment** in the User data menu (view/edit). Leave the menu with Save.

Note: as the first part of filename typically the proposal number is considered; do not use special characters, like _, @, $, etc., for the file name prefix.

3.2.2) Select **Sample** (Figure 10) for activating the **Sample configuration** menu.

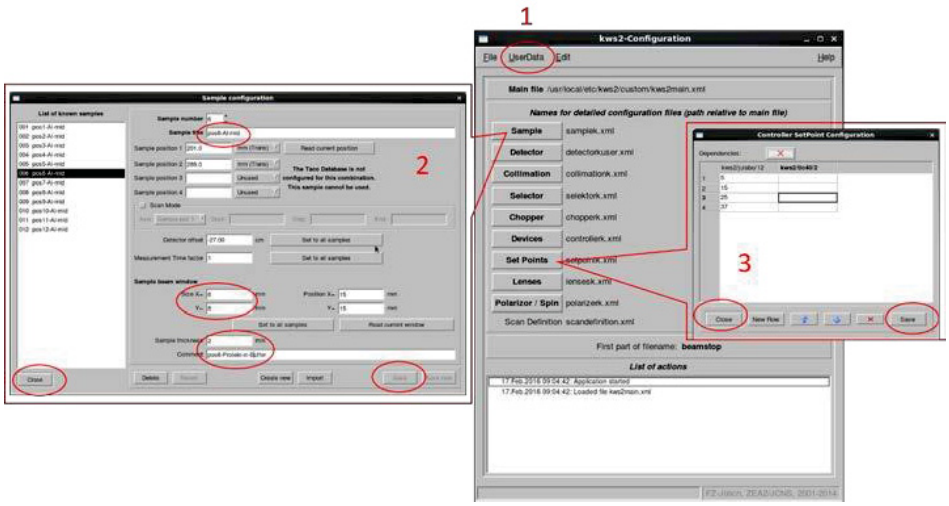

Figure 10: View of the kws2-Configuration menu and Sample configuration functions.

3.2.2.1) Fill the fields **Sample title**, **Sample beam window** – Size, Sample thickness and Comment for each sample/position selected from the left vertical list of the menu (Figure 10). Save each sample configuration.

Note 1: configuration files are predefined for each sample holder and are loaded by the instrument scientist, prior to the start of the experiment; the **Sample position 1, 2, 3, 4** (typically the coordinates x, y, ϕ, ω on the sample stage-rotation table-cradle) and the **Sample beam window – Position** are typically predefined in these files. Note 2: do not use special characters, like _, @, $, etc., in the sample title and comment fields.

3.2.2.2) Leave the menu with Close.

3.2.3) Select **Set Points** (Figure 10) for activating the **Controller SetPoint Configuration** menu.

3.2.3.1) Define the set points (typically, temperature values) for the chosen controller from the table of the activated ones.

Note: when two controllers are connected to the sample holder, the two sets of set-points can be correlated by activating the field **Dependencies**.

3.2.3.2) Save the configuration and leave the menu with Close.

3.2.4) Save all configurations under the **File** function at the upper functions menu.

3.3) Select **Definition** in the main menu (Figure 9) to activate the **kws2 Definition** menu (Figure 11) for defining the experimental setup and the measurement program.

Note: for regular users only the options **Sample, Detector** and **Selection** (in the upper menu functions) are of direct interest.

3.3.2) Select **Sample** and activate the **Select Samples** menu (Figure 11).

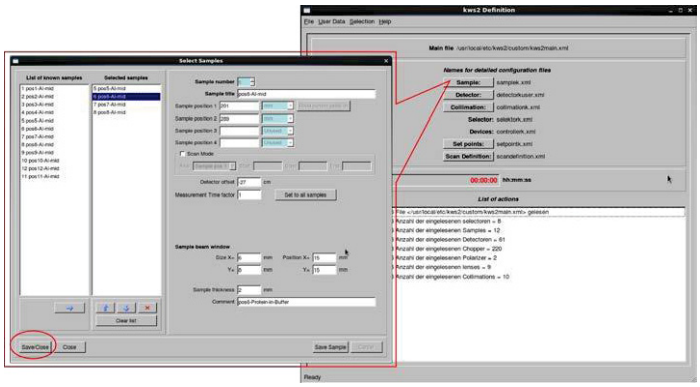

Figure 11: View of the kws2 Definition menu and Select Sample functions.

3.3.2.1) Choose the samples to be measured from the list of known samples in the left vertical field and move them in the Selected Samples field using the blue arrow.

3.3.2.2) Order the list of the selected samples by using the blue vertical arrows.

3.3.2.3.) Check the sample parameters and adjust the name, thickness, and comment, if necessary.

Note: all other parameters on the right half of the menu cannot be changed at this level.

3.3.2.4) Leave the menu with Save/Close

3.3.3) Select **Detector** and activate the **Definition of Measurements** menu (Figure 12).

3.3.3.1) Choose the measurement type (working mode) by selecting in the area **Measurement** either **Standard**, for static measurements, or **Real Time (RT)**, for time resolved measurements.

3.3.3.2) Define in the **Start Trigger** area whether the measurement will be triggered by an external signal or will be started directly, in the case of Real Time (RT) measurement mode.

3.3.3.3) Define the number of time channels and the time length of one channel in the **RT Spectrum** area, in the case of the Real Time (RT) measurement mode. Note: the number of external signals is always 1.

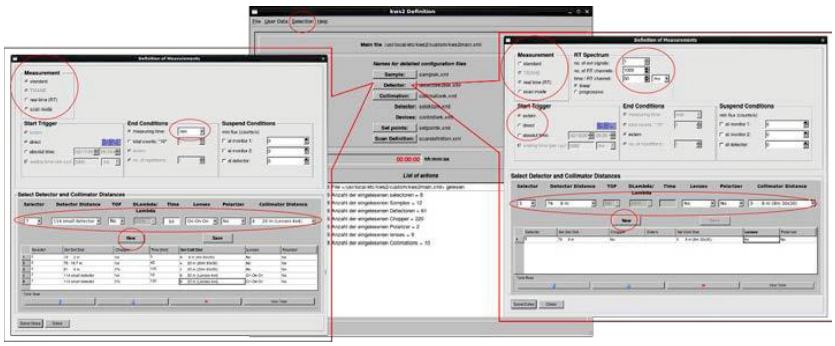

Figure 12: View of the kws2 Definition menu and Definition of Measurements functions.

3.3.3.4) Select the experimental setup/working mode by choosing in the **Select Detector and Collimation Distances** area the appropriate values or answers regarding: wavelength to be used (**Selector** field), detection distance (**Detector Distance** field), data acquisition mode (**TOF** field**)**, aimed wavelength resolution (**DLambda/Lambda** field), measurement time (**Time** field), lenses configuration (**Lenses** field), and collimation distance (**Collimation Distance** field), followed by clicking on **New** after one configuration is entirely defined.

Note1: in the Standard measurement mode, many configurations can be defined and loaded in the lower table by activating the button **New** after each definition (Figure 18). Note 2: for Standard measurement mode, pay attention to select the proper time unit in the field measuring time in the End Conditions area. Note 3: for Real Time (RT) mode, only one measurement can be defined and loaded in the lower table; the total measurement time will be automatically defined, depending on the number of the RT channels and time/RT channel defined. Note 4: time resolved measurements (RT) cannot be used in combination with the TOF mode.

3.3.3.5) Choose **Save/Close** in the **Definition of Measurements** menu after finishing the definition of the experimental setup/working mode.

Note: a table containing the measurement program will be generated by combining the defined samples with the defined measurement conditions (Figure 13).

3.3.3.6) Check the defined measurement program.

3.3.3.6.1) Adjust the measurement time for each measurement as wished and sort the measurements according to the three loops (sorting parameter) shown in the bottom of the menu, for measurements planned without temperature control on the samples; leave the menu with **Save/Close** and return to the **kws2 Definition** menu (Figure 12). Check the total defined measurement time in the central field, marked with red.

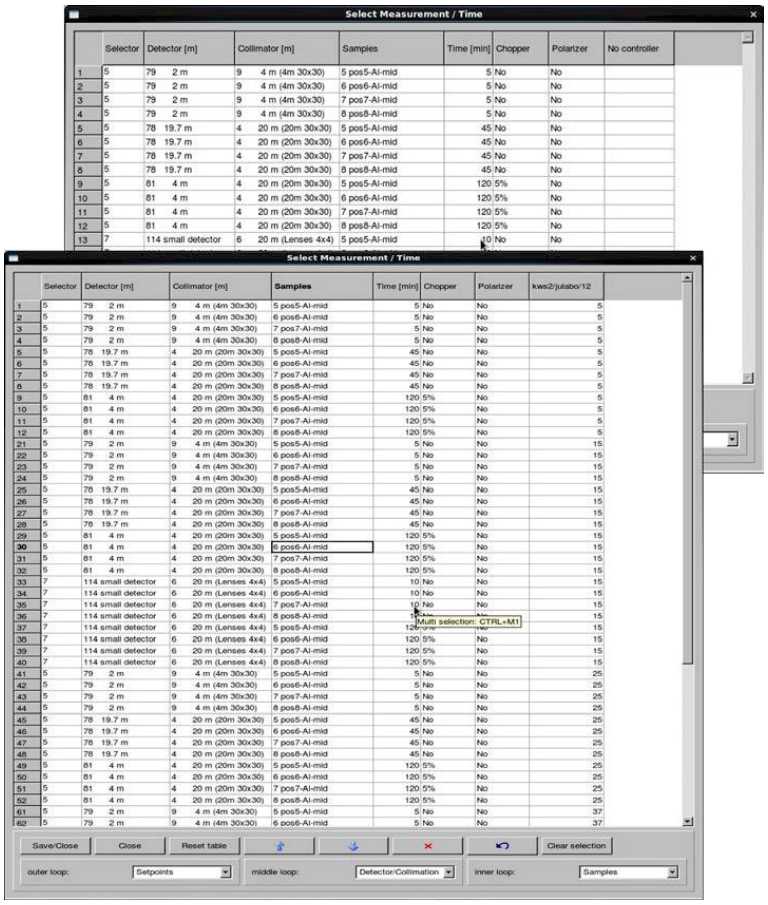

Figure 13: The measurement programs generated by combining the defined samples, defined experimental conditions (back table) and additionally, the defined set points (front table).

3.3.3.6.2) Leave the menu with **Save/Close** without adjusting any parameter or sorting the measurement program for measurements planned with temperature control on the samples. Chose **Selection** (upper functions menu) in the **kws2 Definition** menu and select the proper controller from the list of the activated ones.

Note: a table containing the measurement program will be generated by combining the defined samples with the defined measurement conditions and the defined field values on the sample (temperature, Figure 13). Proceed like for 3.3.3.6.1).

3.4) Close the menu **kws2 Definition** and return to the main menu (Figure 9).

3.5) Select **Control** in the main menu of the **KWS2** measurement software (Figure 9). Note: the Measurement control menu (Figure 14) will be activated.

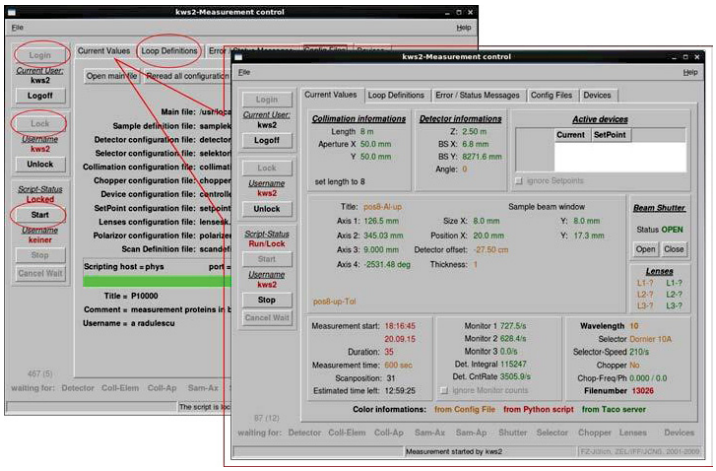

Figure 14: The kws2-Measurement control menu and the Current Values option.

Note: the **KWSlive_MainWindow** interface will be activated (Figure 15).

3.5.1) Log in with the username and password that will be communicated by the instrument scientist and lock the session so that a script is generated, which will execute the commands for performing the uploaded measurement program.

3.5.2) Select **Loop Definition** for checking the uploaded measurement program.

3.5.3) Start the measurement program by activating **Start**.

3.5.4) Select **Current Values** to enable the visualization mode of running measurement.

Note: the parameters and the status of different instrument components/samples/sample environment can be observed, as well as the file number of the running measurement, the

measurement time, the integral intensity on the detector and the count rates of detector and monitors.

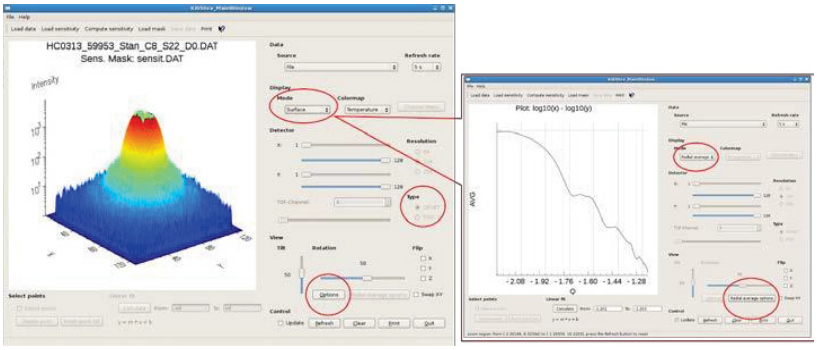

Figure 15: The Live-Display option with the KWSlive_MainWindow menu and different data visualization options.

3.5.5) Let the measurements be conducted and completed according to the defined measurement program or interrupt or stop the measurements by activating **Stop** and choosing the desired option (to continue, to stop the current measurement with/without saving the file or to stop the entire program).

3.6) Select **Live-Display** in the main menu of the **KWS2** measurement software (Figure 9) for the visualization of data for the measurement in progress or from old measurements.

3.6.1) Choose at **Type** either GEDET or PSD for the visualization of data collected with the main or with the secondary (high-resolution) detector, respectively.

3.6.2) Choose at **Display Mode** either **Contour** for the visualization of data in two-dimensional view or **Surface** for the three-dimensional view or **Radial average** for one-dimensional view. Enter parameter values (wavelength and detection distance L_D) in the fields of the menu Radial average options for allowing graphical presentation of data as intensity (uncorrected) vs. Q.

Note: for the visualization of older data choose **Load data** in the upper functions menu and select a file.

3.6.3) Choose a desired **TOF-channel** for the visualization of data collected in TOF mode (with either the main or the secondary detector) or in real-time mode.

Note: for the loaded time-resolved data (current measurement or old files) the TOF-channel functions are activated automatically.

4. Data analysis

4.1) Start the data processing software qtiKWS (command or icon) in a terminal window at the data analysis computer of the KWS-2 instrument.

Note: the interface shown in Figure 16 will be activated.

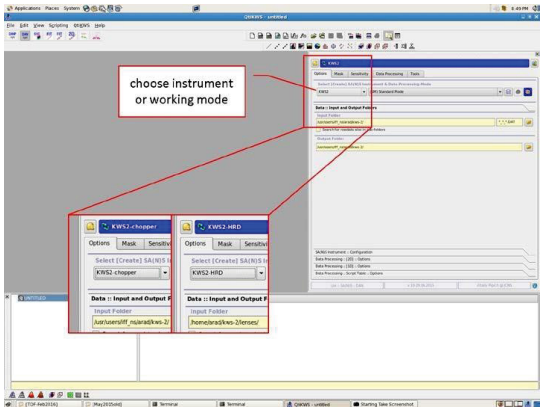

Figure 16: The main interface of the data reduction software with the options for the selection of the instrument and the working mode in which data were collected.

4.2) Select **DAN** from the upper functions menu and select the instrument/working mode from **Options** on the right side menu (as shown in Figure 16). Define the instrument and working mode. Define the folder where the measured data files are located and the corrected data files will be stored.

4.3) Choose **Tools** and **Header(s)** in the right side menu (Figure 17) and generate the info-table containing the files to be processed. Define the table name by acting the left green arrow on the **Header(s)** field. Load the measured files by acting the right green arrow on the **Header(s)** field.

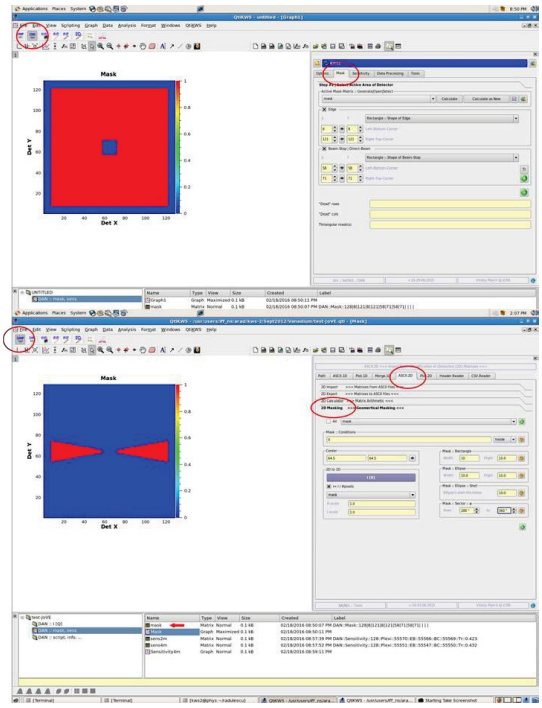

Figure 17: The functions for defining the log-book for the set of data to be treated.

Note 1: a table is generated, which contains all run numbers of the performed measurements and information about the sample names, experimental configurations, measured intensities/count rates, file names and date of measurement for each measured file. Note: for the inspection of the full information the table should be scrolled rightwards. Note 2: all actions done in qtiKWS will produce results that are shown in the explorer-like table in the lower part of the interface.

4.4) Activate **Mask** in the right side menu (Figure 18) and generate the active mask that define the area of the detector which will be considered for data processing.

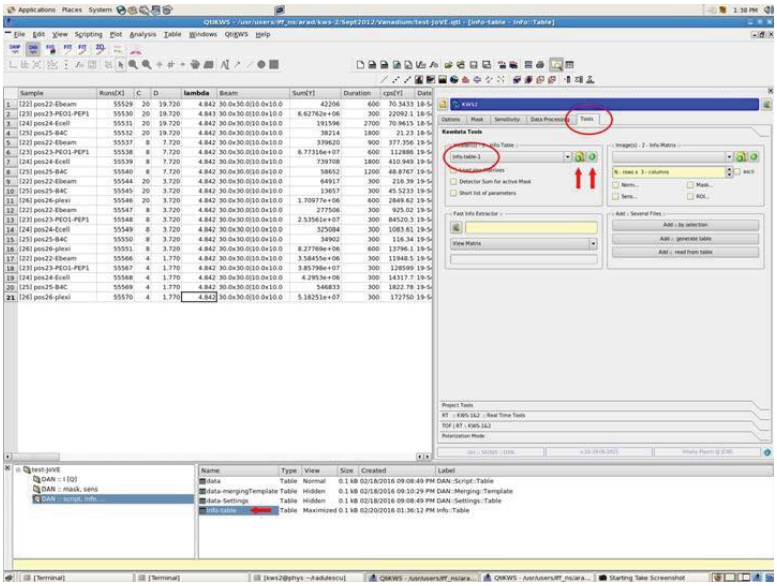

Figure 18: The functions for defining the detector masks for which the data will be treated.

4.4.1) Enter values in the Edge and Beam-Stop fields for defining the left lower and right upper corners of rectangular mask in the case of analysis of isotropic scattering patterns.

Note: the whole detector area excepting the beam-stop (central rectangular masked field) will be used (Figure 18, top).

4.4.2) select **DANP** in the upper functions menu and choose **ASCII.2D** (Figure 18, bottom) for creating a special mask using the drawing functions under the **2D Masking** menu.

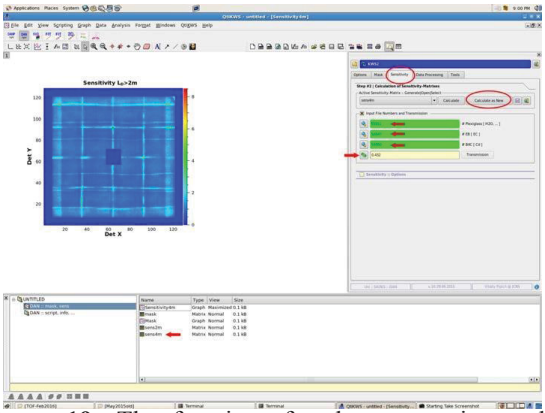

Figure 19: The functions for the preparation and splitting of the real-time (RT) and TOF data collected on multiple time channels, before applying the usual data treatment procedure.

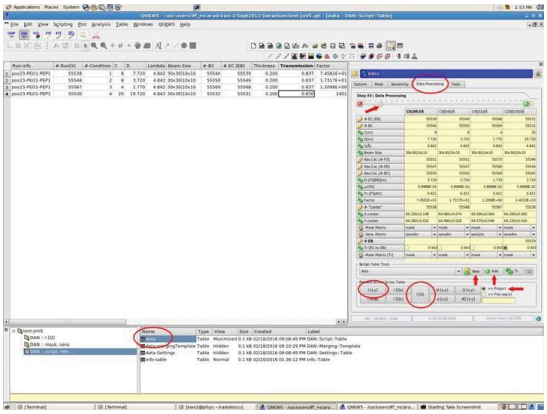

Figure 20: The functions for defining the detector sensitivity maps.

Note1: for anisotropic scattering patterns or localized scattering details, different shape or localized masks (angular sectors, circular or quadratic regions) can be generated. Note2: the new created mask should be renamed in the lower explorer-like table, and a full mask (step 4.4.1) should be additionally generated, as basis for other future modifications.

4.5) Chose **Tools** in the right side menu and activate the **TOF|RT** filed (Figure 19) for performing the splitting of the data collected in real-time (RT) or TOF working modes in single files corresponding to each time channel.

4.5.1) Click on **TOF :: Calculate Parameters** function and load one file from which information about the real-time or TOF conditions are extracted.

4.5.2) Click on **TOF|RT :: Sum vs Number :: Read** function and load the file of interest measured in real-time or TOF modes.

Note: a **sum-tof-file** table like that shown in the left side of the working interface is generated.

4.5.3) Plot the integral intensity as a function of time channels (Figure 19) from the **sum-tof-file** using the graphical options under the **Graph** function in the upper functions menu.

Note: for data measured in TOF mode, the two pulses generated by the chopper are shown in the time configuration of their arrival on the detector.

4.5.4) Define the processing parameters in the fields of **TOF** functions and then click the button **TOF|RT :: All Selected Steps :: Proceed** for conducting the splitting of data in single files corresponding to each time channel.

4.6) Activate **Sensitivity** in the right side menu (Figure 20) and generate the detector sensitivity by entering in the marked green fields the run numbers for the measurements of the standard sample (Plexiglas), empty beam (EB) and blocked beam (B4C). Click on the green arrows next to the yellow filed (Transmission) for calculating the transmission of the standard sample. Generate and name the sensitivity matrix by selecting **Calculate as New**.

Note: different sensitivity maps can be generated for different experimental conditions. The sensitivity map can be visualized by opening the sensitivity matrix in the explorer-like lower table and selecting the appropriate plot functions from the plotting menu that will be activated.

4.7) Activate **Data Processing** in the right side menu (Figure 21) and generate the correction/calibration table and the script table for correcting, calibrating and performing the radial averaging of the data.

4.7.1) Define the number of experimental conditions used in the experiment by using the horizontal slider on the top of the right side menu (red arrow).

4.7.2) Fill the fields indicated by yellow pencil by entering for each experimental condition the run numbers for the empty cell (**EC**), blocked beam (**B4C**), standard sample – Plexiglas (**Abs. Cal. FS**), empty beam for the standard correction (**Abs. Cal. EB**), blocked beam for the standard correction (**Abs. Cal. B4C**), center measurement (**"Center"**), empty beam (**EB**).

4.7.3) Select one of the defined experimental conditions for the calculation of the transmission of samples by checking one of the boxes next to **Tr (Ec-to-EB)** function.

4.7.4) Click on each button indicated by a pair of rotating green arrows on the vertical series of functions (Figure 21) for loading from the defined files the information needed for data processing and calculating the transmission of the empty cell.

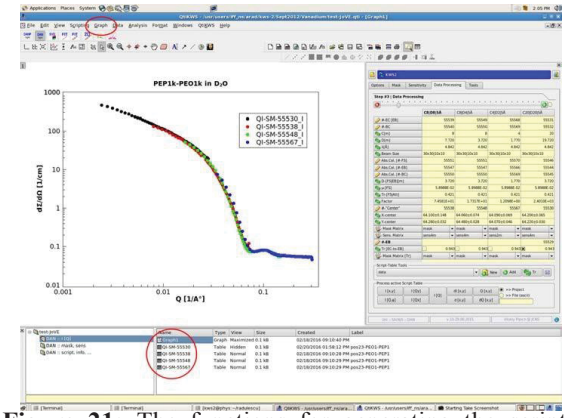

Figure 21: The functions for generating the script table for the correction, calibration and radial averaging of data.

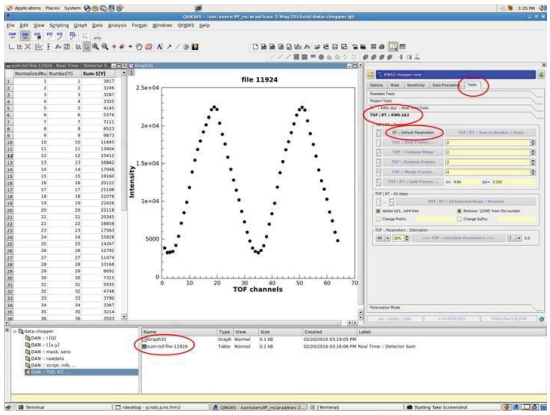

Figure 22: The functions for graphical presentation of treated data.

4.7.5) Click on the head of each yellow column for defining the column name.

4.7.6) Click on the **New** button for generating the table of the data files which will be processed.

4.7.7) Click on the **Add** button for loading the data files which will be processed.

Note: the table shown in the left side of the interface in Figure 20 will be created.

4.7.8) Click on the **Tr** button indicated with rotating green arrow, under the **Script-Table Tools** area, for calculating the transmission of each sample.

4.7.9) Click on the button **I[x,y]** for initiating the correction and calibration of two dimensional data.

4.7.10) Click on the button **I(Q)** for initiating the correction, calibration and radial averaging of data.

Note: by choosing **Project** in the lower right corner of the interface (Figure 21), all results will be generated in the active qtiKWS session (project) and can be visualized in the explorer-like lower table; by choosing **File** in the lower right corner of the interface, all results will be generated as external files, which will be saved in the external folder which was defined at the step 4.2).

4.7.11) Plot the processed data (Figure 22) in the active qtiKWS project by selecting from the lower explorer-like table the generated results and using the graphical options under the **Graph** function in the upper functions menu.

Note: the tables show four columns – Q, I, ΔI, $\Delta\sigma$ of the Q-resolution[5] – for the radially averaged data or two-dimensional matrixes for the data which were not radially averaged.

4.8) Save the qtiKWS project (save functions under the File option of the upper menu)

REPRESENTATIVE RESULTS:

Results of experimental investigations on the structure and morphology of various soft-matter and biophysical samples carried out at KWS-2 in different working modes and experimental setups are given in Figures 23-34. These examples are selected from investigations made on standard samples with known properties, used for the test and commissioning of different working modes or from studies carried out by users at KWS-2 by combining different working modes offered by the instrument.

Figure 23 presents the results obtained on the PEP1k-PEO1k diblock copolymer that forms cylindrical micelles in D_2O, and demonstrates the Q-range that can be covered at KWS-2 in conventional mode by using one wavelength and several detection distances.

For the investigation of larger morphologies, long wavelengths can be involved for measurements at the longest detection distance L_D=20m based on spontaneous decision taken

during the experiment, as demonstrated in Figure 24, where results obtained on a series of polystyrene spheres (standard size) of known size and size polydispersity are shown.

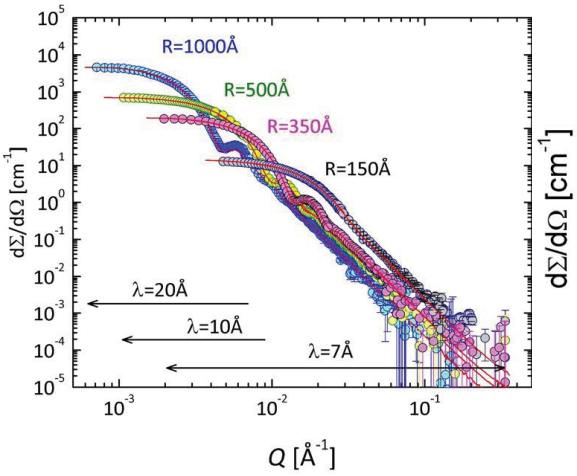

Figure 23: The scattering pattern from PEP1k-PEO1k diblock copolymer micelles in D_2O (after correction for the scattering from solvent was applied) as measured at different detection distances with neutrons of λ=4.5Å; a core-shell rod-like micellar shape is revealed by the Q^{-1} dependence of scattered intensity at low Q and the $Q^{-5/3}$ dependence (blob scattering) observed at high Q; the Q-range covered in each experimental configuration (L_C, L_D) is specifically marked.

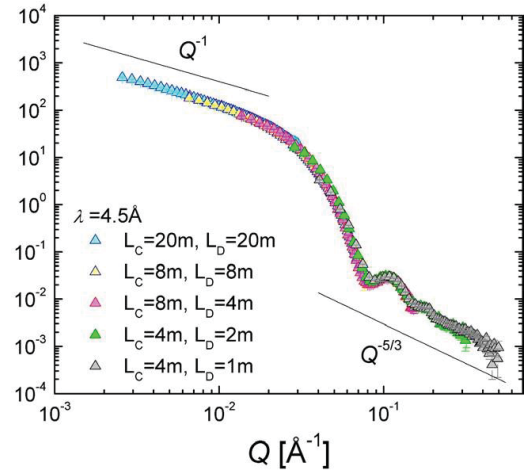

Figure 24: The scattering pattern scattering patterns from polystyrene spherical standards (Thermo Scientific) in D_2O (after correction for the scattering from solvent was applied); the red lines represent fits with the spherical form-factor[9], including the instrument resolution[10, 11] and size polydispersity (supplied by the producer); different neutron wavelengths were involved.

Figure 25 shows the scattering patterns from SiO_2 particles[12] of kwon size and very low size polydispersity in d-DMF, as were measured using two instrumental resolutions. The model fit of the experimental curves[9] using fixed structural parameters and the wavelength resolution as free parameter that matched the aimed value has demonstrated the reliability of the data collected in tunable resolution mode[5].

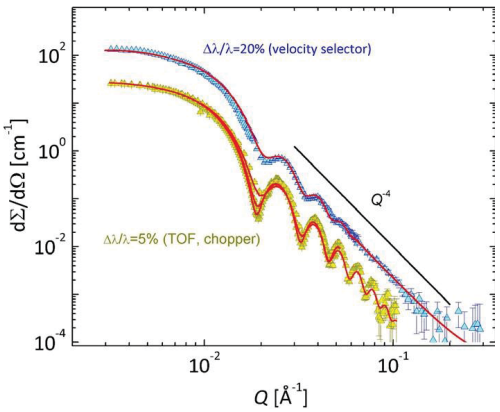

Figure 25: The scattering pattern from SiO_2 particles (low polydispersity in size[9]) in deuterated dymethyl-formamide (d-DMF) measured at KWS-2 with different instrumental resolutions using either the velocity selector (conventional pinhole mode) or the chopper with TOF data acquisition (tunable resolution mode[5]); the red curves represent the model fit of the experimental data with the spherical form factor[9], including the instrumental resolution[10, 11] and the particle size polydispersity; the power-law behavior towards high Q is also indicated.

Figure 26 reveals the direct advantage of combining in the same measurement session the conventional and the tunable $\Delta\lambda/\lambda$ resolution working modes: instead of broad features observable in the scattering pattern from the ordered structure of star-like C28H57-PEO5k polymer micelles in D_2O at high polymer volume fraction (12%) while using the conventional mode with $\Delta\lambda/\lambda$=20%, a fine structure a series of sharper peaks was revealed when better $\Delta\lambda/\lambda$ resolution was involved, which enabled the clear identification of the crystalline phase formed by the micelles in solution[5,13].

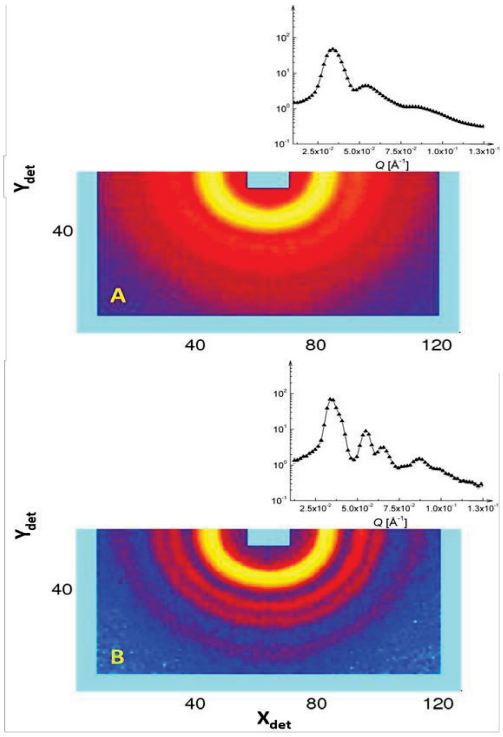

Figure 26: The two-dimensional and radially averaged one-dimensional scattering patterns from the $C_{28}H_{57}$-PEO5k (fully deuterated) polymer micelles in D_2O (at a polymer volume fraction of 12%) measured in conventional mode with $\Delta\lambda/\lambda$ =20% (top) and in tunable resolution mode (chopper) with $\Delta\lambda/\lambda$=5% at L_D=4m (middle) and L_D=8m (bottom); the fine structure of the peak features is better resolved with improved resolution[5, 13].

Figures 27 and 28 demonstrate the advantages of the high intensity mode against the conventional working mode: the results obtained on polystyrene standard samples have proven the gain in intensity (up to 12 times) when larger samples are involved (up to 5cm in diameter) while keeping the same resolution as for conventional pinhole mode. The high-intensity mode with lenses offers advantages in the case of the weak scattering that generally is encountered at large detection distance and is

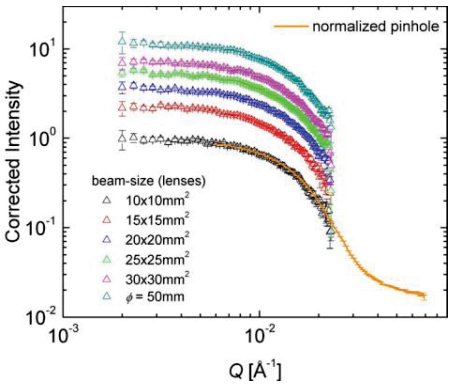

Figure 27: The intensity gain factor of twelve obtained on a sample of polystyrene spheres in D_2O when using lenses compared to the conventional pinhole mode, due to increasing of the sample size (thus, of the beam size); the measurements were carried out with a neutrons of l=7A using all 26 lenses in beam; the cold lenses (70K) have a transmission of 65%.

particularly yielded in the case of weak contrast conditions. When additionally, the sample is stable only over short period of times, the use of this mode represents a clear advantage, as it is demonstrated in Figure 29[14]: bovine serum albumin (BSA) coated citrate capped gold nanoparticles (BSA-GNP) were investigated in salt solutions with the variation of the D_2O content between 0% and 100% D_2O for contrast variation by using the high intensity mode (large sample size) at KWS-2 to overcome the weak scattering from the mineralized GNPs (note that the H_2O scattering level is around $1cm^{-1}$) and the short time stability of the precipitates.

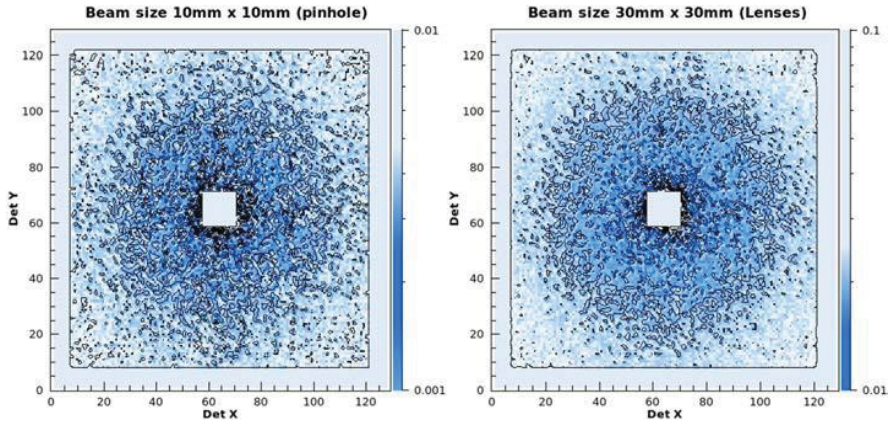

Figure 28: The 2D scattering pattern from polystyrene standard samples in D_2O measured in pinhole mode (left), with the 10mm x 10mm beam size on the sample, and in high-intensity focusing mode (right) with lenses, with the 30mm x 30mm beam size on the sample; the resolution (given by the size of the direct beam, which is captured by the beam-stop in the middle of the detector) is the same in both cases.

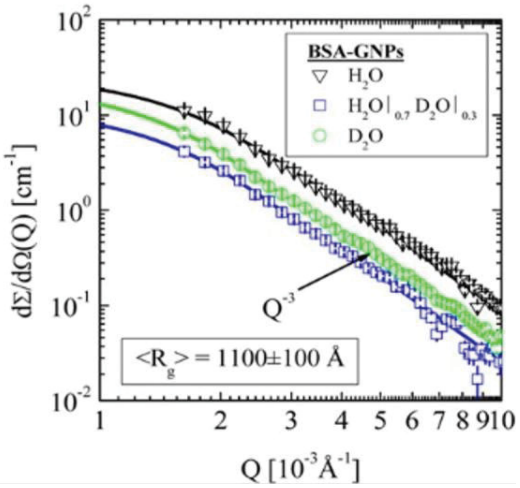

Figure 29: Contrast variation SANS on bovine serum albumin grafted gold nanoparticles (BSA-GNPs) in H_2O, D_2O and mixed H_2O/D_2O solutions using lenses and large samples (5cm in diameter) at KWS-2 (Reprinted with permission from Langmuir, 2014, 30, 15072-15082. Copyright 2014, American Chemical Society).

Figure 30 shows the results obtained on a series of polystyrene spheres (standard size) of known size and size polydispersity and demonstrate the wide *Q*-range that can be covered at KWS-2 when combining the conventional pinhole and the focusing high-resolution (low-*Q*) modes. Large morphologies that show structural levels spanning a wide length scale, from

nanometer to micrometer sizes, can be investigated in a direct way, as shown in Figure 31: the cylindrical core-shell micelles formed by the poly-(hexylene-oxide-co-ethylene-oxide) PHO10k-PEO10k diblock copolymer (fully protonated) in D_2O[15] are characterized by a total thickness of about 300Å and a length of about 7000Å, as revealed by the fit of the experimental results with the core-shell cylindrical form-factor[9, 15].

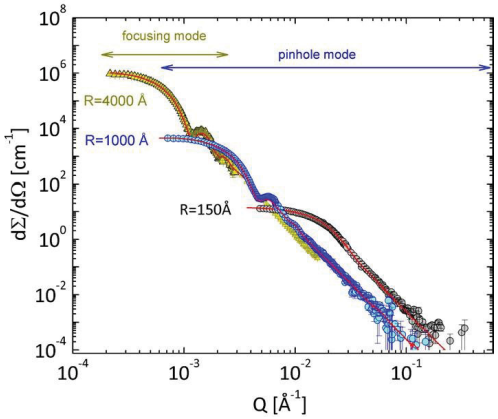

Figure 30: The scattering pattern from polystyrene spherical standards of different sizes (Thermo Scientific) in D_2O (after correction for the scattering from solvent was applied) measured in conventional pinhole mode with neutrons of λ=7Å and 20Å and focusing mode (with 26 lenses) with neutrons of λ=7Å, demonstrating the entire Q-range that can be explored at KWS-2; the red lines represent fits with the spherical form-factor[9], including the instrument resolution[10, 11] and size polydispersity (supplied by the producer).

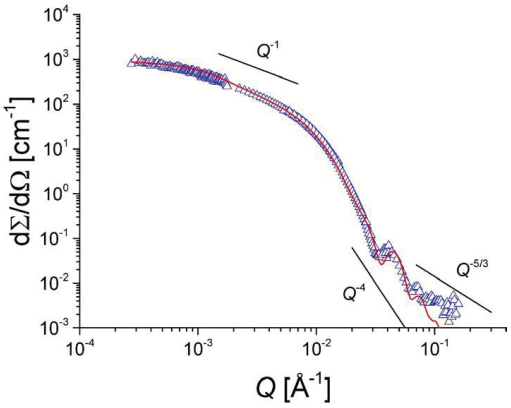

Figure 31: The scattering pattern from fully protonated PHO10k-PEO10k diblock copolymer micelles in D_2O (after correction for the scattering from solvent was applied) as measured at KWS-2 by combining the conventional and the focusing (lenses) modes; a core-shell rod-like micellar shape is revealed by the Q^{-1} dependence of scattered intensity at low Q and the $Q^{-5/3}$ dependence (blob scattering) observed at high Q; the intensity plateau towards low Q values reveals the rods length; the red curve represents the fit of the experimental data with a core-shell cylinder model[9].

At the smaller length scale of a few nanometers the weak scattering signal from small biological molecules in buffer solution can be investigated at KWS-2 benefiting of the high intensity of the instrument. Figure 32 presents the scattering patterns from beta amyloid protein (Aβ 1-42, M_W=4.5 kDa) monomers in deuterated hexafluoroisopropanol dHFIP as obtained after the correction for the scattering signal from the buffer was applied. A model fit of the data delivered a monomer size of about 16±1Å[16]. A long measurement time of several hours for each experimental condition (detection distance L_D and sample type) was involved, although the measurements were carried out at short detection distances. The old detector which has shown limitations regarding the count rate hindered the use of shorter collimation distances L_C, hence of the maximum flux at the instrument. With the commissioning of the

new detection system that enables the use of the full neutron flux, such weak intensities will be measured in the future in shorter times and with improved statistics.

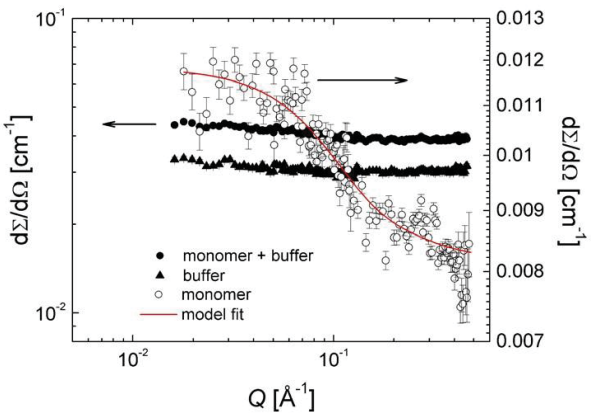

Figure 32: The scattering pattern from beta amyloid protein (Aβ 1-42, M_W=4.5 kDa) monomers in deuterated hexafluoroisopropanol dHFIP at a concentration 5.6 mg/ml, after three weeks incubation measured at detection distance of 5.6 m and 1.1 m; the full symbols present the corrected and calibrated data from the monomer in buffer solution and from the buffer solution, while the open symbols (with the corresponding right vertical scale) denote the scattering signal from monomers, after correction for the buffer contribution was applied; the red solid line shows the fitted Beaucage function with fixed dimensionality d=2[16] .

Figure 33 presents the time-dependent changes in integrated lamellar reflection intensity during the guest exchange between deuterated and protonated benzene in a syndiotactic-polystyrene (sPS) co-crystal with benzene[17] as measured at KWS-2 in real-time (RT) mode with a time step of 1s. The diffusion of a guest molecule in the crystalline regions (lamellae) of sPS could be investigated at early stages based on the evolution of the intensity due to the change of contrast induced by the diffusing guest. The initiation and control of the guest diffusion was accomplished using a "guest-exchange" device[17], which enabled the external triggering of detection electronics once a guest exchange process in the sample was initiated. The start of the data acquisition was synchronized in this way with the start of the change of sample scattering properties induced by the new guest molecules.

Figure 34 presents the SANS patterns from Lysozyme protein in D_2O buffer and from the D_2O buffer collected at different pressures. A special attention has been paid for the investigation of the background and forward scattering from the Lysozyme molecules, used as test for the performance of the new pressure cell manufactured in house by following a design done in PSI, Switzerland. The results were similar to those obtained in by Kohlbrecher et al. in a similar study for the test of the original pressure cell model constructed there[18, 19]. At KWS-2 further data have been acquired since a pressure of 5000 bar has been reached. Evolution of the forward scattered intensity from the protein follows a linear behavior as obtained in the study at PSI, Switzerland[19].

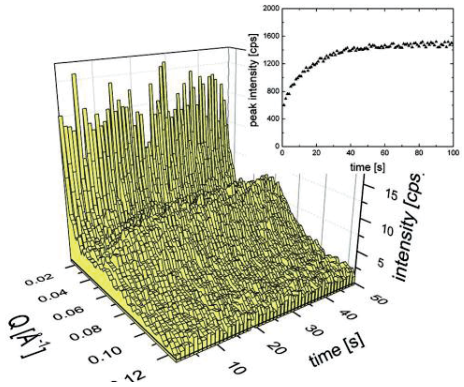

Figure 33: The time dependence of the integrated lamellar reflection intensity measured in real time SANS experiment at KWS-2 on the exchange process between deuterated benzene and protonated benzene molecules in a syndiotactic polystyrene (sPS) co-crystal with benzene guest molecules; the use of uniaxially oriented sPS films enabled observation of the intensity evolution from oriented lamellar stacks due to fast contrast exchange[17] on particular sectors of the detector in a reliable way.

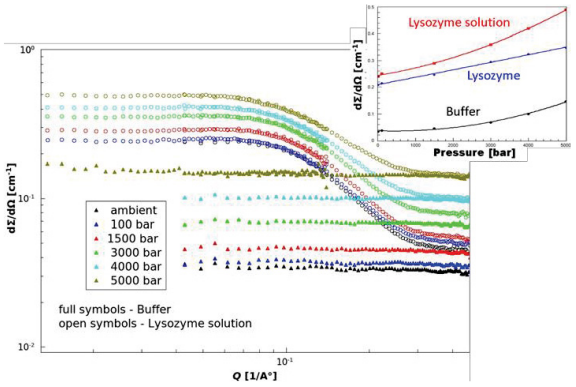

Figure 34: Scattering patterns from lysozyme 50 mg/mL in 50 mM acetate buffer in D_2O and from buffer solution measured on KWS-2 from ambient pressure up to 5000 bar. The inset shows the behaviour of the forward scattered intensity I($Q \rightarrow 0$) from the protein solution, buffer and protein (after correction for the buffer contribution was applied) as a function of pressure.

DISCUSSION:

Soft matter and biophysical systems are characterized typically by structural correlations and interrelated microstructural and morphological levels that span a wide length scale, from nm up to microns. For the understanding of the mechanism of morphology formation and evolution and the relationship between the microscopic features and macroscopic properties of such systems, it is important to explore their microstructure over the entire length scale and under relevant environmental conditions (temperature, pressure, pH, humidity, etc.).

KWS-2 SANS diffractometer offers the high versatility and performance required by such structural studies via the combination of optimized experimental parameters such as intensity, length scale, space resolution or time resolution and complex sample environments. Using the multiple working modes enumerated in the Introduction and supported by the results presented in Figures 23-34, KWS-2 is pushing the performance beyond the conventional limits set at a classical SANS diffractometer at a steady neutron source (reactor) in an easy and practical manner, which permits optimization, flexibility and spontaneity in designing and conducting complex studies, as supported by the described protocol. Practically, at KWS-2 combined SANS and USANS investigations can be carried out, with the advantage that the sample

geometry and thermodynamic conditions remain constant, so that certain sensitive effects can be unambiguously explored, unlike the classical approach of involving two or more different instruments and sample geometries. Also, strong correlate systems and periodicities can be studied with adapted resolution, without spending time and efforts with the installation of complicate monochromatization systems, which would involve additional care and safety aspects. The hindrances generated by the weak scattering due to use of highly diluted systems or unfavorable contrast conditions can be overcome by the use of higher intensities based on larger beam size while keeping the resolution. These advantages combined with specialization of the instrument on particular research fields, related to soft-matter and biophysical systems, compensate for the inherent intensity and Q-range limitations which conventional SANS diffractometers show in comparison to the newly established TOF-SANS diffractometers at spallation sources. In spite of an ideal higher performance, the latter still present an increased degree of difficulty with respect to conducting the experiments by the regular users and especially to handling the data reduction. For increased flexibility and easiness the TOF-SANS instruments often rely on imposing boundaries, with consequences in limiting the performance.

KWS-2 targets the study of structure and structural changes mostly in systems from soft condensed matter, chemistry and biology. As typical applications can be enumerated: polymers, polymer solutions, polymer melts, polymer blends, colloids, nanocomposites, micellar systems, microemulsions, membranes, films, in-situ adsorption-desorption or humidifying-drying phenomena, kinetics of de-mixing, formation, aggregation of structures, shear induced deformations, rubber networks, protein structures, protein folding/unfolding processes, in-situ crystallization phenomena, hierarchical and multiple size semi-crystalline polymer morphologies. KWS-2 shows limitations in possibility to support detailed structural studies on magnetic systems or in classical hard-matter or materials fields using non-polarized or polarized neutrons and specific low-temperature and high magnetic field sample environments. A near future development of KWS-2 aims to implement and optimize a new working mode with polarized neutrons and polarization analysis21 that will enable the possibility for the separation of the structural relevant coherent scattering signals from the incoherent scattering background, which will bring an unique advantage for the unambiguous characterization of small weak scattering biological systems.

The Protocol describes how SANS investigations with varying degrees of complexity can be typically planned, programed, conducted and visualized at KWS-2 and how the data can be reduced. In a SANS experiment the sample's differential scattering cross section, dΣ/dΩ, is evaluated in absolute units of cm^{-1} typically over a wide *Q*-range that correspond to a broad length scale over which structural correlations and interrelated size levels characteristic of the investigated system appear. The scattering cross section dΣ/dΩ is thus the physical quantity relating the intensity measured in a static scattering experiment at an angle θ, $I_s=f(\theta)$, to the structural properties of the sample.

For the evaluation of dΣ/dΩ for a system of interest, besides the measurement of the system, additional measurements are needed, in order to correct the data for any external scattering (environment, sample cell, solvent or buffer solution in case of solute systems, etc.) and calibrate the corrected data in absolute units[8]. The external background (sample cell or container), the reference sample (solvent or buffer solutions), the sample transmission (needed for a correct background subtraction and calibration of the corrected results in absolute units), the electronic background of the detector, the detector sensitivity (inhomogeneity of detector efficiency that are inherent for area detectors) and a normalized standard sample should be additionally measured. At KWS-2 a Plexiglas (PMMA) is used as standard sample. This is a so-called secondary standard and is periodically calibrated against a primary standard sample, which is vanadium. Vanadium delivers a very weak scattered intensity and requires very long measurement times for collecting appropriate statistics, therefore is unpractical for SANS purposes. The intensity collected from the sample of interest I_S and from the standard sample I_{St} can be expressed as follows

$$I_S(counts, \theta, Q) = I_0 t_S A_S T_S \Delta\Psi_S (d\,\Sigma/d\,\Omega)_S \quad [1]$$

$$I_{St}(counts, \theta, Q) = I_0 t_{St} A_{St} T_{St} \Delta\Psi_{St} (d\,\Sigma/d\,\Omega)_{St} \quad [2]$$

where I_0 represents the incoming intensity (delivered by the collimation system), t – the thickness, A – the area exposed to the beam, T – the transmission, and $\Delta\Psi$ is the solid angle in which a detection cell is seen from the sample position. If both sample and standard are measured in the same conditions with respect to the incoming beam (L_C, A_C and A_S, λ and $\Delta\lambda/\lambda$), thus same I_0 and A, and the solid angle is expressed as A_D/L_D (with A_D – the area of a

detection cell), by dividing the two relations the scattering cross-section of the sample is obtained as

$$\left(\frac{d\Sigma}{d\Omega}\right)_S = \frac{t_{St}T_{St}(d\Sigma/d\Omega)_{St}}{t_S T_S}\frac{\left(L_D^S\right)^2}{\left(L_D^{St}\right)^2}\frac{((I_{S+Cell}-I_B)-T_S(I_{ECell}-I_B))}{\langle I_{St}\rangle} = k\frac{((I_{S+Cell}-I_B)-T_S(I_{ECell}-I_B))}{T_S\langle I_{St}\rangle} \quad [3]$$

where the I_{St} is expressed as an average (the standard as an incoherent scattering system delivers a flat scattering pattern) and the I_S is obtained after correcting the measured intensity of the sample in the cell (container) for the contribution of the empty cell I_{ECell} and the background on the detector for the closed beam, I_B. The product $t_{St}T_{St}(d\,\Sigma/d\,\Omega)_{St}$, which contains scattering and physical parameters of the standard sample, depends on the neutron wavelength λ and is typically known from the calibration of the standard sample. Thus, it is tabulated in the data reduction software[4]. The parameters and quantities in Eq.3 that are known from calibration procedures and the definition of the experimental setup (t_S, L_D) form the so-called calibration factor k. The intensities and the sample transmission T_S that appear in Eq. 3 must be measured.

The data analysis program qtiKWS does the correction, calibration and radial averaging of the experimental data and delivers $d\,\Sigma/d\,\Omega$ for the investigated samples, which will be further the subject of modeling and fitting procedures according to structural and morphological models.

ACKNOWLEDGMENTS:

We acknowledge Dr. Dietmar Schwahn (Forschungszentrum Jülich GmbH) for support and stimulating discussions regarding the upgrades operated at KWS-2 in 2010-2015. The constant help from the Central Institute of Engineering, Electronics and Analytics (ZEA) and JCNS-1 (Neutron Scattering) and JCNS-2 (Scattering Methods) Institutes in Forschungszentrum Jülich GmbH during the design, installation and commissioning of components, devices and control software for the new working modes at KWS-2 is gratefully acknowledged.

DISCLOSURES:

The authors have nothing to disclose.

REFERENCES

1. Gläser, W. & Petry, W. The new neutron source FRM II. *Physica* B **276-278**, 30-32, doi: 10.1016/S0921-4526(99)01460-X (2000).

2. Radulescu, A., Pipich, V. & Ioffe, A. Quality assessment of neutron delivery system for small-angle neutron scattering diffractometers of the Jülich Centre for Neutron Science at FRM II. *Nucl. Instrum. Methods Phys. Res. Sect*. A **689**, 1-6, doi:10.1016/j.nima.2012.06.027 (2012).

3. Radulescu, A. & Ioffe, A. Neutron guide system for small-angle neutron scattering instruments of the Jülich Centre for Neutron Science at FRM-II. *Nucl. Instrum. Methods Phys. Res. Sect*. A **586**, 55-58, doi:10.1016/j.nima.2007.11.039 (2008)

4. Radulescu, A., Pipich, V., Frielinghaus, H. & Appavou, M. S. KWS-2, the high intensity / wide Q-range small angle neutron diffractometer for soft-matter and biology at FRM II. *J. Phys.: Conf. Ser.* **351**, 012026, doi:10.1088/1742-6596/351/1/012026 (2012).

5. Radulescu, A., et al. Tuning the instrument resolution using chopper and time of flight at the small-angle neutron scattering diffractometer KWS-2. *J.Appl.Cryst.* **48**, 1849-1859, doi: 10.1107/S1600576715019019 (2015).

6. Frielinghaus, H., et al. Aspherical refractive lenses for small-angle neutron scattering. *J. Appl. Cryst.* **42**, 681-690, doi: 10.1107/S00218898090179 (2009).

7. Radulescu, A., Fetters, L.J. & Richter, D. Structural characterization of semicrystalline polymer morphologies by imaging-SANS. *J.Phys.: Conf.Ser.* **340**, 012089, doi:10.1088/1742-6596/340/1/012089 (2012).

8. Zemb, T. & Lindner, P. Neutron, X-rays and Light Scattering Methods Applied to Soft Condensed Matter. Elsevier Science 552 (2002).

9. Pedersen, J. S. Analysis of small-angle scattering data from colloids and polymer solutions: modeling and least square fittings. *Adv. Colloid Interface Sci*. **70**, 171-210, doi: 10.1016/S0001-8686(97)00312-6 (1997).

10. Barker, J. G. & Pedersen, J. S. Instrumental Smearing Effects in Radially Symmetric Small-Angle Neutron Scattering by Numerical and Analytical Methods. *J. Appl. Cryst*. **28**, 105–114, doi: 10.1107/S0021889894010095 (1995).

11. Hammouda, B. & Mildner, D. F. R. Small-angle neutron scattering resolution with refractive optics. *J. Appl. Cryst.* **40**, 250-259, doi: 10.1107/S002188980605638X (2007).

12. Vad, T., Sager, W. F. C., Zhang, J., Buitenhuis, J. & Radulescu, A. Experimental determination of resolution function parameters from small-angle neutron scattering data of a colloidal SiO_2 dispersion. *J. Appl. Cryst*. **43**, 686-692, doi: 10.1107/S0021889810022156 (2010).

13. Amann, M., Willner, L., Stellbrink, J., Radulescu, A., Richter, D. Studying the concentration dependence of the aggregation number of a micellar model system by SANS. *Soft Matter* **11**, 4208-4217, doi: 10.1039/C5SM00469A (2015).

14. Dahdal, Y. N., et al. Small-Angle Neutron Scattering Studies of Mineralization on BSA Coated Citrate Capped Gold Nanoparticles Used as a Model Surface for Membrane Scaling in RO Wastewater Desalination. *Langmuir*, **30**, 15072-14082, doi: 10.1021/la502706k (2014).

15. Ströbl, M., Diploma Thesis, Univ. Regensburg, Germany (2008).

16. Zhang-Haagen, B., et al. Monomeric Amyloid Beta Peptide in Hexafluoroisopropanol Detected by Small Angle Neutron Scattering. *PLOS One,* **11**, e0150267, doi: 10.1371/journal.pone.0150267 (2016).

17. Kaneko, F., Radulescu, A. & Ute, K. Time-resolved small-angle neutron scattering on guest-exchange processes in co-crystals of syndiotactic polystyrene. *J. Appl. Cryst.* **47**, 6-13, doi: 10.1107/S1600576713030343 (2014).

18. Kohlbrecher, J., et al. A high pressure cell for small angle neutron scattering up to 5000 MPa in combination with light scattering to investigate liquid samples. *Rev. Sci. Instr*. **78**, 125101, doi: 10.1063/1.2817632 (2007).

19. Vavrin, R., et al. Structure and phase diagram of an adhesive colloidal dispersion under high pressure: A small angle neutron scattering, diffuse wave spectroscopy, and light scattering. *J. Chem. Phys*. **130**, 154903, doi: 10.1063/1.3103245 (2009).

20. Kaneko, F., et al. Development of a Simultaneous SANS/FTIR Measuring System. *Chem. Lett*. **44**, 497-499, doi: 10.1246/cl.141179 (2015).

21. Babcock, E. et al. Polarization analysis with ^{3}He spin filters for separating coherent from incoherent scattering in soft matter studies. *Phys. Procedia* **42**, 154-162, doi: 10.1016/j.phpro.2013.03.190 (2013).

2.4 Experimental evidence for an Aβ pentamer/hexamer in solution

M. Wolff[1,2,#], B. Zhang-Haagen[2,3,#], C. Decker[1], B. Barz[2], M. Schneider[1], R. Biehl[3,4], A. Radulescu[4], B. Strodel[2], D. Willbold[1,2], and L. Nagel-Steger[1,2,*]

Status: submitted in Nature Communications

Impact Factor: 11.47

Proportion of contribution 30%

Contributions: Conceived and designed the SANS experiments; performed the SANS experiments; Analyzed the data.

Aβ42 pentamers to hexamers are the smallest detectable aggregate species in solution.

Martin Wolff[1,2,†] *, Bo Zhang-Haagen*[2,3] *, Christina Decker*[1]*, Bogdan Barz*[2]*, Mario Schneider*[1]*, Ralf Biehl*[3,4]*, Aurel Radulescu*[4]*, Birgit Strodel*[2]*, Dieter Willbold*[1,2]*, and Luitgard Nagel-Steger*[1,2]*,*

[1] Institut für Physikalische Biologie, Heinrich-Heine-Universität Düsseldorf, 40225 Düsseldorf, Germany

[2] Institute of Complex Systems, Structural Biochemistry (ICS-6), Research Centre Jülich, 52428 Jülich, Germany

[3] Jülich Centre for Neutron Science & Institute of Complex Systems, Neutron Scattering (JCNS-1&ICS-1), Research Centre Jülich, 52428 Jülich, Germany,

[4] Jülich Centre for Neutron Science, Outstation at MLZ (JCNS-MLZ), Research Centre Jülich, 85747 Garching, Germany

ABSTRACT: Aβ oligomers play a decisive role in Alzheimer's disease pathology. However, their structural properties are not well understood. We used sedimentation velocity centrifugation, small angle neutron scattering and molecular modelling to identify the small oligomeric species formed by Aβ42 peptide in solution. It is characterized by a sedimentation coefficient of 2.56 S and a radius of gyration between 2 and 4 nm. This experimentally determined sedimentation coefficient is in close agreement with the one calculated for an Aβ42 hexamer based on MD simulations in the μs range. To our knowledge it is for the first time that an Aβ42 oligomeric species has been detected by SANS measurements. Our results demonstrate that the smallest detectable species in solution are penta- to hexamers. No evidence could be found for the presence of dimers, trimers or tetramers, which have been frequently reported as early assembly states of Aβ42.

An increasing number of human diseases are characterized by the accumulation of specific protein aggregates found in proteinaceous depositions with a common tertiary structural motif, characterized by a cross-β-sheet architecture, called amyloid fold.[1] While these amyloid fibril folds are already clarified for a number of proteins, for review see ref.[2], little is known about the first stages of the amyloid formation process, where dynamic, heterogeneous and often toxic intermediates are most likely populated. Such oligomeric species are elusive with respect to high-resolution structural characterizations either because of too low concentrations or due to their kinetic instability.[3-6] The accumulation of aggregated Aβ peptide in the brain tissue is one of the key hallmarks in Alzheimer's disease (AD),[7] which is the most common form of dementia worldwide. Aβ is generated as a proteolytic fragment from the transmembrane amyloid precursor protein (APP). Among a number of isoforms, caused by variations in the location of the N- or C-terminus or post-transcriptional modifications, the 42 amino acids long isoform is the main constituent of extracellular senile plaques found post mortem in AD brains.[8] However, not the deposited fibrillar forms, but rather soluble Aβ oligomers have been found responsible for the neurodegeneration in AD.[9,10] The smallest Aβ assemblies discussed in literature are dimers, which have been found in body fluids and brain tissues from AD patients.[11,12] Several reports of in vitro as well as in vivo experiments point to the existence of a monomer-dimer equilibrium for Aβ.[13,14] In experiments of photo-induced cross-linking of unmodified proteins (PICUP) applied to Aβ peptides covalently linked dimers are detectable for Aβ40 and for Aβ42 among larger oligomeric species.[15] But also non-cross-linked Aβ oligomers have already been identified in polyacrylamide gel electrophoresis as SDS-resistant bands and interpreted as dimers to tetramers.[16] Cultured neuronal cells were found to release small Aβ oligomers, among which the dimer represents a major species, whose size was determined by SDS-PAGE combined with

western blotting.[17-19] Furthermore, dimers have been found along with monomers and trimers as stable components in neuritic plaques obtained from AD brain.[20] Other studies have identified Aβ paranuclei as penta- or hexamers, which were detected by mass spectrometry based techniques.[21,22] Recently a group succeeded in the characterization of an enriched Aβ42 oligomer by NMR combined with AFM.[23] Further information on Aβ oligomers can be found in a number of recently published reviews.[4,6,24-28]

Sedimentation velocity (SV) centrifugation is an attractive complementary technique for the sensitive detection and quantification of protein aggregates.[29] Even less than one percent aggregates in a sample can be reliably detected, provided instrument and equipment are handled with sufficient care.[30] Recently, we demonstrated the existence of discrete oligomeric species in the *s*-value range from 4 to 15 S during the lag phase of fibril formation by SV centrifugation.[31] Analysis reproducibly yielded two Aβ42 assembly species at low salt conditions and physiological pH, independent of the total Aβ42 concentration; one species corresponded to a 12-mer and the other to an 18-mer of Aβ42. Their sizes suggest the involvement of a trimeric or hexameric building block. We interpreted the recently observed gap in the determined *s*-value distributions between 0.69 S, corresponding to the Aβ42 monomer, and 4 S as the range for the nucleus size.[31] In this s-value region corresponding to molecular weights between 5 kDa and 55 kDa, we suspect further reaction intermediates on-pathway to fibrils. Here, we aim to close this gap by combining two complementary techniques for the structural characterization of macromolecules in solution, i.e. SV analysis and small angle neutron scattering (SANS), which will provide us with important information about the first steps of the nucleation process. In addition, we complement our experimental results by molecular dynamics (MD) simulations of

oligomeric Aβ42 assemblies, which bridge our SV and SANS results. This combined approach reveals clear experimental evidence for a penta- or hexameric assembly of Aβ42 in solution.

RESULTS

The focus of this study is on the determination of the aggregation states of Aβ42 in solution in order to elucidate the initial Aβ42 assembly steps. Recently it has been shown that SV analysis is a highly sensitive detection method for spurious amounts of aggregates in protein samples. SV analysis allows for the determination of size- and shape distributions for self-assembling proteins with high accuracy.[32-34] Due to the fractionating property of the sedimentation process with large particles sedimenting before small particles, the method is resistant to the presence of large particles, such as unresolved protein aggregates or dust particles. The method is characterized by an excellent signal to noise ratio. The shape evolution of the formed sedimentation boundary over time reveals not only information about the sedimentation velocity but also about the diffusion properties of the analytes. Importantly, the method requires no interactions of the peptide with surfaces that might induce aggregation. SANS is a well-established, non-destructive method to examine structure on length scales of 1 to 1000 nm. In a previous study we could demonstrate the applicability of SANS with regard to monomeric Aβ42.[35] While in SV the hydrodynamic properties of macromolecules are evaluated, yielding the hydrodynamic radius, in SANS the properties of macromolecules as neutron scatterers are evaluated yielding aside from information about size, shape and interactions the radius of gyration.

Sedimentation velocity centrifugation allows sensitive detection of Aβ aggregates in solution. Looking for small assemblies of Aβ it was straightforward to check for the detectability of a dimeric assembly, first. As a model a stable synthetic Aβ40 dimer was

generated from a monomer with a cysteine residue at position 0, which formed an intermolecular disulphide bridge under oxidizing conditions. SV analysis revealed that the Aβ42 monomer and the covalently linked dimer are sufficiently different so that they can be detected as different *s*-value species: 0.65 S and 0.9 S, respectively. Experimental measurements had been complemented by simulations (Fig. S1). None of the SV experiments performed for Aβ42 provided evidence for an Aβ42 dimer in solution. Additionally, superposition of $c(s)$ derived peaks for the monomer revealed no concentration dependent shift or broadening of the signal at 0.62 S within the covered concentration range for absorbance detection, which is also a strong indicator for the absence of a monomer-dimer equilibrium.[36,37] We thus conclude that the dimer fraction is below the detection limit, i.e. below 0.5 % of the signal.

The smallest detectable assembly state is a penta- to hexamer. Experimental evidence for oligomeric species between a trimer and 12-mer are found mainly from SDS-PAGE analyses and mass spectrometry studies. For example, a trimer is postulated as building block for the Aβ*56 aggregate, found in *in-vivo* studies by Lesné and colleagues,[38,39] and trimers along with tetramers were also detected by Bernstein.[40] We decreased the total Aβ42 concentrations to the low micro- to nanomolar concentration range in our SV experiments, because we expect that at Aβ42 concentrations, which are below the critical concentration for the formation of higher-order structures, the drain of small oligomers into larger assemblies is suppressed. The necessary increase in detection sensitivity was gained by using analytical ultracentrifugation (AUC) coupled with a fluorescence detection system. Thus, a lower limit of about 100 nM fluorophore-labelled Aβ42 was achieved. For the position of the fluorescence label we chose the N-terminus of Aβ, because the N-terminus is not primarily involved in intermolecular contacts required for aggregate formation.[41]

SV analysis is a technique, which recently gained special relevance in the determination of aggregate concentration in samples of pharmaceutical relevant proteins.[42-45] According to literature this method allows for the detection of spurious amounts of aggregates provided it is applied with due diligence. According to theoretically considerations the high signal to noise ratios of the absorbance and fluorescence detection in sedimentation velocity experiments provides a superior sensitivity for trace components well below 1 %.[45] In practical studies on a dimeric antibody 0.2 % as limit of detection and about 2.8 % as limit of quantification had been determined.[30] For confirmation of the detected high molecular weight species the calculation of the continuous $c(s)$ distribution, which provides the relative amounts of the differently sedimenting species in a given sample, was extended by applying a Bayesian approach followed by F statistics, as reported recently by Wafer and colleagues.[42]

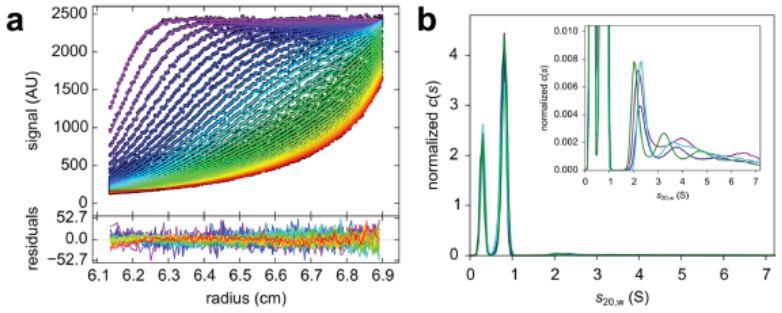

Figure 1. SV analysis of 0.1 µM AF488-Aβ42 with fluorescence detection reveals the existence of small oligomers in addition to the monomer. (**a**) Raw data of an SV experiment with overlaid lines for the fitted data, showing a signal intensity of about 2500 RFU. Only every third scan, as well as every third data point is shown for clarity. The corresponding residuals within the fitted data range are shown in the box below. Rmsd for this sample was 11.86. (**b**) Area normalized *c*(*s*) results for four independent samples of 0.1 µM AF488-Aβ42 have been superimposed in the graph. The 0.8 S species is assigned to the monomer, the peak at 0.3 S is the

result of incomplete removal of unincorporated dye. The inset shows the magnification of $c(s)$ distributions. Sedimentation was performed at 60,000 rpm, 20°C.

The total Aβ42 concentration, c_0 was varied from 0.1 μM to 160 μM. All SV measurements were performed with Aβ42 incubation times of about two hours before SV centrifugation. The *s*-value for the monomeric AF488-Aβ42 was determined as 0.80±0.01 S, which is slightly higher than the *s*-value found for the unlabelled monomer (Table 1). The monomer accounts for 61 % of the total fluorescence signal. The *s*-values of the smallest detectable oligomers in this experiment were determined as 2.32±0.14 S for AF488-Aβ42 and 2.56±0.32 S for Aβ42. The smaller *s*-value for AF488-Aβ42 oligomer in comparison to the unlabelled Aβ42 oligomer is due to an increase of the frictional coefficient f or shape factor f/f_0 for AF488-Aβ42 with the fluorophores protruding away from the oligomer. For the monomer, which is unstructured in aqueous solution,[31] the increase in mass seems to be the dominating effect leading to an increase of the *s*-value for AF488-Aβ42. In Fig. 1B the $c(s)$ distributions for four independent samples of 0.1 μM AF488-Aβ42 dissolved in 10 mM phosphate buffer are shown. At this low concentration aside from the monomer and the residual free dye only a small fraction of small oligomeric species were detected. These oligomers are dominated by a species between 2 S and 3 S, which represents the smallest *s*-value of the oligomer distribution. The fraction of this species accounts for about 1.4 % of the total signal. After subtracting the contribution of the free dye the value increases to 2 % of total AF488-Aβ42. To further test the properties of the small oligomer we performed SV experiments at different temperatures between 10 and 30°C. Variation of the experimental temperature did not lead to significant changes in the oligomeric fraction within this temperature range. To exclude the possibility of contamination or covalently bonded

aggregate species, we treated the sample with 6 M guanidine hydrochloride. Under these denaturing conditions this oligomer species disappeared (data not shown). As a further control, the fluorescently labelled Aβ-peptide had been chromatographically purified by size exclusion chromatography and only the monomer peak was applied to SV measurements, yielding again the oligomeric species thus indicating the presence of a chemical equilibrium between monomers and oligomeric species.

Table 1: Experimentally determined sedimentation coefficients for Aβ42 monomer and small oligomer.

	Monomer (S)*	Small Oligomer (S)*
Aβ42	0.62±0.02	2.56±0.32
AF488-Aβ42	0.80±0.01	2.32±0.14

*Sedimentation coefficients for the monomeric and small oligomeric species of Aβ42 were determined from $c(s)$ distributions. Weight averaged $s_{20,w}$-values and standard deviations were calculated for at least 4 independent sample preparations.

Fig. 2 shows the $c(s)$ distributions obtained for 5 and 10 μM Aβ42. At these medium Aβ42 concentrations, larger aggregates became detectable aside from the small oligomer. In Fig. 3, three $c(s)$ distributions obtained for high Aβ42 concentrations are shown, which demonstrate that the small oligomer is still detectable under conditions where already larger aggregates have been considerably formed. In Table 1 the mean of the $s_{20,w}$-values for the monomer and for the small oligomer are summarized for Aβ42 and AF488-Aβ42. From these values the hydrodynamic radii of a hexamer and a pentamer have been calculated according to equation S1 (Table S2).

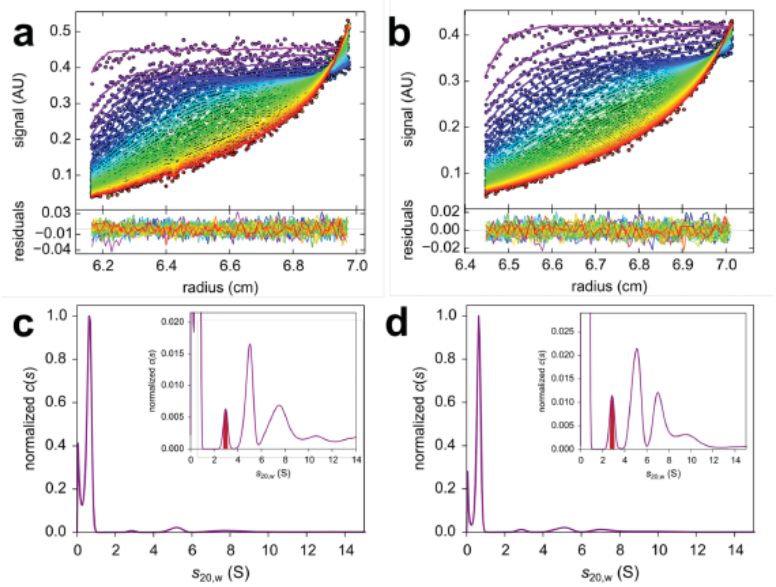

Figure 2. SV analysis at medium Aβ42 concentrations confirms the existence of the small oligomer between 2 S and 3 S and an increasing fraction of larger assemblies with *s*-values between 3 and 12 S. On top raw data of 5 µM (**a**) and 10 µM Aβ42 (**b**) together with overlaid fit results and residuals attached below are shown. The corresponding *c*(*s*) results for 5 µM (**c**) and 10 µM Aβ42 (**d**) are shown below. Sedimentation was performed at 50,000 rpm, 20°C and monitored with absorbance detection. Detection wavelength was 208 nm for 5 µM and 220 nm for 10 µM Aβ42. The *c*(*s*) distribution was normalized to maximum *c*(*s*) value. The insets show the distributions with an expanded *y* scale.

In summary, SV measurements covering a c_0 range from 0.1 µM to 160 µM consistently revealed the existence of a small oligomer at 2.32 S for AF488-Aβ42 or 2.56 S for Aβ42, respectively. According to model calculations (Fig. 4 and Table 2) the hexamer is the largest and the tetramer the smallest oligomer, which are in agreement with an $s_{20,w}$ -value between 2 and

3 S. A trimer as possible configuration can be excluded based on the assigned *s*-value, since only under the assumption of a perfect sphere an $s_{20,w}$ -value of 2 S could be reached for a particle with a mass three times that of the AF488-Aβ42 monomer.

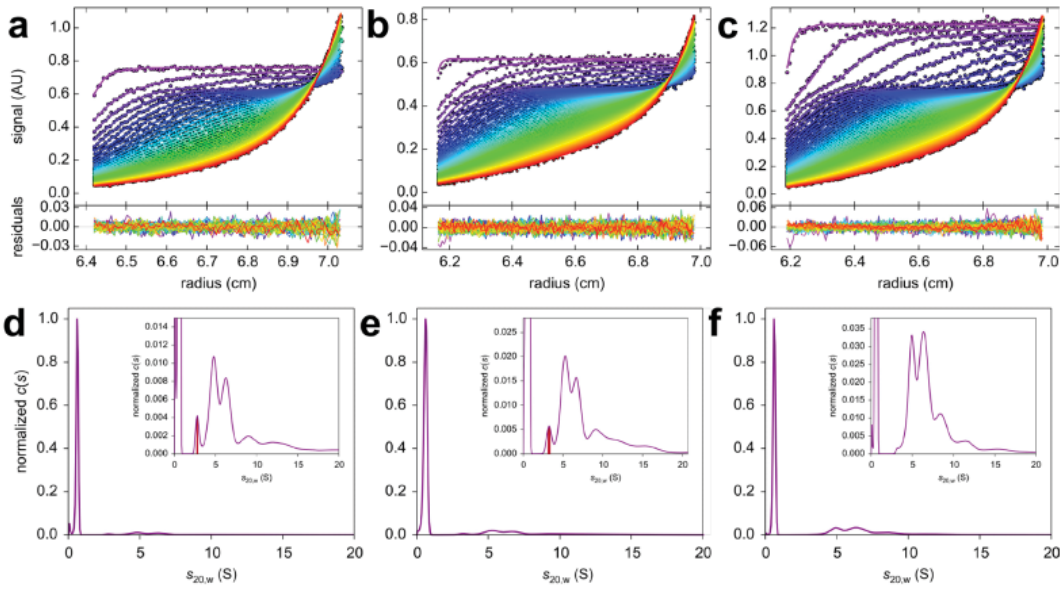

Figure 3. SV analysis at high Aβ42 concentration. On top raw data overlaid with fit data and corresponding residuals are shown for 32 µM (a), 95 µM (b), and 160 µM (c) Aβ42. Below, *c*(*s*) analysis reveals the existence of a high fraction of larger oligomeric species aside from the monomer and a comparably low fraction of the 2 to 3 S species for 32 µM (**d**), 95 µM (**e**), and 160 µM (**f**) Aβ42. Sedimentation was performed at 60,000 rpm, 10°C and monitored with absorbance detection at 280 nm. The *c*(*s*) distribution was normalized to maximum *c*(*s*) value. The insets show the distributions with an expanded *y*-scale.

MD simulations provide size and shape information about early oligomeric species. The low percentage of the small oligomeric species did not allow retrieving reliable shape information from the SV experiment, which would have been necessary for the determination of mass or the number of monomeric units of the *s*-value species. Therefore, in order to find out the size of the oligomer we performed five independent all-atom MD simulations of 20 Aβ42 monomers inserted in a cubic box at a solute concentration of ~0.8 mM and estimated the sedimentation coefficents of the modelled Aβ42 oligomers.[46] The total simulation time was 1 μs. Normalized distributions of the sedimentation coefficient for the three oligomer orders are shown in Fig. 4. The resulting weight average *s*-values for the calculated distribution are listed in Table 2. Tetramers displayed the lowest sedimentation coefficients with an average value of 2.09±0.06 S, followed by pentamers with 2.38±0.06 S and hexamers with an average value of 2.61±0.07 S. For the current analysis we used 576 tetramers, 123 pentamers and 299 hexamers. The *s*-values obtained for the small oligomeric species collected in five MD simulations showed a distribution; i.e. hexamers were found with *s*-values between 2.42 S and 2.90 S, which seems to approach a Gaussian-like shape with higher sampling. This distribution reflects the heterogeneity of the simulated oligomers with regard to their surface area. Nevertheless the overlap between two adjacent species is not exceeding 0.3 S units.

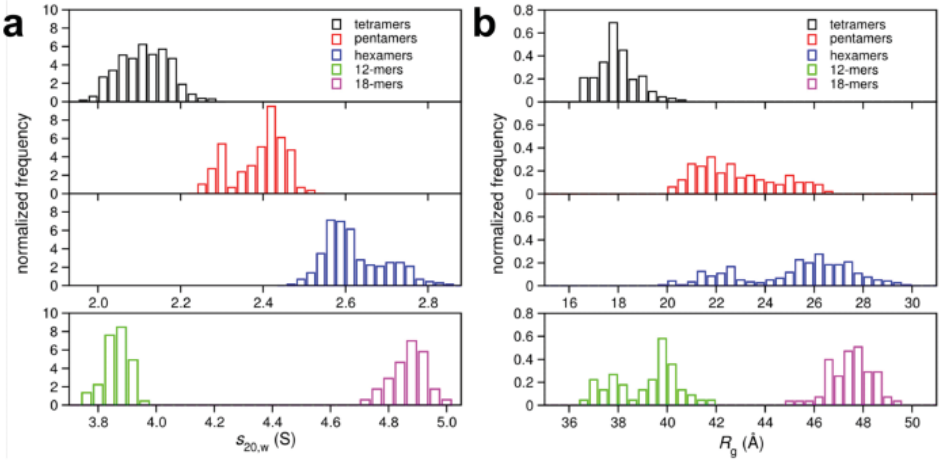

Figure 4. Calculated sedimentation coefficients and radii of gyration of Aβ42 oligomers obtained by MD simulations. (**a**) Normalized distributions of sedimentation coefficients for Aβ42 tetramers (black), pentamers (red) and hexamers (blue) obtained from MD simulations. (**b**) Normalized radii of gyration for the ensembles of Aβ42 tetramers (black), pentamers (red) and hexamers (blue) obtained from MD simulations. The $s_{20,w}$ as well as R_g distributions for 12-mers (green) and 18-mers (magenta) were extrapolated from the hexamer distribution by scaling the ensemble with the cubic root of the mass assuming a common shape. All values for tetra- to hexameric Aβ42 oligomers were calculated with the program HydroPro.[47] Corresponding weight averaged *s*-values are summarized in Table 2.

Small angle neutron scattering studies of Aβ42 in solution demonstrate a penta- to hexamer. In contrast to SV with fluorescence detection, for SANS measurements the peptide can be used without the addition of a dye, but an equivalent D_2O buffer needs to be used to reduce the buffer scattering. For the relative low concentrations used in aggregation studies, a long counting time is required to have reasonable statistical accuracy as the detected signal at larger wave vectors is two orders of magnitude below the buffer scattering. To slow down the

aggregation process and allow measurement times of about 8 h for several detector distances without significant change in the sample, the measurements have been performed at a lower temperature of 7°C. Aβ42 with incubation times between 0.5 and 316 h has been measured by SANS (Fig. 5) for concentrations of 1 mg/ml (221 μM), 0.25 mg/ml (55 μM) and 0.1 mg/ml (22 μM).

Table 2. Average sedimentation coefficients for Aβ42 tetramers, pentamers and hexamers obtained from MD simulated oligomeric structures.

Oligomer	Tetramer	Pentamer	Hexamer
s-value (S)	2.09±0.06	2.38±0.06	2.61±0.07
No. of conformations	576	123	299

The number of conformations is the total number before the clustering algorithm was applied. All values were calculated with the program HydroPro[47].

SANS measurements showed that even at low temperature and relative low concentrations, aggregates of all sizes are formed immediately after the addition of buffer to the dry peptide. The measured intensities after buffer subtraction were analysed by a model adding contributions of larger aggregates and complexes, midsize aggregates, small oligomers and monomers as shown in Fig. 5A. Except for the monomer, the populations of the different assembly states were determined in accompanying measurements by dynamic light scattering or AFM images of dried samples (data not shown). Large aggregates or complexes with sizes larger than 50 nm contribute at low Q by a power law $\sim Q^{-d}$ with d between 5/3 and 3 as expected for networks/gels.[48] Midsize aggregates, such as protofibrils or fibrils are modelled by an ellipsoid of revolution with radii between 50 nm and 10 nm.[1] Small oligomers are modelled by a

Beaucage model ($F(R_g, d)$) providing the radius of gyration (R_g) of the small aggregates with fixed dimensionality.[49] Monomers contribute with a fixed R_g=1 nm as a background contribution, which cannot be resolved for all measurements. Small oligomers with R_g between 1 nm and 5 nm were observed at different concentrations throughout the experiments (Fig. 5B). To elucidate which R_g is to be expected for oligomers of different sizes we calculated R_g for the ensemble of structures generated by our MD simulations (Fig. 4). For the estimation of the R_g values for larger oligomers, we scaled the R_g distribution of the hexamers by the cubic root of mass assuming that the general shape does not change.

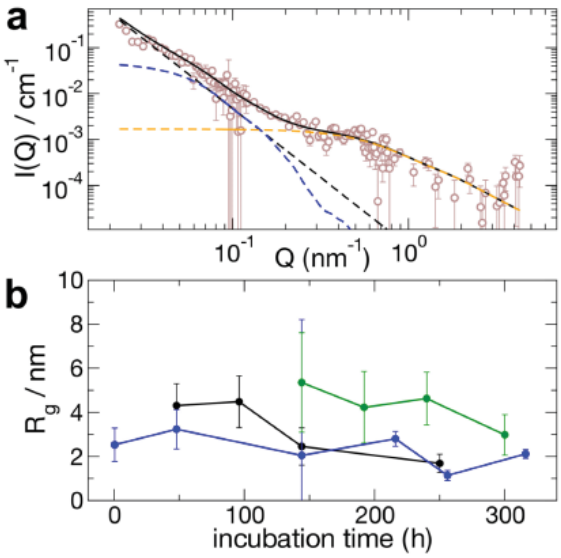

Figure 5. Results from SANS scattering experiments after prolonged incubation of Aβ42 . Measurement and incubation was at 7°C in 50 mM sodium phosphate buffer, pH 7.4 with 150 mM NaCl in 100 % D_2O. (**a**) Exemplary SANS scattering intensity after 0.5 h. Contributions to the scattered intensity arise from aggregates larger than 50 nm conforming to a power law (black broken line), mid-size aggregates modelled as ellipsoid of revolution (blue broken line)

and small oligomers (orange broken line), which are modelled by a Beaucage function. A vanishing background of monomers is modelled as Beaucage function with fixed R_g=1 nm. The combined fit result is shown as black solid line. Ellipsoids have radii between 50 nm and 10 nm. (**b**) Radius of gyration of small oligomers from SANS analysis after incubation at concentrations of 1 mg/ml (black), 0.25 mg/ml (blue), and 0.1 mg/ml (green), respectively.

For the lowest concentration (0.25 mg/ml) the always present oligomers with R_g~2.3 nm correspond to pentamer and/or hexamer. According to Fig. 4 it is difficult to discriminate between pentamers and hexamers based on the R_g value only. At 1 mg/ml the small oligomers had sizes of around 4 nm at incubation times below 120 h; after 120 h incubation we find smaller aggregates again with R_g of about 2 nm, which probably correspond to a pentamer/hexamer (Fig. 4). At the shortest times it was not possible to discriminate between different size classes due to a strong overlap.

Discussion

Our study shows the occurrence of small oligomeric assemblies built by five to six monomeric units of the Aβ42 peptide in solution. This conclusion emerged from the application of two independent experimental approaches, which are based on different physical principles, SV analysis and SANS. The two approaches were bridged by MD calculations. The experimentally determined *s*-value of the small oligomer was compared to *s*-values which had been calculated for a set of different oligomers generated by MD simulations. According to this comparison the hexamer appeared to be the most likely species. From SANS measurements radii of gyration between 2 and 5 nm had been obtained, which would be in agreement with radii of gyration of

assemblies ranging from pentamers to 18-mers calculated for the same set of MD simulated oligomers. For better comparability between *s*-value and radius of gyration the hydrodynamic radii for Aβ42 tetramers to hexamers had been calculated based on the experimentally determined *s*-values (Eq. S1, Table S2). The tetramer appears to be less likely because of a hydrodynamic radius smaller than the determined radii of gyration. In summary these comparisons led us to a model of a penta- to hexamer for the small oligomeric Aβ42 species. Data interpretation was further supported by MD simulations of Aβ42 assembly, which were performed in adaptation to the experimental conditions.

In SV as well as SANS experiments, a small fraction of about 1 to 10 % of total Aβ42 could be detected in the pentamer/hexamer state aside from the dominant monomeric Aβ42 species and larger oligomers present only at higher concentrations. The consistently low fraction of the small oligomeric species over a broad range of total Aβ42 concentrations, which is reported by both methods, is a strong indicator of its role as a reaction intermediate with low population.

Within the accessible Aβ42 concentration ranges it turned out to be impossible to shift the equilibrium towards higher fractions of the pentamer/hexamer. At concentrations below 10 µM, the pentamer/hexamer is the sole species aside from the monomer. At higher concentrations, the pentamer/hexamer appears to be in a steady-state equilibrium with the monomer and larger oligomeric species, representing a lowly populated reaction intermediate. This classifies the pentamer/hexamer to be on pathway with regard to fibril formation.

Ahmed et al. reported the characterization of a penta- or hexameric Aβ42 with structural information from liquid as well as solid state NMR.[23] They also used a low salt phosphate buffer and a similar pretreatment of the Aβ42 peptide. In contrast to our study the oligomeric particle

they described had dimensions which would lead to a sedimentation coefficient of about 6 S, definitely much larger than our species at about 2.6 S. Therefore our penta- to hexamer has to be a different oligomeric species. These differences might be caused by a deviating peptide conformation and /or packing. Furthermore we always observed a considerable amount of free monomer in the presence of the oligomeric species which appears to be absent in the before mentioned study.

In earlier studies, small Aβ assemblies with 2 to 6 monomeric units have been identified mostly on the basis of SDS-PAGE analysis of either cross-linked or non-cross linked samples.[15,16] In addition, a number of computational studies of Aβ oligomerization revealed the existence of several small assemblies, which considerably vary with regard to secondary structure content and overall appearance.[46,50] In a study of Aβ42 fused to GroES and ubiquitin and performed at high pH in the presence of urea, Aβ42 assembled into SDS-resistant hexamers and tetramers.[51] This study implies that only the most stable complexes will occur under the chosen reaction conditions. This is in contrast to our study where we had not to rely on comparisons to size standards and could perform the measurements at standard pH and salt concentrations.

Our results clearly demonstrate that solutions of the Aβ42 peptide do not contain dimers, trimers or tetramers at detectable amounts. Under the assumption of a rapid equilibrium between these small oligomers the lower limit of detection would be increased due to broadening of the peak or missing resolution of single species to about 5 % according to SV data simulations. A possible explanation for the appearance of these small species in a number of other studies would be that these species represent fragmentation products of larger species. In our study the smallest

detectable species is a penta- to hexamer. The fraction of this species is regardless of total Aβ42 concentration close to 1 % of the sedimentation boundary. To the best of our knowledge the existence of these oligomeric species in solution has not been demonstrated yet. The closest others got thus far was by the application of IMS-MS,[52,53] which however required the transfer of ionized molecules and molecular complexes into the gas phase, leaving space for additional events to take place. Nevertheless, it remains reasonable to assume that, because of the concentration dependency of the aggregation, a low concentration may exist, at which only dimers and trimers but no larger oligomers are in equilibrium with the monomer. Lowering the total Aβ42 concentration in our experiments has been one of the strategies we followed in order to suppress the conversion into large aggregates and to increase the fraction of the small oligomeric species, yet we did not observe dimers and trimers.

Our previous studies by sedimentation velocity centrifugation revealed the power of the method to characterize Aβ oligomeric species in equilibrium in solution. The formerly observed gap in the size distribution could be further restricted. We interpreted this gap as indicative for the size, i.e. *s*-value, range of a so called nucleus of aggregation according to the assumption of a nucleated aggregation mechanism. A nucleus would be the smallest assembly, which favours the addition of further monomers or oligomers to itself over its dissociation. Therefore a nucleus is a kinetically instable intermediate, which was up to now elusive to experimental detection. The hydrodynamic radius of the nucleus has been estimated to be between 5 and 50 nm according to fluorescence correlation spectroscopy measurements performed by Garai and colleagues.[54] This boundary is similar to our estimated size region between 1 and 4 S, although the size of our determined penta-to hexameric species with R_H between 2.3 and 2.8 nm is clearly smaller.

In summary, the current study is the first experimental proof for the existence of small Aβ assemblies of the size of a pentamer to hexamer in solution. It would be desirable to verify whether these penta- /hexameric species exhibit the primary toxicity leading to synapse failure and finally to memory loss. To address this question, larger quantities of this species have to be obtained first, which is our goal for future studies.

METHODS

Amyloid-β Peptides. Synthetic Aβ42 peptide was purchased as trifluoroacetate salt (Bachem, H-1368). Aβ42 was first dissolved in 100 % 1,1,1,3,3,3-hexafluoro-2-propanol (HFIP) for at least 12 h in order to remove any preexisting aggregates. Before usage HFIP was removed by lyophilisation. Aliquots were stored at -80°C until use. Repeated freeze thaw cycles were generally avoided.

For fluorescence detection measurements we used recombinantly produced Aβ42 with an additional cysteine residue at position 0. Cloning was based on a plasmid encoding wildtype Aβ(1-42) as a fusion protein with an N-terminal His6-tag, a solubilizing fusion partner (NANP)19 and a modified tobacco etch virus protease (TEV) recognition site, which was kindly provided by Finder, Glockshuber and coworkers.[55] Cys_0-Aβ42 was labelled by maleimide chemistry with AlexaFluor488 (Molecular Probes, Thermo Fisher Scientific) including a short linker $(CH_2)_5$. The dye conjugate was further purified by SEC from unincorporated dye and is named AF488-Aβ42. The partial specific volume of the dye-peptide conjugate was calculated according to Durchschlag[56,57] as $\bar{v} = 0.7127$ cm^3/g; see also $\bar{v}$ values summarized in Table S1.

A synthetic, covalently linked Aβ40 dimer was obtained by using Aβ40 with an additional Cys residue at the N-terminus, Cys-Aβ40 (Bachem H-7368) under oxidizing conditions. The

disulphide bridge linked dimer was purified by high performance liquid chromatography (HPLC). The partial specific volume calculated for the Cys-Aβ40-dimer with the help of SEDNTERP (vs. 20120828 BETA)[58] is $\bar{v}$=0.7316 cm^3/g at 20°C and $\bar{v}$=0.7295 cm^3/g at 15°C (Table S1).

Sedimentation Velocity Centrifugation. AUC was performed with an Optima XL-A or ProteomLab XL-A (Beckman Coulter). The ProteomLab XL-A is equipped with standard absorbance optics and an additional fluorescence detection system (Aviv Biomedical Inc.). Samples were filled either in 12 mm titanium double sector cells with 400 µl filling volume (Nanolytics) for absorbance detection or in 3 mm titanium double sector cells with 100 µl filling volume for fluorescence measurements. An integrated spacer places the sample volume to the upper third of a cell assembly (Nanolytics) guaranteeing an optimal focus position for the fluorescence detection. For both cell assemblies quartz windows were used. Labelled or unlabelled Aβ42, pre-treated with HFIP, was dissolved in 10 mM sodium phosphate buffer, pH 7.4 at various concentrations between 0.1 to 160 µM directly prior to the SV experiments. All samples had been thermally equilibrated within the centrifuge for about 2 h before starting the run. Sedimentation velocity runs with absorbance detection were performed either at 50,000 rpm or at 60,000 rpm, equivalent to 201,600g or 289,000g, respectively, at the maximum radius of 7.2 cm. At concentrations above 20 µM the runs were performed at 10 or 15°C in order to suppress aggregation during centrifugation. For absorbance data collection a radial resolution of 30 µm was chosen together with the shortest possible scan interval, which was ~1.5 min. The detection wavelength was chosen such that sample absorbance was between 0.5 and 1.2 OD. For the fluorescence detection system, based on laser excitation at 488 nm, the radial resolution is fixed at 20 µm and data acquisition is not done sequentially but simultaneously for all sample

sectors, leading to scan intervals shorter than 1 min. Each sample sector was measured with an individually adjusted signal amplification factor resulting in 2000–3400 relative fluorescence units (RFU). All SV data were analysed using the $c(s)$-distribution analysis using the size-distribution option "with prior probabilities" as implemented in the software package SEDFIT (vs. 14.7g; May 2015) (http://www.analyticalultracentrifugation.com/)[59]. For data analysis a resolution of 0.05 S with a confidence level (F-ratio) of 0.95 was chosen for the appropriate s-value range. For the determination of trace amounts of oligomers the protocol from Wafer et al. was followed.[42] After repeating the $c(s)$ calculation by alternating between simplex algorithm and Marquardt-Levenberg until no further change in rmsd is observable, the c(s) model is exchanged by a model of non-interacting species. This model can then be tested by F-statistics for the necessity of the high molecular weight species. This was achieved by calculating a critical relative rmsd value based on the model including the large species. In case the equivalent fit excluding the large species results in an rmsd equal or smaller than the before determined critical rmsd the large species is not significant, otherwise it is. Thus significance of the oligomeric species was proven for four data sets by an increase of rmsd value above the critical rmsd upon removal the larger species (Fig. 1a,b). Except for the nonlinear detection correction we completely abstained from using the tools implemented in SEDFIT to correct data for fluorescence related optical artefacts in order to avoid possible impacts on the reliability of the afore mentioned procedure. This was possible due to clipping the data range close to the bottom, where shadowing effects lead to a signal decrease. All presented $c(s)$ distributions have root mean square deviations of $\leq 1\%$ of the total signal. Sedimentation coefficients are reported as $s_{20,w}$ values in Svedberg units with 1 S = 10^{-13} s, which represent the apparent sedimentation coefficient normalized to the standard conditions of 20 °C and pure water solvent.

Small Angle Neutron Scattering. Peptides were dissolved in HFIP for three weeks and dried before being resolved in deuterated buffer (50 mM Nap*i*, pH 7.4 + 150 mM NaCl in 100 % D_2O, filtered with Anopore Whatman, pore size 20 nm). Samples were incubated at 7°C at rest. SANS experiments were performed at the small angle diffractometer, KWS-2 of Heinz Maier-Leibnitz Zentrum (MLZ Garching, Germany) with wavelengths between 0.47 nm and 0.81 nm and detector distances from 1.1 m to 19.7 m to cover a wave vector range of 0.001 $Å^{-1}$ to 0.5 $Å^{-1}$.[60] The wavelength spread was $\Delta\lambda/\lambda = 0.2$. Measurement times from 1 h to 4 h dependent on detector distance and sample scattering were used. Samples and buffer measurements for background correction were performed in quartz cells of 2 mm thickness together with appropriate measurements for detector sensitivity and dark current. Appropriate standard methods for evaluation and background correction were used from the software QtiKWS.[61]

Molecular Dynamics calculations. Five independent all-atom MD simulations of twenty Aβ42 monomers inserted in a cubic box with a side length of 350 Å and periodic boundary conditions were performed. We applied different initial velocity distributions for each simulation and simulated in total 2.5 μs, with 500 ns per simulation. We used the parallel processing MD software Gromacs 4.5.5 for performing the simulations with a leap-frog stochastic dynamics integrator, the OPLS/AA force field,[62-64] and implicit solvent using a Generalized Born model with a hydrophobic solvent accessible surface area term (GBSA).[65] The temperature coupling was done via velocity rescaling with a stochastic term algorithm[66] using a time constant for coupling of 2 ps and keeping the system at 300 K. Electrostatic interactions were treated with the cut-off method with a value of 1.2 nm and van der Waals interactions were also cut at 1.2 nm. Hydrogen atoms were treated as virtual interaction sites, permitting an integration time step of 4 fs while maintaining energy conservation.[67] From the 5× 500 ns simulations we extracted all

tetramer, pentamer and hexamer conformations and clustered all structures for each oligomer size using the method of Daura and colleagues[68] with a cut-off of 0.2 nm. For the resulting cluster centres we calculated sedimentation coefficients using the program HydroPro.[47] To this end, we first estimated the partial specific volume as the total protein volume divided by the molecular weight of the protein. To estimate the total protein volume we used the program 3V Volume Calculator,[69] and for determining the molecular weight of the protein we used VMD.[70]

Acknowledgements

The authors gratefully acknowledge the computing time granted on the supercomputers JUROPA and JURECA at Jülich Supercomputing Centre (grant numbers JICS61 and JICS64). Further, the authors thank the Helmholtz Association for funding part of this work through the Helmholtz-Portfolio Topics "Technology and Medicine" (CD, LNS, DW) and “Drug Research” (DW). We would like to express our great appreciation to Dieter Richter for his valuable and constructive suggestions regarding SANS measurements. We thank Stephanie Schiefer for her skillful assistance in atomic force microscopy. This work is based on experiments performed at the Heinz Maier-Leibnitz Zentrum (MLZ), Garching, Germany.

Author information

These authors contributed equally to this work

Martin Wolff and Bo Zhang Haagen

Corresponding Author

* l.nagel-steger@fz-juelich.de, Institute of Complex Systems, Structural Biochemistry (ICS-6). Research Centre Juelich, Wilhelm Johnen Strasse, 52425 Juelich, Germany.

Present Addresses

†Martin Wolff, Physikalische Biochemie, University Potsdam, 14476 Golm, Germany.

Affiliations

Contributions

The manuscript was written through contributions of all authors. All authors have given approval to the final version of the manuscript. M.W., C.D., B.Z.-H., B.B., M.S. and A.R. were responsible for in vitro and in vivo data generation, experimental design and data interpretation. R.B., B.S., D.W., and LNS were responsible for study conceptualization, design, data interpretation and manuscript preparation with all authors providing editorial comments

Competing financial interests

The authors declare no competing financial interest.

Supporting Information.

Partial specific volumes and molar masses of the Aβ-peptides used in this study (Table S1); Detectability of a dimer by SV analysis (Figure S1); Atomic force microscopy of fluorescently labelled Aβ42 (Figure S3); Calculation of hydrodynamic radii for different oligomers based on determined sedimentation coefficients (Eq. S1, Table S2).

REFERENCES

1 Meier, B. H. & Bockmann, A. The structure of fibrils from 'misfolded' proteins. *Curr Opin Struct Biol* **30C**, 43-49, doi:10.1016/j.sbi.2014.12.001 (2014).

2 Comellas, G. & Rienstra, C. M. Protein structure determination by magic-angle spinning solid-state NMR, and insights into the formation, structure, and stability of amyloid fibrils. *Annu Rev Biophys* **42**, 515-536, doi:10.1146/annurev-biophys-083012-130356 (2013).

3 Cerasoli, E., Ryadnov, M. G. & Austen, B. M. The elusive nature and diagnostics of misfolded Abeta oligomers. *Front Chem* **3**, 17, doi:10.3389/fchem.2015.00017 (2015).
4 Hayden, E. Y. & Teplow, D. B. Amyloid beta-protein oligomers and Alzheimer's disease. *Alzheimers Res Ther* **5**, 60, doi:10.1186/alzrt226 (2013).
5 Teplow, D. B. On the subject of rigor in the study of amyloid beta-protein assembly. *Alzheimers Res Ther* **5**, 39, doi:10.1186/alzrt203 (2013).
6 Nagel-Steger, L., Owen, M. C. & Strodel, B. An account of amyloid oligomers: facts and figures obtained from experiments and simulations. *Chembiochem*, doi:10.1002/cbic.201500623 (2016).
7 Alzheimer, A. Über eine eigenartige Erkrankung der Hirnrinde. *Allgemeine Zeitschrift für Psychiatrie und psychisch-gerichtliche Medizin (Berlin)* **64**, 146-148 (1907).
8 Joachim, C. L. & Selkoe, D. J. The seminal role of beta-amyloid in the pathogenesis of Alzheimer disease. *Alzheimer Dis Assoc Disord* **6**, 7-34 (1992).
9 Klein, W. L., Krafft, G. A. & Finch, C. E. Targeting small Abeta oligomers: the solution to an Alzheimer's disease conundrum? *Trends Neurosci* **24**, 219-224 (2001).
10 Klein, W. L. Abeta toxicity in Alzheimer's disease: globular oligomers (ADDLs) as new vaccine and drug targets. *Neurochem Int* **41**, 345-352 (2002).
11 Shankar, G. M. *et al.* Amyloid-[beta] protein dimers isolated directly from Alzheimer's brains impair synaptic plasticity and memory. *Nat Med* **14**, 837-842, doi:10.1038/nm1782 (2008).
12 Mc Donald, J. M. *et al.* The aqueous phase of Alzheimer's disease brain contains assemblies built from approximately 4 and approximately 7 kDa Abeta species. *Alzheimers Dement* **11**, 1286-1305, doi:10.1016/j.jalz.2015.01.005 (2015).
13 Garai, K. & Frieden, C. Quantitative analysis of the time course of Abeta oligomerization and subsequent growth steps using tetramethylrhodamine-labeled Abeta. *Proc Natl Acad Sci U S A* **110**, 3321-3326, doi:10.1073/pnas.1222478110 (2013).
14 Garzon-Rodriguez, W., Sepulveda-Becerra, M., Milton, S. & Glabe, C. G. Soluble amyloid Abeta-(1-40) exists as a stable dimer at low concentrations. *J Biol Chem* **272**, 21037-21044 (1997).
15 Bitan, G., Lomakin, A. & Teplow, D. B. Amyloid beta-protein oligomerization: prenucleation interactions revealed by photo-induced cross-linking of unmodified proteins. *J Biol Chem* **276**, 35176-35184, doi:10.1074/jbc.M102223200 (2001).
16 Burdick, D. *et al.* Assembly and aggregation properties of synthetic Alzheimer's A4/beta amyloid peptide analogs. *J Biol Chem* **267**, 546-554 (1992).
17 Podlisny, M. B. *et al.* Aggregation of secreted amyloid beta-protein into sodium dodecyl sulfate-stable oligomers in cell culture. *J Biol Chem* **270**, 9564-9570 (1995).
18 Walsh, D. M., Tseng, B. P., Rydel, R. E., Podlisny, M. B. & Selkoe, D. J. The oligomerization of amyloid beta-protein begins intracellularly in cells derived from human brain. *Biochemistry* **39**, 10831-10839 (2000).
19 Muller-Schiffmann, A. *et al.* Molecular engineering of a secreted, highly homogeneous, and neurotoxic abeta dimer. *ACS Chem Neurosci* **2**, 242-248, doi:10.1021/cn200011h (2011).
20 Roher, A. E. *et al.* Morphology and toxicity of Abeta-(1-42) dimer derived from neuritic and vascular amyloid deposits of Alzheimer's disease. *J Biol Chem* **271**, 20631-20635 (1996).

21 Roychaudhuri, R. *et al.* C-Terminal turn stability determines assembly differences between Aβ40 and Aβ42. *Journal of Molecular Biology* **425**, 292-308, doi:10.1016/j.jmb.2012.11.006 (2013).
22 Cernescu, M. *et al.* Laser-induced liquid bead ion desorption mass spectrometry: an approach to precisely monitor the oligomerization of the beta-amyloid peptide. *Anal Chem* **84**, 5276-5284, doi:10.1021/ac300258m (2012).
23 Ahmed, M. *et al.* Structural conversion of neurotoxic amyloid-[beta]1-42 oligomers to fibrils. *Nat Struct Mol Biol* **17**, 561-567, doi:10.1038/nsmb.1799 (2010).
24 Viola, K. L. & Klein, W. L. Amyloid beta oligomers in Alzheimer's disease pathogenesis, treatment, and diagnosis. *Acta Neuropathol* **129**, 183-206, doi:10.1007/s00401-015-1386-3 (2015).
25 Lesné, S. E. Toxic oligomer species of amyloid-beta in Alzheimer's disease, a timing issue. *Swiss Med Wkly* **144**, w14021, doi:10.4414/smw.2014.14021 (2014).
26 Rahimi, F., Shanmugam, A. & Bitan, G. Structure-function relationships of pre-fibrillar protein assemblies in Alzheimer's disease and related disorders. *Curr Alzheimer Res* **5**, 319-341 (2008).
27 Fändrich, M. Oligomeric intermediates in amyloid formation: structure determination and mechanisms of toxicity. *Journal of Molecular Biology* **421**, 427-440, doi:10.1016/j.jmb.2012.01.006 (2012).
28 Benilova, I., Karran, E. & De Strooper, B. The toxic A[beta] oligomer and Alzheimer's disease: an emperor in need of clothes. *Nat Neurosci* **15**, 349-357, doi:10.1038/nn.3028 (2012).
29 Schuck, P., Perugini, M. A., Gonzales, N. R., Howlett, G. J. & Schubert, D. Size-distribution analysis of proteins by analytical ultracentrifugation: strategies and application to model systems. *Biophys J* **82**, 1096-1111, doi:10.1016/S0006-3495(02)75469-6 (2002).
30 Pekar, A. & Sukumar, M. Quantitation of aggregates in therapeutic proteins using sedimentation velocity analytical ultracentrifugation: practical considerations that affect precision and accuracy. *Anal Biochem* **367**, 225-237, doi:10.1016/j.ab.2007.04.035 (2007).
31 Wolff, M. *et al.* Amyloid beta oligomeric species present in the lag phase of amyloid formation. *PLoS One* **10**, e0127865, doi:10.1371/journal.pone.0127865 (2015).
32 Brookes, E., Cao, W., Demeler, B. in *Eur Biophys J.* Vol. 39 (2010).
33 Demeler, B., Brookes, E., Nagel-Steger, L. in *Methods Enzymol.* Vol. 454 (2009).
34 Nagel-Steger, L., Demeler, B., Meyer-Zaika, W., Hochdörffer, K., Schrader, T., Willbold, D. in *Eur Biophys J.* Vol. 39 (2010).
35 Zhang-Haagen, B. *et al.* Monomeric amyloid beta peptide in hexafluoroisopropanol detected by small angle neutron scattering. *PLoS One* **11**, e0150267, doi:10.1371/journal.pone.0150267 (2016).
36 Schuck, P. Sedimentation patterns of rapidly reversible protein interactions. *Biophys J* **98**, 2005-2013, doi:10.1016/j.bpj.2009.12.4336 (2010).
37 Schuck, P. Diffusion of the reaction boundary of rapidly interacting macromolecules in sedimentation velocity. *Biophys J* **98**, 2741-2751, doi:10.1016/j.bpj.2010.03.004 (2010).
38 Larson, M. E. & Lesné, S. E. Soluble Abeta oligomer production and toxicity. *J Neurochem* **120 Suppl 1**, 125-139, doi:10.1111/j.1471-4159.2011.07478.x (2012).

39 Lesné, S. *et al.* A specific amyloid-beta protein assembly in the brain impairs memory. *Nature* **440**, 352-357, doi:10.1038/nature04533 (2006).
40 Bernstein, S. L. *et al.* Amyloid beta-protein: monomer structure and early aggregation states of Abeta42 and its Pro19 alloform. *J Am Chem Soc* **127**, 2075-2084, doi:10.1021/ja044531p (2005).
41 Kheterpal, I., Williams, A., Murphy, C., Bledsoe, B. & Wetzel, R. Structural features of the Abeta amyloid fibril elucidated by limited proteolysis. *Biochemistry* **40**, 11757-11767 (2001).
42 Wafer, L., Kloczewiak, M. & Luo, Y. Quantifying Trace Amounts of Aggregates in Biopharmaceuticals Using Analytical Ultracentrifugation Sedimentation Velocity: Bayesian Analyses and F Statistics. *Aaps J* **18**, 849-860, doi:10.1208/s12248-016-9925-y (2016).
43 Arthur, K. K., Kendrick, B. S. & Gabrielson, J. P. Guidance to Achieve Accurate Aggregate Quantitation in Biopharmaceuticals by SV-AUC. *Methods Enzymol* **562**, 477-500, doi:10.1016/bs.mie.2015.06.011 (2015).
44 Krayukhina, E. *et al.* Aggregation analysis of pharmaceutical human immunoglobulin preparations using size-exclusion chromatography and analytical ultracentrifugation sedimentation velocity. *J Biosci Bioeng* **115**, 104-110, doi:10.1016/j.jbiosc.2012.07.021 (2013).
45 Brown, P. H., Balbo, A. & Schuck, P. A Bayesian approach for quantifying trace amounts of antibody aggregates by sedimentation velocity analytical ultracentrifugation. *Aaps J* **10**, 481-493, doi:10.1208/s12248-008-9058-z (2008).
46 Barz, B., Olubiyi, O. O. & Strodel, B. Early amyloid beta-protein aggregation precedes conformational change. *Chem Commun (Camb)* **50**, 5373-5375, doi:10.1039/c3cc48704k (2014).
47 Ortega, A., Amoros, D. & de la Torre, J. G. Prediction of Hydrodynamic and Other Solution Properties of Rigid Proteins from Atomic- and Residue-Level Models. *Biophys J* **101**, 892-898, doi:DOI 10.1016/j.bpj.2011.06.046 (2011).
48 Shibayama, M., Tanaka, T. & Han, C. C. Small angle neutron scattering study on poly(N-isopropyl acrylamide) gels near their volume-phase transition temperature. *The Journal of Chemical Physics* **97**, 6829-6841, doi:10.1063/1.463636 (1992).
49 Xiao, Y. *et al.* Abeta(1-42) fibril structure illuminates self-recognition and replication of amyloid in Alzheimer's disease. *Nat Struct Mol Biol* **22**, 499-505, doi:10.1038/nsmb.2991 (2015).
50 Nasica-Labouze, J. *et al.* Amyloid beta protein and Alzheimer's disease: when computer simulations complement experimental studies. *Chem Rev* **115**, 3518-3563, doi:10.1021/cr500638n (2015).
51 Ngo, S. & Guo, Z. Key residues for the oligomerization of Abeta42 protein in Alzheimer's disease. *Biochem Biophys Res Commun* **414**, 512-516, doi:10.1016/j.bbrc.2011.09.097 (2011).
52 Zheng, X., Liu, D., Roychaudhuri, R., Teplow, D. B. & Bowers, M. T. Amyloid beta-Protein Assembly: Differential Effects of the Protective A2T Mutation and Recessive A2V Familial Alzheimer's Disease Mutation. *ACS Chem Neurosci* **6**, 1732-1740, doi:10.1021/acschemneuro.5b00171 (2015).

53 Bernstein, S. L. *et al.* Amyloid-beta protein oligomerization and the importance of tetramers and dodecamers in the aetiology of Alzheimer's disease. *Nat Chem* **1**, 326-331, doi:10.1038/nchem.247 (2009).
54 Garai, K., Sahoo, B., Sengupta, P. & Maiti, S. Quasihomogeneous nucleation of amyloid beta yields numerical bounds for the critical radius, the surface tension, and the free energy barrier for nucleus formation. *The Journal of Chemical Physics* **128**, 045102, doi:10.1063/1.2822322 (2008).
55 Finder, V. H., Vodopivec, I., Nitsch, R. M. & Glockshuber, R. The recombinant amyloid-beta peptide Abeta1-42 aggregates faster and is more neurotoxic than synthetic Abeta1-42. *Journal of Molecular Biology* **396**, 9-18, doi:10.1016/j.jmb.2009.12.016 (2010).
56 Durchschlag, H. & Zipper, P. in *Progress in Colloid & Polymer Science: Ultracentrifugation* Vol. 94 (ed G. Lagaly M.D. Lechner (guest editor) F. Kremer) Ch. Calculation of the partial volume of organic compounds and polymers, 20-39 (Springer Verlag Berlin Heidelberg GmbH, 1994).
57 Durchschlag, H. in *Thermodynamic Data for Biochemistry and Biotechnology* (ed Hans-Jürgen Hinz) Ch. Specific Volumes of Biological Macromolecules and Some Other Molecules of Biological Interest, 45-128 (Springer, 1986).
58 Laue, T. M. *SEDNTERP. Web. 09 September 2016.*, <http://bitcwiki.sr.unh.edu/index.php/Main_Page> (2016).
59 Schuck, P. Size-distribution analysis of macromolecules by sedimentation velocity ultracentrifugation and lamm equation modeling. *Biophys J* **78**, 1606-1619, doi:10.1016/S0006-3495(00)76713-0 (2000).
60 Radulescu, A., V. Pipich, H. Frielinghaus, and M.-S. Appavou. KWS-2, the high intensity / wide Q -range small-angle neutron diffractometer for soft-matter and biology at FRM II. *Journal of Physics: Conference Series* **351** (2012).
61 QtiKWS :: SA(N)S Data Reduction and Analysis Program v. 2015-06-29 June 2015 (http://iffwww.iff.kfa-juelich.de/~pipich/dokuwiki/doku.php/qtikws).
62 Jorgensen, W. L., Maxwell, D. S. & TiradoRives, J. Development and testing of the OPLS all-atom force field on conformational energetics and properties of organic liquids. *J Am Chem Soc* **118**, 11225-11236, doi:Doi 10.1021/Ja9621760 (1996).
63 Kaminski, G. A., Friesner, R. A., Tirado-Rives, J. & Jorgensen, W. L. Evaluation and reparametrization of the OPLS-AA force field for proteins via comparison with accurate quantum chemical calculations on peptides. *Journal of Physical Chemistry B* **105**, 6474-6487, doi:Doi 10.1021/Jp003919d (2001).
64 Hess, B., Kutzner, C., van der Spoel, D. & Lindahl, E. GROMACS 4: Algorithms for highly efficient, load-balanced, and scalable molecular simulation. *J Chem Theory Comput* **4**, 435-447, doi:Doi 10.1021/Ct700301q (2008).
65 Qiu, D., Shenkin, P. S., Hollinger, F. P. & Still, W. C. The GB/SA continuum model for solvation. A fast analytical method for the calculation of approximate Born radii. *J Phys Chem A* **101**, 3005-3014, doi:Doi 10.1021/Jp961992r (1997).
66 Bussi, G., Donadio, D. & Parrinello, M. Canonical sampling through velocity rescaling. *J Chem Phys* **126**, doi:10.1063/1.2408420 (2007).
67 Feenstra, K. A., Hess, B. & Berendsen, H. J. C. Improving efficiency of large time-scale molecular dynamics simulations of hydrogen-rich systems. *J Comput Chem* **20**, 786-798 (1999).

68 Daura, X. *et al.* Peptide folding: When simulation meets experiment. *Angew Chem Int Edit* **38**, 236-240, doi:Doi 10.1002/(Sici)1521-3773(19990115)38:1/2<236::Aid-Anie236>3.0.Co;2-M (1999).
69 Voss, N. R., Gerstein, M., Steitz, T. A. & Moore, P. B. The geometry of the ribosomal polypeptide exit tunnel. *Journal of Molecular Biology* **360**, 893-906, doi:DOI 10.1016/j.jmb.2006.05.023 (2006).
70 Humphrey, W., Dalke, A. & Schulten, K. VMD: Visual molecular dynamics. *J Mol Graph Model* **14**, 33-38, doi:Doi 10.1016/0263-7855(96)00018-5 (1996).

SUPPORTING INFORMATION

Aβ42 pentamers to hexamers are the smallest detectable aggregate species in solution.

Martin Wolff[1,2,†], *Bo Zhang-Haagen*[2,3], *Christina Decker*[1], *Bogdan Barz*[2], *Mario Schneider*[1], *Ralf Biehl*[3,4], *Aurel Radulescu*[4], *Birgit Strodel*[2], *Dieter Willbold*[1,2], *and Luitgard Nagel-Steger*[1,2,*]

[1] Institut für Physikalische Biologie, Heinrich-Heine-Universität Düsseldorf, 40225 Düsseldorf, Germany

[2] Institute of Complex Systems, Structural Biochemistry (ICS-6), Research Centre Jülich, 52428 Jülich, Germany

[3] Jülich Centre for Neutron Science & Institute of Complex Systems, Neutron Scattering (JCNS-1&ICS-1), Research Centre Jülich, 52428 Jülich, Germany,

[4] Jülich Centre for Neutron Science, Outstation at MLZ (JCNS-MLZ), Research Centre Jülich, 85747 Garching, Germany

Present Addresses

[†]Martin Wolff, Physikalische Biochemie, University Potsdam, 14476 Golm, Germany.

[‡]Authors equally contributed to the manuscript.

Corresponding Author

* l.nagel-steger@fz-juelich.de, Institute of Complex Systems, Structural Biochemistry (ICS-6). Research Centre Juelich, Wilhelm Johnen Strasse, 52425 Juelich, Germany.

Table S1: Partial specific volumes and molar masses of the Aβ-peptides used in this study.

	Molar mass (g/mol)	$\bar{v}$ at 20°C (cm^3/g)	$\bar{v}$ at 15°C (cm^3/g)
Aβ42	4514.10	0.7377	0.7361
AF488-Aβ42	5337.77	0.7127	
Aβ40	4329.87	0.7341	
Cys-Aβ40	4433.01	0.7316	0.7295
Cys-Aβ40-dimer	8864.00	0.7288	0.7263

Detectability of a dimer by SV analysis

The software package UltraScan II (vs 9.9; rev. 1927) (http:\\www.ultrascan.uthscsa.edu) offers a simulation tool based on finite element (ASTFEM) methods for the calculation of radial sedimentation profiles as a function of time for single or multiple components [1]. Beforehand, the components have to be modelled with regard to their mass, shape and partial specific volume. Afterwards, the calculated sedimentation profiles can be processed by data evaluation software like SEDFIT in order to retrieve for example a $c(s)$ distribution. A model for two ideal, non-interacting components was chosen for monomeric and dimeric cys-Aβ40. To evaluate whether in SV analysis it is possible to specifically detect the dimer we simulated a particle with the double mass of Aβ42 and a slightly more compact shape than the monomer with a theoretical *s*-value between 1.0 and 1.5 S. Assuming a composition of 50 % monomer and 50 % dimer as independent species at 20°C in sodium phosphate buffer the dimer is clearly distinguishable from the monomer by sedimentation velocity centrifugation at maximum speed (289,000g). Experimentally this could be verified by analysing a covalently linked Aβ40 dimer, which was generated by introducing a disulphide bridge between a cysteine engineered at the N-terminus.

Data evaluation reveals a difference in *s*-value of 0.25 S between the monomer and the dimer (Fig. S1).

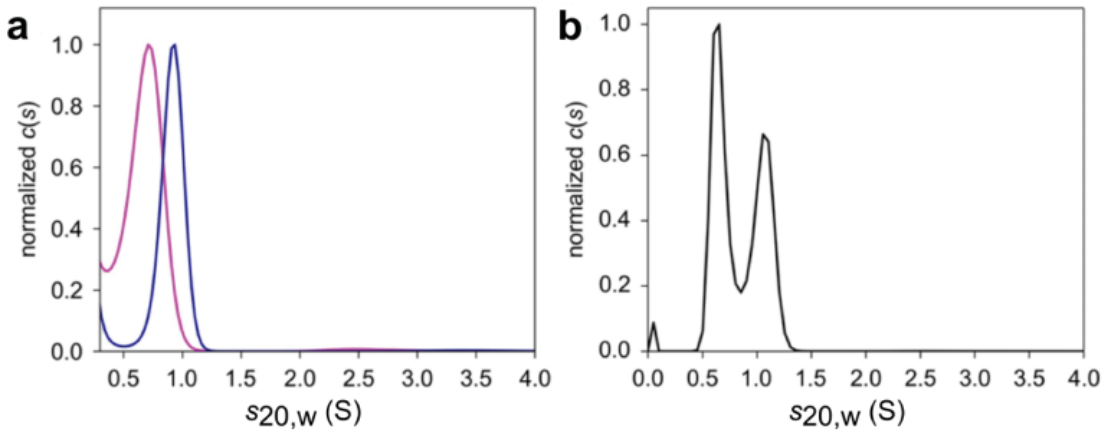

Figure S1: SV analysis of Aβ40 monomer and dimer at 60,000 rpm, 15°C. (**a**) Comparison of monomeric Aβ40 ($s_{20,w}$ = 0.65 S), (magenta) and dimeric Aβ40 (dark blue), which had been covalently linked by a disulfide bridge ($s_{20,w}$=0.9 S). (**b**) c(s) distribution obtained from simulated SV data for a 1:1 mixture of monomeric Aβ40 and dimeric Aβ40, decorated with 0.5 % random noise, 0.02 % radial invariant, and 0.02 % time invariant noise. The frictional ratio was assumed 1.5 for the monomer and 1.4 for the dimer. The *c*(*s*) distributions were normalized according to maximum peak height.

Atomic force microscopy of FITC-Aβ42

In order to demonstrate that the fluorophore labelled Aβ peptide was capable of fibril formation a solution of 1 µM FITC-Aβ42 had been incubated in phosphate buffered saline, pH 7.4 for 5 days at 37°C. Forty-microliter aliquots of the samples were transferred to freshly cleaved mica. After 30 min to 40 min incubation the mica surface was washed three times with 100 µl deionized water (Millipore). Excess water was removed with compressed N_2. Imaging of FITC-Aβ42 was performed with Nanowizard II (JPK Instruments AG) in intermittent contact in air [2],

using standard silicon cantilevers (OLYMPUS OMCL-AC160TS). In AFM fibrils with rather uniform diameter and 100 to 200 nm length were detected (Fig. S2).

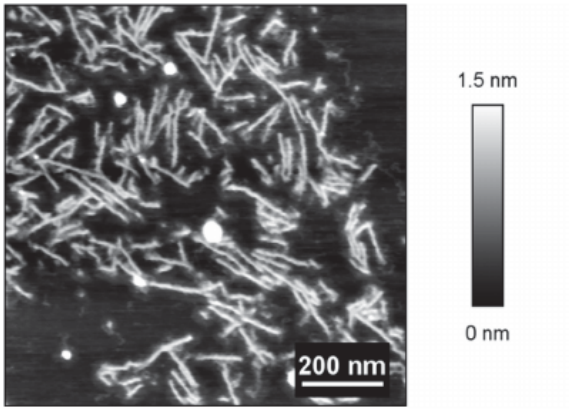

Figure S2: Detection of FITC-Aβ42 fibrils by atomic force spectroscopy. FITC-Aβ42 (1 µM) had been incubated for 5 days at 37 °C. Afterwards the sample had been imaged by atomic force microscopy in air on mica surface. The greyscale on the right side indicates height from black to white.

Calculation of hydrodynamic radii for different oligomers based on determined sedimentation coefficients

For comparability, hydrodynamic radii for three different oligomers, the tetramer, pentamer and hexamer have been calculated assuming a hydration of 0.398 g H_2O/g protein. Equation (S1) is obtained from the Svedberg equation by insertion of the expression for the frictional coefficient $f=6\pi\eta R_H$ according to Stokes' law.

$$R_H = m(1-\bar{v}\rho)/6\pi\eta s \qquad \text{(S1)}$$

with $m = \left(nM_p + \delta n M_p\right)/N_A$ and $\bar{v} = \left(M_p\bar{v}_p + \delta M_p \bar{v}_h\right)/\left(M_p + \delta M_p\right)$

R_H hydrodynamic radius

m	mass of hydrated oligomer build from n monomers
ρ	water density at 20°C: 0.99823g/cm^3
η	water viscosity at 20°C: 0.01002 Poise
s	sedimentation coefficient in water at 20 °C
M_P	molar mass of protein
δ	estimated fraction of bound hydration water, here δ = 0.398 g H_2O/g protein [3-5]
N_A	Avogadro constant
$\bar{v}_p$	partial specific volume of protein (index p)
$\bar{v}_h$	partial specific volume of hydration shell (index h)

The density of hydration shell water is assumed to be 10 % higher than bulk water density [6].

Table S2: Calculated hydrodynamic radii for the different oligomeric states based on experimentally determined sedimentation coefficient.

Given:	**Aβ42**	**MW (g/mol)**	**R_H (nm)**
$s_{20,w}$ = 2.56 S	tetramer	1.8056E+04	1.85
	pentamer	2.2571E+04	2.31
	hexamer	2.7085E+04	2.77
	AF488-Aβ42	**MW (g/mol)**	**R_H (nm)**
$s_{20,w}$ = 2.32 S	tetramer	2.1351E+04	2.63
	pentamer	2.6689E+04	3.28
	hexamer	3.2027E+04	3.94

Sedimentation coefficients of Aβ42 oligomers from MD simulations

To calculate the sedimentation coefficient for different oligomers we selected all tetramers, pentamers and hexamers conformations from the 5 trajectories. Using the Gromos[7] clustering method with a cutoff of 2 Å we conducted a clustering analysis on each of the conformations for a particular oligomer order. The central structures of each cluster were then used for the

calculation of the sedimentation coefficients using the program HydroPro.[8] The partial specific volume needed for the calculation was estimated as the total protein volume, calculated with the 3V Volume Calculator,[9] divided by the molecular weight of the protein, obtained in VMD.[10]

REFERENCES

1 Cao, W. & Demeler, B. Modeling analytical ultracentrifugation experiments with an adaptive space-time finite element solution of the Lamm equation. *Biophys J* **89**, 1589-1602, doi:10.1529/biophysj.105.061135 (2005).

2 Serem, W. K., Bett, C. K., Ngunjiri, J. N. & Garno, J. C. Studies of the growth, evolution, and self-aggregation of beta-amyloid fibrils using tapping-mode atomic force microscopy. *Microsc Res Tech* **74**, 699-708, doi:10.1002/jemt.20940 (2011).

3 Kuntz, I. D. Hydration of macromolecules. IV. Polypeptide conformation in frozen solutions. *J Am Chem Soc* **93**, 516-518 (1971).

4 Pessen, H. & Kumosinski, T. F. Measurements of protein hydration by various techniques. *Methods Enzymol* **117**, 219-255 (1985).

5 Kuntz, I. D., Jr. & Kauzmann, W. Hydration of proteins and polypeptides. *Adv Protein Chem* **28**, 239-345 (1974).

6 Svergun, D. I. *et al.* Protein hydration in solution: experimental observation by x-ray and neutron scattering. *Proc Natl Acad Sci U S A* **95**, 2267-2272 (1998).

7 Daura, X. *et al.* Peptide folding: When simulation meets experiment. *Angew Chem Int Edit* **38**, 236-240, doi:Doi 10.1002/(Sici)1521-3773(19990115)38:1/2<236::Aid-Anie236>3.0.Co;2-M (1999).

8 Ortega, A., Amoros, D. & de la Torre, J. G. Prediction of Hydrodynamic and Other Solution Properties of Rigid Proteins from Atomic- and Residue-Level Models. *Biophys J* **101**, 892-898, doi:DOI 10.1016/j.bpj.2011.06.046 (2011).

9 Voss, N. R., Gerstein, M., Steitz, T. A. & Moore, P. B. The geometry of the ribosomal polypeptide exit tunnel. *Journal of Molecular Biology* **360**, 893-906, doi:DOI 10.1016/j.jmb.2006.05.023 (2006).

10 Humphrey, W., Dalke, A. & Schulten, K. VMD: Visual molecular dynamics. *J Mol Graph Model* **14**, 33-38, doi:Doi 10.1016/0263-7855(96)00018-5 (1996).

Summary

We were able to characterize stable Aβ monomers for the first time by small angle neutron scattering (SANS) under non-polar conditions (100 % d-HFIP) at extremely high protein concentrations ($A\beta_{1-40}$: 5.4 mg/ml, $A\beta_{1-42}$: 2.4 mg/ml)[89]. The radii of gyration (R_g) were determined to be 1.6 ± 0.1 nm for $A\beta_{1-42}$ and 1.0 ± 0.1 nm for $A\beta_{1-40,}$ which are in good agreement with the averaged radii from the PDB structures of solid state NMR studies. Further structural details could not be resolved probably due to large structural heterogeneity of the monomeric Abeta peptides leading to large error bars at high scattering vector Q. In a complementary approach, the hydrodynamic radius of monomeric Aβ was obtained from dynamic light scattering (DLS) as 3.2 nm for $A\beta_{1-42}$ and 1.8 nm for $A\beta_{1-40}$[89]. Additionally, the precipitation of preformed aggregates in d-HFIP with sizes of several micrometers and <1% volume fraction as dominating process was observed by time resolved DLS. An obvious change of scattering intensity of monomer was not observed, which indicates neither fragmentation nor dissociation of the preformed aggregates occur in detectable amount.

At pH=7.4 in aqueous buffer we successfully prepared the samples with more than 90% monomers at a concentration range between 0.1 mg/ml and 1 mg/ml for time resolved SANS and DLS experiments in an incubation time gap between 0.5 h and 300 h. According to the Beaucage model the R_g of $A\beta_{1-42}$ monomer is about 1 nm. By SANS small oligomers built from 5 to 20 monomeric units were observed during the aggregation processes. At 0.25 mg/ml we detected a constant low fraction of Aβ42 5- or 6-mer with $R_g \approx 2$ nm throughout the whole incubation time. Due to the not sufficiently deviating radii of gyration the 5- and 6-mer could not be distinguished from each other. At Aβ concentrations below and above 0.25 mg/ml a dissociation of 10-/12-mer (or 15-/18-mer) to 5-/6-mer was observed. This phenomenon corresponds roughly to the paranuclei – protofibril – fibril mechanism with Aβ 5-/6-mer as paranuclei and the building unit, which self-assembles to large oligomers and protofibril/fibril. Such small oligomeric Aβ aggregates, which appear to resemble paranuclei, have been detected by SANS never before. The also observed multiples of 5-/6-mers (10-/12-mer, 15-/18-mer) with a

globular shape could be ´off-pathway´ oligomers which act as a source for 5-/6-mers as postulated for several aggregation models.

Using the combination of scattering methods (SANS, DLS), AFM and AUC a quantitative picture of Aβ aggregation was generated. In particular for SANS it was shown that it is a promising tool for the investigation of the self-assembly pathway of Aβ and other amyloid proteins.

Zusammenfassung

Im Rahmen dieser Arbeit gelang es erstmals, für SANS-Messungen geeignete stabile Aβ-Monomere bei deutlich erhöhten Proteinkonzentrationen ($A\beta_{1-40}$: 5.4 mg/ml, $A\beta_{1-42}$: 2.4 mg/ml) in unpolarem Lösungsmittel (100% d-HFIP) zu erhalten[89]. Die Gyrationsradien wurden mit 1.6 ± 0.1 nm für $A\beta_{1-42}$ und 1.0 ± 0.1 nm für $A\beta_{1-40}$, bestimmt, welche beide mit den aus PDB-Strukturen errechneten Radien gut übereinstimmen. Aufgrund der großen Fehlerbalken im hohen Streuungsvektorbereich waren die hochauflösenden Monomer-Strukturen nur schwer ermittelbar. Zusätzlich wurden mithilfe von DLS die hydrodynamischen Radien der Monomere mit 3.2 nm für $A\beta_{1-42}$ and 1.8 nm für $A\beta_{1-40}$ bestimmt. Zudem konnte eine Ausscheidung der vorgeformten Aggregate in d-HFIP mit einer Größe von einigen Mikrometern und einem Volumenanteil von <1% als dominierender Prozess ermittelt werden. Allerdings war weder die Fragmentierung noch die Abspaltung von Aggregaten zu beobachten.

In wäßriger Pufferlösung bei pH 7,4 ließen sich erfolgreich Proben mit mehr als 90 % Monomeren bei einer niedrigen Inkubationstemperatur (7°C) herstellen, welche mit einer $A\beta_{1-42}$ Konzentration zwischen 0,1 mg/ml und 1 mg/ml geeignet für zeitaufgelöste SANS- und DLS-Experimente waren. Der unter Verwendung des Beaucage-Models ermittelte R_g der $A\beta_{1-42}$-Monomere beträgt etwa 1 nm. Zusätzlich wurden kleine Oligomere, die sich aus 5 bis 20 Monomereinheiten zusammensetzten, während des Aggregationsprozesses beobachtet. Bei 0,25 mg/ml $A\beta_{1-42}$ ließen sich während der gesamten Inkubationszeit Aβ 5-/6-mere mit $R_g \approx 2$ nm beobachten. Aufgrund der ähnlichen Größe der Aβ 5- und 6-mere konnten diese nicht voneinander unterschieden werden. Oberhalb und unterhalb von 0,25 mg/ml $A\beta_{1-42}$ traten zusätzlich zum 5-/6-mer 10-/12-mere und 15-/ 18-mere auf. Dieses Phänomen entspricht deutlich dem Paranuclei-Protofibril-Fibril-Mechanismus mit Aβ 5-/6-mer als Paranukleus, bzw. Baustein, der den Keim zur Aggregation in größere Oligomere und Protofibrillen, sowie Fibrillen darstellt. Mithilfe von SANS sind Paranuklei während des Aggregationsprozesses niemals zuvor beobachtet worden. Die Tatsache, dass 10-/12-mere und 15-/18-mere ganzzahlige Vielfache der 5-/6-mere sind, deutet darauf hin, dass

Aggregatwachstum nicht nur durch Monomeraddition sondern auch durch Zusammenlagerung der Paranuklei erfolgen kann. Alternativ könnte es sich auch um ‘off-pathway’-Oligomere handeln, welche als Quelle für in verschiedenen Aggregationsmodellen postulierte 5-/6-mere dienen.

Unter Verwendung einer Kombination von Streuungsmethoden (SANS, DLS) mit AFM und AUC konnte ein quantitatives Bild der Aβ-Aggregation erstellt werden. Prinzipiell konnte gezeigt werden, dass SANS sich auf das schwierige System des stark aggregierende Aβ anwenden lässt, wenn Probenvorbereitung und Lösungsbedingungen so optimiert sind, dass ausreichende Peptidkonzentrationen erreicht werden. Damit eröffnet sich eine Vielzahl neuer Möglichkeiten, um die Aggregation von Aβ sowie die damit verbundenen Strukturen von Intermediaten zu erforschen und neue Informationen zu erhalten, die durch andere Methoden nicht zugänglich sind.

Bibliography

1. File:Main_protein_structure_levels_en @ commons.wikimedia.org. at <https://commons.wikimedia.org/wiki/File:Main_protein_structure_levels_en.svg>
2. Dobson, C. M. Protein folding and misfolding. *Nature* **426,** 884–90 (2003).
3. Wright, P. E. & Dyson, H. J. Intrinsically Unstructured Proteins : Re-assessing the Protein Structure-Function Paradigm. *J. Mol. Biol.* **293,** 321–331 (1999).
4. Carley, W. W., Barak, L. S. & Webb, W. W. F-actin aggregates in transformed cells. *J. Cell Biol.* **90,** 797–802 (1981).
5. Stefani, M. & Dobson, C. M. Protein aggregation and aggregate toxicity: new insights into protein folding, misfolding diseases and biological evolution. *J. Mol. Med. Berlin Ger.* **81,** 678–699 (2003).
6. Aguzzi, A. & O'Connor, T. Protein aggregation diseases: pathogenicity and therapeutic perspectives. *Nat. Rev. Drug Discov.* **9,** 237–248 (2010).
7. John, A. & Gerald, A. Alzheimer ' s Disease : The Amyloid Cascade Hypothesis. 184–185 (1992).
8. Sarah E. Bondos. methods for Measuring protein Aggregation. *Curr. Anal. Chem.* **2,** 157–170 (2006).
9. Tyedmers, J., Mogk, A. & Bukau, B. Cellular strategies for controlling protein aggregation. *Nat. Rev. Mol. Cell Biol.* **11,** 777–788 (2010).
10. Gibson, T. J. & Murphy, R. M. Inhibition of insulin fibrillogenesis with targeted peptides. *Protein Sci.* **15,** 1133–1141 (2006).
11. Sabaté, R., Gallardo, M. & Estelrich, J. An autocatalytic reaction as a model for the kinetics of the aggregation of beta-amyloid. *Biopolymers* **71,** 190–5 (2003).
12. Nag, S. *et al.* Nature of the Amyloid-Monomer and the Monomer-Oligomer Equilibrium. *J. Biol. Chem.* **286,** 13827–13833 (2011).
13. LeVine, H. Alzheimer's beta-peptide oligomer formation at physiologic concentrations. *Anal. Biochem.* **335,** 81–90 (2004).
14. Collins, S. R., Douglass, A., Vale, R. D. & Weissman, J. S. Mechanism of prion propagation: Amyloid growth occurs by monomer addition. *PLoS Biol.* **2,** (2004).
15. Schreck, J. S. & Yuan, J. M. A kinetic study of amyloid formation: Fibril growth and length distributions. *J. Phys. Chem. B* **117,** 6574–6583 (2013).
16. Morris, R. J. *et al.* Mechanistic and environmental control of the prevalence and lifetime of amyloid oligomers. *Nat. Commun.* **4,** 1891 (2013).

17. Hong, L., Qi, X. & Zhang, Y. Dissecting the kinetic process of amyloid fiber formation through asymptotic analysis. *J. Phys. Chem. B* **116,** 6611–6617 (2012).

18. Oosawa, F. & Kasai, M. A theory of linear and helical aggregations of macromolecules. *J. Mol. Biol.* **4,** 10–21 (1962).

19. Ferrone, F. a, Hofrichter, J., Sunshine, H. R. & Eaton, W. a. Kinetic studies on photolysis-induced gelation of sickle cell hemoglobin suggest a new mechanism. *Biophys. J.* **32,** 361–380 (1980).

20. Flyvbjerg, H., Jobs, E. & Leibler, S. Kinetics of self-assembling microtubules: an 'inverse problem' in biochemistry. *Proc. Natl. Acad. Sci. U. S. A.* **93,** 5975–5979 (1996).

21. Watzky, M. a., Morris, A. M., Ross, E. D. & Finke, R. G. Fitting yeast and mammalian prion aggregation kinetic data with the finke-watzky two-step model of nucleation and autocatalytic growth. *Biochemistry* **47,** 10790–10800 (2008).

22. Zagorski, M. G. *et al. Amyloid, Prions, and Other Protein Aggregates*. *Methods in Enzymology* **309,** (Elsevier, 1999).

23. Koo, E. H., Lansbury, P. T. & Kelly, J. W. Amyloid diseases: abnormal protein aggregation in neurodegeneration. *Proc. Natl. Acad. Sci. U. S. A.* **96,** 9989–9990 (1999).

24. Nowotny, P., M Kwon, J. & M Goate, A. Alzheimer Disease. *Encycl. Life Sci.* 1–6 (2001).

25. Dauer, W. & Przedborski, S. Parkinson's Disease. *Neuron* **39,** 889–909 (2003).

26. Sigurdsson, E. M. *Amyloid Proteins: Methods And Protocols*. (Springer Science & Business Media, 2005).

27. Roos, R. A. C. Huntington's disease: a clinical review. *Orphanet J. Rare Dis.* **5,** 40 (2010).

28. Sipe, J. D. & Cohen, a S. Review: history of the amyloid fibril. *J. Struct. Biol.* **130,** 88–98 (2000).

29. S., C. © 1959 Nature Publishing Group. *Nature* **184,** 2003–2004 (1959).

30. Inouye, H., Fraser, P. E. & Kirschner, D. A. Structure of Aβ-crystallite assemblies formed by Alzheimer , B-amyloid protein analogues : analysis by x-ray diffraction X-ray diffraction. *Biophys. J.* **64,** 502–519 (1993).

31. Blennow, K., de Leon, M. J. & Zetterberg, H. Alzheimer's disease. *Lancet* **368,** 387–403 (2006).

32. Fernandez, A. Alzheimer's Disease: is our Healthcare System Ready?

33. Williamson, J., Jill, G. & S, M. K. Genetic Aspects of Alzheimer Disease.

Neurologist **15,** 80–86 (2009).

34. Gomez-Isla, T. *et al.* The impact of different presenilin 1 andpresenilin 2 mutations on amyloid deposition, neurofibrillary changes and neuronal loss in the familial Alzheimer's disease brain: evidence for other phenotype- modifying factors. *Brain* **122,** 1709–19. (1999).

35. Bertram, L. & Tanzi, R. E. Thirty years of Alzheimer's disease genetics: the implications of systematic meta-analyses. *Nat. Rev. Neurosci.* **9,** 768–78 (2008).

36. Berezovska, O. Familial Alzheimer's Disease Presenilin 1 Mutations Cause Alterations in the Conformation of Presenilin and Interactions with Amyloid Precursor Protein. *J. Neurosci.* **25,** 3009–3017 (2005).

37. Shankar, G. M. *et al.* Natural Oligomers of the Alzheimer Amyloid-β Protein Induce Reversible Synapse Loss by Modulating an NMDA-Type Glutamate Receptor-Dependent Signaling Pathway. *J. Neurosci.* **27,** 2866–2875 (2007).

38. De Felice, F. G. *et al.* Aβ oligomers induce neuronal oxidative stress through an N-methyl-D-aspartate receptor-dependent mechanism that is blocked by the Alzheimer drug memantine. *J. Biol. Chem.* **282,** 11590–11601 (2007).

39. Coulson, E. J. Does the p75 neurotrophin receptor mediate Aβ-induced toxicity in Alzheimer's disease *J. Neurochem.* **98,** 654–660 (2006).

40. Zhao, W.-Q. *et al.* Amyloid beta oligomers induce impairment of neuronal insulin receptors. *FASEB J.* **22,** 246–260 (2008).

41. Yamamoto, N. *et al.* A ganglioside-induced toxic soluble Aβ assembly: Its enhanced formation from Aβ bearing the arctic mutation. *J. Biol. Chem.* **282,** 2646–2655 (2007).

42. Magdesian, M. H. *et al.* Amyloid-β binds to the extracellular cysteine-rich domain of frizzled and inhibits Wnt/β-catenin signaling. *J. Biol. Chem.* **283,** 9359–9368 (2008).

43. De Felice, F. G. *et al.* Protection of synapses against Alzheimer's-linked toxins: insulin signaling prevents the pathogenic binding of Abeta oligomers. *Proc. Natl. Acad. Sci. U. S. A.* **106,** 1971–6 (2009).

44. Ono, K., Takahashi, R., Ikeda, T. & Yamada, M. Cross-seeding effects of amyloid beta-protein and α-synuclein. *J. Neurochem.* **122,** 883–890 (2012).

45. Soto, C., Brahes, M. C., Alvarez, J. & Inestrosa, N. C. Structural Determinants of the Alzheimer ' s. (1994).

46. Kirschner, D. A. *et al.* Synthetic peptide homologous to fi protein from Alzheimer disease forms amyloid-like fibrils in vitro. *Neurobiology* **84,** 6953–6957 (1987).

47. Vivekanandan, S., Brender, J. R., Lee, S. Y. & Ramamoorthy, A. A partially folded structure of amyloid-beta(1-40) in an aqueous environment. *Biochem. Biophys. Res. Commun.* **411,** 312–316 (2011).

48. Crescenzi, O. *et al.* Solution structure of the Alzheimer amyloid beta-peptide (1-42) in an apolar microenvironment: Similarity with a virus fusion domain. *Eur. J. Biochem.* **269,** 5642–5648 (2002).

49. Sticht, H. *et al.* Structure of Amyloid A4-(1-40)-Peptide of Alzheimer's Disease. *Eur. J. Biochem.* **233,** 293–298 (1995).

50. Tomaselli, S. *et al.* The alpha-to-beta conformational transition of Alzheimer's Aβ-(1-42) peptide in aqueous media is reversible: A step by step conformational analysis suggests the location of β conformation seeding. *ChemBioChem* **7,** 257–267 (2006).

51. Lin, M.-S. *et al.* Investigation of the mechanism of beta-amyloid fibril formation by kinetic and thermodynamic analyses. *Langmuir* **24,** 5802–8 (2008).

52. Lührs, T. *et al.* 3D structure of Alzheimer's amyloid-beta(1-42) fibrils. *Proc. Natl. Acad. Sci. U. S. A.* **102,** 17342–17347 (2005).

53. Lu, J.-X. *et al.* Molecular Structure of β-Amyloid Fibrils in Alzheimer's Disease Brain Tissue. *Cell* **154,** 1257–1268 (2013).

54. Hortschansky, P., Schroeckh, V., Christopeit, T., Zandomeneghi, G. & Fändrich, M. The aggregation kinetics of Alzheimer ' s b-amyloid peptide is controlled by stochastic nucleation. *Protein Sci.* **14,** 1753–1759 (2005).

55. Gillam, J. E. & MacPhee, C. E. Modelling amyloid fibril formation kinetics: mechanisms of nucleation and growth. *J. Phys. Condens. Matter* **25,** 373101 (2013).

56. Malinchik, S. B., Inouye, H., Szumowski, K. E. & Kirschner, D. a. Structural analysis of Alzheimer's beta(1-40) amyloid: protofilament assembly of tubular fibrils. *Biophys. J.* **74,** 537–545 (1998).

57. Fändrich, M., Schmidt, M. & Grigorieff, N. Recent progress in understanding Alzheimer's β-amyloid structures. *Trends Biochem. Sci.* **36,** 338–345 (2011).

58. Paravastu, A. K., Leapman, R. D., Yau, W.-M. & Tycko, R. Molecular structural basis for polymorphism in Alzheimer's beta-amyloid fibrils. *Proc. Natl. Acad. Sci. U. S. A.* **105,** 18349–18354 (2008).

59. Grüning, C. S. R. *et al.* The off-rate of monomers dissociating from amyloid-β protofibrils. *J. Biol. Chem.* **288,** 37104–37111 (2013).

60. Wang, S. S. S., Chen, Y. T., Chen, P. H. & Liu, K. N. A kinetic study on the aggregation behavior of B-amyloid peptides in different initial solvent

environments. *Biochem. Eng. J.* **29,** 129–138 (2006).

61. Bartolini, M. *et al.* Kinetic characterization of amyloid-beta 1–42 aggregation with a multimethodological approach. *Anal. Biochem.* **414,** 215–225 (2011).

62. Childers, W. S., Anthony, N. R., Mehta, A. K., Berland, K. M. & Lynn, D. G. Phase networks of cross-β peptide assemblies. *Langmuir* **28,** 6386–95 (2012).

63. Lovell, M. a., Robertson, J. D., Teesdale, W. J., Campbell, J. L. & Markesbery, W. R. Copper, iron and zinc in Alzheimer's disease senile plaques. *J. Neurol. Sci.* **158,** 47–52 (1998).

64. Bush, A. I. The metallobiology of Alzheimer's disease. *Trends Neurosci.* **26,** 207–14 (2003).

65. Atwood, C. S. *et al.* Characterization of copper interactions with Alzheimer amyloid β peptides: Identification of an attomolar-affinity copper binding site on amyloid β1-42. *J. Neurochem.* **75,** 1219–1233 (2000).

66. Ha, C., Ryu, J. & Chan, B. P. Metal ions differentially influence the aggregation and deposition of Alzheimer's β-amyloid on a solid template. *Biochemistry* **46,** 6118–6125 (2007).

67. Cherny, R. a *et al.* Aqueous Dissolution of Alzheimer ' s Disease A β Amyloid Deposits by Biometal Depletion Aqueous Dissolution of Alzheimer ' s Disease A Amyloid Deposits by Biometal Depletion *. *J. Biol. Chem.* **274,** 23223–23228 (1999).

68. Atwood, C. S. *et al.* PROTEIN CHEMISTRY AND STRUCTURE : Dramatic Aggregation of Alzheimer A β by Cu (II) Is Induced by Conditions Representing Physiological Acidosis Dramatic Aggregation of Alzheimer Aβ by Cu (II) Is Induced by Conditions Representing Physiological Acidos. *J. Biol. Chem.* **273,** 12817–12826 (1998).

69. Yoshiike, Y. *et al.* New Insights on How Metals Disrupt Amyloid β-Aggregation and Their Effects on Amyloid-β Cytotoxicity. *J. Biol. Chem.* **276,** 32293–32299 (2001).

70. Bush, A. I., Pettingell, W. H., Paradis, M. D. & Tanzi, R. E. Modulation of A?? adhesiveness and secretase site cleavage by zinc. *J. Biol. Chem.* **269,** 12152–12158 (1994).

71. Bush, A. I. *et al.* Rapid Induction of Alzheimer A-Beta Amyloid Formation By Zinc. *Science (80-.).* **265,** 1464–1467 (1994).

72. Grasso, G. *et al.* Copper(I) and Copper(II) Inhibit Aβ peptides proteolysis by insulin-degrading enzyme differently: Implications for metallostasis alteration in alzheimer's disease. *Chem. - A Eur. J.* **17,** 2752–2762 (2011).

73. Giurleo, J. T., He, X. & Talaga, D. S. beta-Lactoglobulin Assembles into Amyloid through Sequential Aggregated Intermediates. *J. Mol. Biol.* **381,** 1332–1348 (2008).

74. Nag, S. *et al.* Nature of the amyloid-beta monomer and the monomer-oligomer equilibrium. *J. Biol. Chem.* **286,** 13827–33 (2011).

75. Lee, C.-C., Nayak, A., Sethuraman, A., Belfort, G. & McRae, G. J. A Three-Stage Kinetic Model of Amyloid Fibrillation. *Biophys. J.* **92,** 3448–3458 (2007).

76. Hamley, I. W. Peptide Fibrillization. *Angew. Chemie Int. Ed.* **46,** 8128–8147 (2007).

77. Bitan, G. *et al.* Amyloid β-protein (Aβ) assembly: Aβ40 and Aβ42 oligomerize through distinct pathways. *Proc. Natl. Acad. Sci. U. S. A.* **100,** 330–335 (2003).

78. Harper, J. D., Wong, S. S., Lieber, C. M. & Lansbury, P. T. Assembly of A β Amyloid Protofibrils : An in Vitro Model for a Possible Early Event in Alzheimer ' s Disease Assembly of A Amyloid Protofibrils : An in Vitro Model for a Possible Early Event in Alzheimer ' s Disease †. *Biochemistry* **38,** 8972–8980 (1999).

79. Lin, H., Bhatia, R. & Lal, R. Amyloid beta protein forms ion channels: implications for Alzheimer's disease pathophysiology. *FASEB J.* **15,** 2433–44 (2001).

80. Quist, A. *et al.* Amyloid ion channels: a common structural link for protein-misfolding disease. *Proc. Natl. Acad. Sci. U. S. A.* **102,** 10427–10432 (2005).

81. Ahmed, M. *et al.* Structural conversion of neurotoxic amyloid-β1–42 oligomers to fibrils. *Nat. Struct. Mol. Biol.* **17,** 561–567 (2010).

82. Bitan, G. Teplow, B. in *Methods in molecular biology-Amyloid Protein* 3–9 (2005). at <http://www.springerprotocols.com/Abstract/doi/10.1385/1-59259-874-9:003>

83. Fukumoto, H. *et al.* High-molecular-weight-amyloid oligomers are elevated in cerebrospinal fluid of Alzheimer patients. *FASEB J.* **24,** 2716–2726 (2010).

84. B, G. On the nucleation and growth of amyloid ,beta-protein fibrils: *Biophysics (Oxf).* **93,** 1125–1129 (1996).

85. Yong, W. *et al.* Structure determination of micelle-like intermediates in amyloid beta -protein fibril assembly by using small angle neutron scattering. *Proc. Natl. Acad. Sci. U. S. A.* **99,** 150–154 (2002).

86. Pallitto, M. M. & Murphy, R. M. A mathematical model of the kinetics of beta-amyloid fibril growth from the denatured state. *Biophys. J.* **81,** 1805–1822 (2001).

87. Kamihira, M., Naito, a, Tuzi, S., Nosaka, a Y. & Saitô, H. Conformational transitions and fibrillation mechanism of human calcitonin as studied by high-resolution solid-state 13C NMR. *Protein Sci.* **9,** 867–877 (2000).

88. Zipper, P. & Durchschlag, H. Small-angle X-ray scattering studies on the X-ray aggregation of malate synthase Computer simulations and models. *Zeitschrift fur Naturforschung. Sect. C* **35c,** 890–901 (1980).

89. Zhang-haagen, B., Biehl, R., Nagel-steger, L. & Radulescu, A. Monomeric Amyloid Beta Peptide in Hexafluoroisopropanol Detected by Small Angle Neutron Scattering. *PLoS One* 1–12 (2016). doi:10.1371/journal.pone.0150267